ACTIVE CONTOUR MODELS
FOR KNEE CARTILAGE AND MENISCUS
ULTRASOUND IMAGE SEGMENTATION

AMIR FAISAL

FACULTY OF ENGINEERING
UNIVERSITY OF MALAYA
KUALA LUMPUR

2017

ACTIVE CONTOUR MODELS FOR KNEE CARTILAGE AND MENISCUS ULTRASOUND IMAGE SEGMENTATION

AMIR FAISAL

THESIS SUBMITTED IN FULFILMENT OF THE REQUIREMENTS FOR THE DEGREE OF DOCTOR OF PHILOSOPHY

FACULTY OF ENGINEERING
UNIVERSITY OF MALAYA
KUALA LUMPUR

2017

UNIVERSITI MALAYA

ORIGINAL LITERARY WORK DECLARATION

Name of Candidate: Amir Faisal (I.C./Passport No.:

Registration/Matrix No.: KHA140002

Name of Degree: Doctor of Philosophy

Title of Project Paper/Research Report/Dissertation/Thesis ("this Work"):

Active Contour Models for Knee Cartilage and Meniscus Ultrasound Image Segmentation

Field of Study: Biomedical Engineering

I do solemnly and sincerely declare that:

(1) I am the sole author/writer of this Work;
(2) This work is original;
(3) Any use of any work in which copyright exists was done by way of fair dealing and for permitted purposes and any excerpt or extract from, or reference to or reproduction of any copyright work has been disclosed expressly and sufficiently and the title of the Work and its authorship have been acknowledged in this Work;
(4) I do not have any actual knowledge nor do I ought reasonably to know that the making of this work constitutes an infringement of any copyright work;
(5) I hereby assign all and every rights in the copyright to this Work to the University of Malaya ("UM"), who henceforth shall be owner of the copyright in this Work and that any reproduction or use in any form or by any means whatsoever is prohibited without the written consent of UM having been first had and obtained;
(6) I am fully aware that if in the course of making this Work I have infringed any copyright whether intentionally or otherwise, I may be subject to legal action or any other action as may be determined by UM.

Candidate's Signature Date

Subscribed and solemnly declared before,

Witness's Signature Date

Name:
Designation:

ABSTRACT

Quantification of the cartilage degeneration as well as the meniscus degeneration and displacement requires segmentation of various parts of the knee joints in the two-dimensional ultrasound images in order to provide a direct measurement of the cartilage thickness and the meniscus area and position, respectively. The goal in the knee cartilage ultrasound image segmentation is to locate the boundaries of a monotonous hypoechoic band between hyperechoic lines of the soft tissue-cartilage interface and of the cartilage-bone interface. Hence, the true thickness between the two interfaces can be computed based on the segmented images. Meanwhile, the goal in segmenting the meniscus ultrasound image is to locate the femoral condyle, the meniscus, and the tibial plateau simultaneously. This thesis presents active contour models for knee cartilage and meniscus ultrasound image segmentation. Cartilage boundary segmentation using locally statistical level set method (LSLSM) and cartilage thickness estimation using the normal distance are presented. In addition, multiple active contours using scalable local regional information on expandable kernel (MLREK) have been proposed to capture multiple, separate objects of the femoral condyle, the meniscus, and the tibial plateau. Segmentation performance is then validated using Dice coefficient and Hausdorff distance metrics. Segmentation results of the presented methods are compared to the existing active contour methods in the attempt of segmenting the knee cartilage and meniscus in the ultrasound images, which show an improvement on the segmentation performance offered by the proposed methods. The choice of various parameters in MLREK in response to the segmentation outcome is then investigated. A demonstration on how to choose the threshold value to adapt the kernel size in order to successfully reach the boundary concavity is given. The ability of multiple contours in preventing merging and overlapping in the shared boundaries of

separate regions is shown. A flexibility in setting each contour with different parameter values for multiple structure segmentation is also illustrated. MLREK has shown to perform multiple object segmentation all at once in an ultrasound image. Application of the presented methods to segment a set of the knee cartilage and meniscus ultrasound images illustrates a good and consistent segmentation performance. The reproducibility of the ultrasound-based cartilage thickness measurements using intraclass correlation coefficient and agreement between pairs of the measurements by the normal distance and the manual measurement using Bland-Altman analysis are determined. The cartilage segmentation possible with LSLSM has allowed the obtained segmentation results to be used for making the cartilage thickness computation. The robustness of the methods described against various thickness of the cartilage and various shapes and areas of the multiple objects indicates a potential of the methods to be applied for the assessment of the cartilage degeneration as well as the meniscus degeneration and displacement. The cartilage degeneration and the meniscus degeneration and displacement typically seen as changes in the cartilage thickness and the meniscus area and position can be quantified over time by comparing the cartilage thickness and the meniscus area and position at a certain time interval.

ABSTRAK

Pengkuantitian degenerasi rawan lutut dan degenerasi serta sesaran meniskus memerlukan pensegmenan pelbagai bahagian pada imej ultrabunyi sendi lutut untuk memberikan ukuran terus pada ketebalan rawan lutut dan kawasan serta kedudukan meniskus. Matlamat pensegmenan imej ultrabunyi rawan lutut adalah untuk mendapatkan sempadan jalur hipoekoik senada antara garisan antara muka hiperekoik tisu lembut dengan rawan lutut. Dengan demikian, ketebalan sebenar di antara kedua antara muka boleh diukur berdasarkan imej yang disegmentasi. Matlamat pensegmenan imej ultrabunyi meniskus termasuk segmentasi imej ultrabunyi meniskus untuk mendapatkan pelbagai objek serentak pada lutut seperti kondil femur, meniskus, dan tibia plateau. Kajian ini akan membentangkan mengenai model kontur aktif untuk pensegmenan imej ultrabunyi rawan lutut dan meniskus. Pensegmenan rawan lutut menggunakan *locally statistical level set method* (LSLSM) dan pengiraan ketebalan rawan menggunakan jarak normal akan dibentangkan. Selain itu, beberapa kontur aktif yang menggunakan maklumat tempatan boleh skala pada kernel boleh kembang (MLREK) dicadangkan untuk pensegmenan pelbagai objek berasingan kondil femur, meniskus, dan tibia plateau. Kemudian prestasi pensegmenan disahkan menggunakan metrik pekali *Dice* dan jarak *Hausdorff*. Prestasi segmentasi model kontur aktif yang kami cadangkan dibandingkan dengan model kontur aktif yang sedia ada dalam pensegmenan imej ultrabunyi rawan lutut dan meniskus yang menunjukan peningkatan keputusan pensegmenan ditawarkan oleh model yang dibentangkan. Kemudian kesan pilihan pelbagai parameter dalam metodologi yang dicadangkan terhadap hasil pensegmenan turut disiasatkan. Bagaimana nilai ambang harus dipilih untuk menyesuaikan saiz kernel untuk berjaya mencapai sempadan cekung ditunjukkan. Pelbagai kontur boleh menghalang penggabungan dan pertindihan di sempadan bersama pada wilayah

berasingan ditunjukkan. Pilihan fleksibel dalam memberikan nilai-nilai parameter yang berbeza untuk setiap kontur apabila membahagikan pelbagai objek juga digambarkan. MLREK telah menunjukkan dapat melaksanakan pensegmenan serentak pelbagai objek kondil femur, meniskus, dan tibia plateau dalam imej ultrabunyi. Penggunaan kaedah yang dibentangkan untuk pensegmenan satu set imej ultrabunyi rawan lutut dan meniskus menunjukan hasil pensegmenan yang baik dan konsisten. Kebolehulangan daripada pengukuran ketebalan rawan lutut berdasarkan imaej ultrabunyi ini menggunakan pekali korelasi intrakelas dan persetujuan antara pasangan ukuran oleh jarak normal dan pengukuran manual menggunakan analisis *Bland-Altman* diukur. Pensegmenan rawan lutut dimungkinkan dengan LSLSM telah membenarkan keputusan pensegmenan digunakan untuk membuat pengiraan ketebalan rawan lutut. Keteguhan kaedah yang dibentangkan terhadap pelbagai ketebalan rawan lutut, bentuk, saiz, dan kedudukan daripada pelbagai objek menunjukkan potensi penggunaan kaedah untuk penilaian degenerasi rawan lutut dan degenerasi serta sesaran meniskus. Degenerasi rawan lutut dan degenerasi serta anjakan meniskus biasanya dilihat sebagai perubahan dalam ketebalan rawan lutut dan kawasan serta kedudukan meniskus boleh diukur mengikut masa dengan membandingkan ketebalan rawan lutut dan kawasan serta kedudukan meniskus di beberapa selang masa.

ACKNOWLEDGEMENTS

First of all, I am greatly grateful to Allah for everything in my life. I would like to express my gratitude to my supervisor, Ir. Dr. Lai Khin Wee, for his constant support, encouragement, and supervision during my journey in this Ph.D. program. I wish to thank my co-supervisors, Dr. Ng Siew Cheok for the discussions, comments, and suggestions on the development of my research and Goh Siew Li, M.D. at the faculty of medicine for discussions and explanations on the medical sciences, which helped me understanding various medical terms. I am benefited from collaborations with professor John George at the department of biomedical imaging, faculty of medicine, University of Malaya (UM) and professor Eko Supriyanto at the faculty of bioscience and medical engineering, University of Technology Malaysia, particularly for providing ultrasound images of the knee joint. I greatly appreciate financial support from University of Malaya Research Grant, International Graduate Research Assistant Scheme, and Postgraduate Research Grant for the last three years. I acknowledge the comment and feedback from candidature defense panels, internal & external examiners, and committee of examiners.

I am benefited from my interactions with many people in UM. In particular, I thank Azira Khalil for discussion on various medical imaging modalities. I thank Dr. Ardian Nata Atmaja, Dr. Devi Chandra, Efrizal, and Muhammad Doris for occasional talks related academic life and beyond. My thanks also go to my lab mates at Neuroengineering Lab. and Medical Imaging Lab.

Last but not least, I personally dedicate this thesis to my family. This would never have happened without my confidence and their unconditional love.

TABLE OF CONTENTS

LIST OF FIGURES

LIST OF TABLES

LIST OF SYMBOLS AND ABBREVIATIONS

C	:	contour.
C_0	:	initial contour.
E	:	energy functional.
F	:	force.
H	:	heaviside function.
I	:	input image.
J	:	true image.
K	:	kernel function.
L	:	intensity range.
M_i	:	membership functions.
N	:	number of regions.
Δ	:	Laplacian operator.
Δd	:	additional scale of the kernel.
Ω	:	image domain.
$\Re$	:	Real numbers.
$*$	:	convolution operator.
δ	:	delta function.
η	:	additive noise.
$\hat{\mathbf{n}}$	:	unit normal vector.
κ	:	curvature along the contour.
λ	:	Lagrangian multiplier.
$\mathrm{div}(\cdot)$	:	divergence.
thres	:	intensity threshold.
μ_i	:	means.
∇	:	gradient operator.
ν	:	weighing parameter of contour's smoothness.
ω	:	constant motion.
ϕ	:	level set function.
ψ	:	a tiny change perpendicular to ϕ.
σ_i	:	variances.
τ	:	threshold value.
a	:	positive constant.
b	:	bias field.
c_i	:	piecewise constants.
d	:	distance.
d_{initial}	:	initial scale of the kernel.
e_i	:	energy functions.
g	:	edge indicator.

l	:	number of iterations.
m	:	pixel numbers.
n	:	number of the contours.
q	:	contour line.
t	:	time.
ξ	:	a small number of weighting parameter.
2-D	:	two-dimensional.
3-D	:	three-dimensional.
ACWE	:	active contours without edges.
CT	:	computed tomography.
DSC	:	Dice similarity coefficient.
GAC	:	geodesic active contour.
HD	:	Hausdorff distance.
ICC	:	intraclass correlation coefficient.
JSW	:	joint space width.
LGDF	:	local Gaussian distribution fitting.
LRAC	:	localizing region-based active contour.
LRD	:	local region descriptors.
LREK	:	local region-scalable force with expandable kernel.
LRES	:	active contour using local regional information on extendable search line.
LSLSM	:	locally statistical level set method.
MLREK	:	multiple active contours using scalable local regional information on expandable kernel.
MRI	:	magnetic resonance imaging.
OA	:	osteoarthritis.
RSF	:	region-scalable fitting.
SLR	:	scalable local regional.
SVMLS	:	statistical variational multiphase level set method.
WKVLS	:	locally weighted K-means variational level set method.

LIST OF APPENDICES

CHAPTER 1: INTRODUCTION

This chapter introduces the background that leads to the development of the knee cartilage segmentation and thickness computation and the meniscus segmentation in the ultrasound images. An overview on several medical imaging modalities that are used for assessing the structure of the knee joint, particularly for the knee cartilage degeneration and the meniscus degeneration and displacement is given. The advantages and disadvantages of these medical imaging systems are also discussed. Ultrasound imaging that offers an excellent alternative to other imaging systems is highlighted in Section 1.1. The importance and the goals in segmenting the knee cartilage and meniscus in the ultrasound images are identified and stated in Section 1.2. Some of the problems inherent in these ultrasound images are identified. Speckle noise and intensity bias available due to physical constraint in the ultrasound image acquisition are discussed. The objectives and scope of work of this thesis are stated in Section 1.3 and Section 1.4, respectively. Section 1.5 provides an organizational layout and overall picture of the thesis.

1.1 Background

Osteoarthritis (OA) is the most prevalent form of arthritis and rheumatic diseases. It causes major implications for individual and public health care globally (World Health Organization, 2002). In general, OA has been strongly associated with ageing, causing pain and disability. This disease is also attributable to overweight and obesity in addition to heavy physical activities. The disease has affected more females than males of adults and elderly (Jackson, Simon, & Aberman, 2001). It is known that the knee is the commonest joint in the lower limb to be affected by OA that is most studied (Pereiraya et al., 2011).

Degenerative change in the cartilage is one of the primary features of the knee OA disease (Kazam et al., 2011). Since X-rays are useful to visualize the two-dimensional

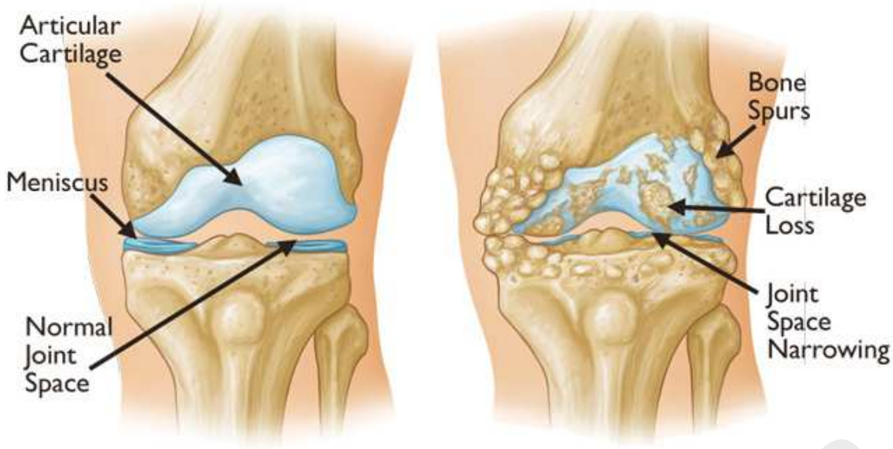

Figure 1.1: (Left) Normal joint space between the femur and the tibia. (Right) Decreased joint space due to damaged cartilage and bone spurs. (*Arthritis of the Knee*, 2017).

(2-D) structure of the bony features, it has been utilized in providing an assessment of the joint space width (JSW) for the knee OA screening and diagnosis (Roemer, Crema, Trattnig, & Guermazi, 2011). The JSW assessment, easily obtained from weight bearing knee projections, is often used to indicate joint space narrowing in order to determine the stage of the knee OA progression. However, the JSW assessment shows an indirect sign of the cartilage thickness provided by the measurement of the joint space width between the femur and the tibia (see Figure 1.1). It has shown a weak sensitivity to change (Buckland-Wright, 1994). In addition, cartilage loss that occurs on the other contact areas cannot be observed in these X-ray images (Hunter et al., 2006). Since X-rays lack in the depiction of the soft tissue, its ability to visualize other OA appearance features is limited. Although computed tomography (CT) is superior to X-rays due to a tomographic evaluation of soft tissues and bone, the contrast of the soft tissue in CT scans is limited to provide the depiction of the cartilage (W. P. Chan et al., 1991). Both imaging modalities have limitations of radiation exposure, where CT is more expensive than X-rays.

It is known that the joint space is not only shared by the cartilage, but also by the meniscus. As depicted in Figure 1.2(a), this concave-shaped pad of fibro-cartilage

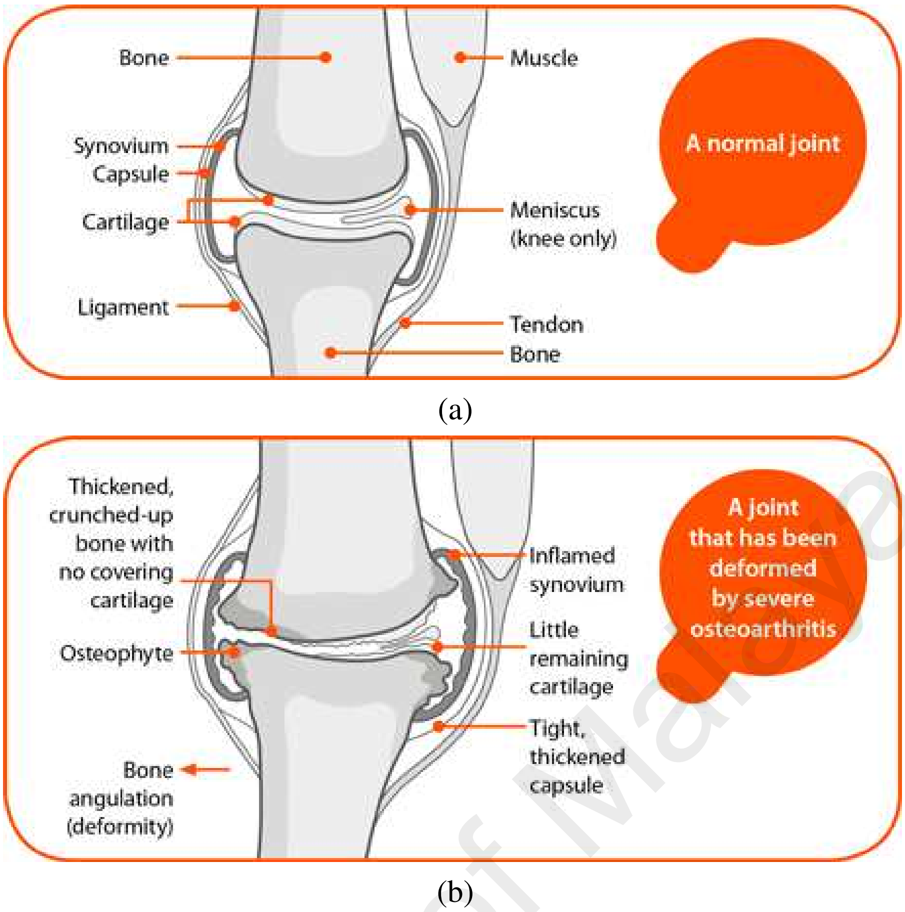

Figure 1.2: Schematic of (a) normal structure of the knee joint and (b) the knee joint affected by osteoarthritis (*What is arthritis?*, 2014)

is located in between the layers of the cartilage in the femoral condyle and the tibial plateau. It is found that the degeneration and displacement in the meniscus contribute to the progression of the knee OA as well (Amin et al., 2005; Hunter et al., 2009). According to recent research findings, the knee OA is recognized to affect the whole joint structure and causes changes in the surrounding bony structure and soft tissues, including synovial fluid, synovium, ligament, cartilage, meniscus, and bone (see Figure 1.2(b)). In order to provide a complete and accurate assessment of structural and symptomatic progression, the entire structures of the knee joint are necessary to be visualized (Braun & Gold, 2012).

Magnetic resonance imaging (MRI) allows a precise depiction of the entire joint structures, including bone, soft tissues, and synovial fluid. MRI has shown to be more reliable and sensitive than X-rays and CT in depicting changes in the knee joint caused by OA. It has been used as a diagnostic tool particularly for the purpose of the knee OA assessment (Iagnocco, 2010). In contrast to the 2-D X-ray images, MRI provides three-dimensional (3-D) imaging of the knee joint for identification of changes in intra- and extra-articular structures. As it demonstrates an excellent imaging quality, in recent years, there have been considerable developments for bone, cartilage, and meniscus segmentation in the 3-D MRI images for the purpose of knee OA characterization (Shan, Zach, & Niethammer, 2010; Dodin, Pelletier, Martel-Pelletier, & Abram, 2010; Fripp, Crozier, Warfield, & Ourselin, 2010; Folkesson, Dam, Olsen, Pettersen, & Christiansen, 2007; Tang, Millington, Acton, Crandall, & Hurwitz, 2006; Fripp et al., 2009; Boniatis, Panayiotakis, & Panagiotopoulos, 2008; Swanson et al., 2010). However, high cost, low availability, and high time consumption of the equipment have limited the routine clinical use of MRI (Naredo et al., 2009; Moller et al., 2008). It is also known that MRI is not suitable to be used for patients with metal implants.

Among other medical imaging modalities, ultrasound imaging is considered to be non-invasive, radiation-free, portable, real-time, cost effective, and widely accessible. It has been frequently used for a wide-range clinical application. While MRI has a comprehensive role in the assessment of the intra-articular structures, ultrasound imaging provides a complementary evaluation of the extra-articular structures (Kazam et al., 2011). Although the visualization of deeper articular structure and subchondral bone is prevented by the nature of sound, it has demonstrated its ability in depicting more appearance features of the knee OA than X-rays and CT (Abraham, Goff, Pearce, Francis, & Birrell, 2011), such as cartilage loss (Saarakkala et al., 2012), meniscal tears (Acebes, Romero, Contreras, Mahillo, & Herrero-Beaumont, 2013), ligament damage (Iagnocco, 2010), and synovial proliferation (Iagnocco, 2010) involved in the pathogenesis and progression of the knee OA (Oo & Boo, 2016). These advantages possessed by ultrasound imaging over

X-rays, CT, and MRI promote the routine clinical use of ultrasound imaging in addition to conventional imaging modalities and offer an excellent alternative to help diagnose or monitor the presence of the knee OA disease non-invasively (Moller et al., 2008).

1.2 Problem Statement

For the purpose of the assessment of the cartilage degeneration and the meniscus degeneration and displacement, segmentation of several parts of the knee joint from the 2-D ultrasound images is an important step in order to provide a direct measurement of the cartilage thickness and the meniscus area and position.

The degeneration in the cartilage is typically seen as the changes in the cartilage thickness. Segmentation is a necessary task in order to provide the thickness computation of the knee cartilage in the ultrasound images. As shown in Figure 1.3(a), the femoral condylar cartilage in ultrasound images is depicted as a monotonous hypoechoic band between the two interfaces of the soft tissue-cartilage and the cartilage-bone (Kazam et al., 2011). When segmenting the knee cartilage from the ultrasound images, it is important to locate the boundaries of these two interfaces that represents cartilage region. Therefore, the cartilage thickness between the two interfaces can be computed based on the segmented images. Segmenting the cartilage from surrounding tissues is difficult due to the boundary between different tissues is not sufficiently distinct. The segmentation algorithm should be insensitive to various cartilage shape and thickness.

The degeneration and displacement in the meniscus are typically seen as the changes in the meniscus area and position, respectively. The meniscus degeneration can be determined through the measurement of the deformation in the meniscus area. In order to determine the meniscus displacement, it is required to measure the relative location of the meniscus to the femoral condyle and the tibial plateau (see Figure 1.3(b)). While segmentation of the meniscus could only determine the meniscus area, simultaneous

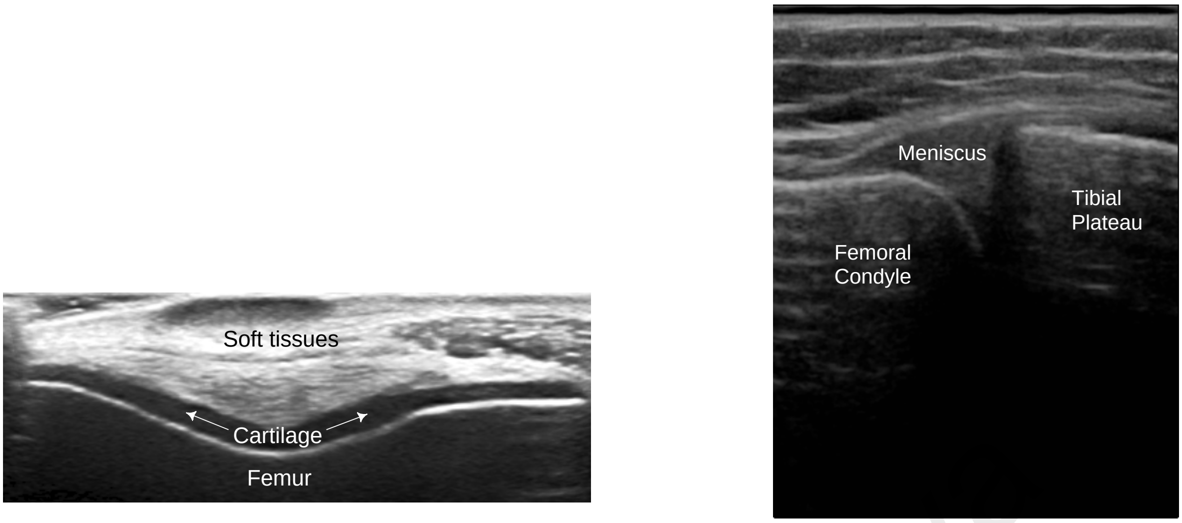

(a) (b)

Figure 1.3: (a) The femoral condylar cartilage and (b) the medial meniscus of the knee joint captured in the 2-D ultrasound images

segmentation of three separate objects of the femoral condyle, the meniscus, and the tibial plateau could determine the meniscus position. Therefore, the goal in the meniscus ultrasound image segmentation is to simultaneously capture the three objects in order to determine the area and position of the meniscus. The segmentation algorithm should locate not only the meniscus, but also the femoral condyle and the tibial plateau. It should be able to prevent merging and overlapping in the shared boundaries of these multiple objects. As a result, segmentation of the multiple objects can be achieved all at once in a single image. As the meniscus may resemble a concave shape, it should penetrate into the boundary concavity and be robust in segmenting objects of different shapes.

Due to the imperfection in the ultrasound image acquisition, speckle and intensity inhomogeneity that occur in the ultrasound images tend to reduce the image contrast. While speckle noise appears as dense, bright and dark granular objects in close proximity throughout the image, intensity inhomogeneity causes a slowly changing intensity contrast where the same tissue region may exhibit contrast variations at several locations and the intensity distributions between different tissues are overlapped significantly. Speckle noise and intensity bias hampered the ultrasound images can cause large variations in image intensities. Spatial intensity variation caused by these multiplicative noises tends to vary the contrast of the object, obscure important details, and make the object difficult to be distinguished in the captured image. They reduce image quality and interpretation, thus, complicate the segmentation task in the ultrasound images. It is desirable to preserve the important details in the ultrasound images that are hampered by the speckle noise and intensity bias. Due to these difficulties, the knee cartilage segmentation and thickness computation and the meniscus segmentation in the 2-D ultrasound images pose a considerable challenge, clinical value, and contribution to the fields of biomedical engineering, medical imaging, and image processing.

1.3 Objectives

The main aim of this thesis is the development of image segmentation algorithms to overcome some challenges available in the knee cartilage and meniscus ultrasound images as an initial step for the quantification of the cartilage degeneration and the meniscus degeneration and displacement. The specific objectives of this thesis are listed below:

1. To develop image segmentation and thickness computation methods in addressing the challenging problems arising in the 2-D knee cartilage ultrasound images.

2. To develop an image segmentation method in dealing with the unique problems associated with the meniscus ultrasound images.

3. To validate the performance of the cartilage segmentation and thickness computation methods and the meniscus segmentation method on real clinical data sets.

1.4 Scope of Work

The scope of this research work includes:

1. The segmentation and thickness computation of the knee cartilage and the segmentation of the meniscus are performed in the 2-D ultrasound images.
2. The performances of the presented methods are compared to other existing methods in the attempt of segmenting the knee cartilage and meniscus ultrasound images.
3. The investigations on several parameters in the presented method are conducted to evaluate their effects on the segmentation accuracy.
4. The performances of the presented methods on real clinical data sets are validated using qualitative and quantitative evaluation metrics.

1.5 Thesis Outline

Chapter 2 provides a brief overview of underlying theory of curve evolution to regulate contour propagation, its implementation using the level set method, and the advantages and disadvantages of the existing active contour models, which are broadly categorized into individual structure segmentation, multiple structure segmentation, and joint segmentation and bias estimation. This chapter also provides an overview on some existing techniques for computing the cartilage thickness.

Chapter 3 explains the methodologies on how to obtain the short-axis knee cartilage and the medial meniscus in the 2-D ultrasound images. The knee cartilage boundary segmentation using locally statistical level set method (LSLSM) and thickness computation using the normal distance method for the 2-D ultrasound images are presented. Multiple active contours using scalable local regional information on expandable kernel (MLREK) for the meniscus ultrasound image segmentation are presented. This chapter also describes qualitative and quantitative segmentation evaluations using Cohen's κ statistics and two validation metrics of Dice similarity coefficient (DSC) and Hausdorff distance (HD) that are used to quantify the segmentation performance, respectively.

Chapter 4 presents qualitative and quantitative evaluations of the cartilage segmentation and thickness computation and the meniscus image segmentation in the 2-D ultrasound images. The performances of LSLSM and two other level set methods in the attempt of segmenting a real knee cartilage ultrasound image are evaluated using DSC and HD metrics. Both qualitative and quantitative evaluations of the three different level set methods on a set of the knee cartilage ultrasound images are performed. The statistics, reproducibility, and agreement of cartilage thickness measurements based on a set of the segmented images using the normal distance are determined and interpreted. Next, segmentation results, convergence properties, computational times of MLREK and other existing active contour methods in their attempt of segmenting the meniscus of the ultrasound image are illustrated using DSC metric. Quantitative evaluations of the sensitivity of each parameter in MLREK to the segmentation results are illustrated using DSC and HD metrics. Segmentation performance of MLREK when applied into a set of the meniscus ultrasound images is validated using both quantitative evaluation metrics.

In Chapter 5, this thesis is finally concluded and some recommendations to guide future works and to further extend the thesis are given.

CHAPTER 2: LITERATURE REVIEW

In this chapter, a review on some of the existing active contour models as one of the image segmentation algorithms that is widely applied in addressing medical image segmentation problems is provided. In Section 2.1.1, the theory of curve evolution to control the contour propagation and its implementation using the level set method are reviewed. Several existing active contour methods and their advantages and disadvantages are explained. In general, they can be further categorized into three classes according to their segmentation purposes: single object segmentation, multiple object segmentation, and joint segmentation and bias estimation and organized into three sections. In Section 2.1.2, the active contour models for the individual structure segmentation are further classified into two categories: local and global active contour models. An overview on the extension of the active contour models in addressing the multiple region segmentation and the joint segmentation and intensity bias correction are given in Sections 2.1.3 and 2.1.4, respectively. In addition, an overview on some existing computational approaches for estimating the cartilage thickness is presented in Section 2.2. Section 2.3 provides a formulation of features required to solve the problems associated with the knee cartilage segmentation and thickness computation and the meniscus segmentation in the 2-D ultrasound images.

2.1 Active Contour Models

Image segmentation is an important task for the purpose of an image understanding. It is often considered as the most difficult step in any automatic image processing systems. In principle, the task of a segmentation algorithm is to partition a given image into meaningful regions that are homogeneous based on the region it represents. It is started with the determination of the distinctive feature that describes each region and differentiates that region with other region. This image feature needs to be captured using a statistical method or some other methods. However, the noise generated due to the imperfection in the image acquisition tends to obscure the captured images thus corrupt the image quality. It makes the segmentation algorithm difficult to distinguish the object, especially when parts of the object region are occluded.

Segmentation algorithms based on active contour methods have grown significantly. These methods have been broadly applied to deal with segmentation problems in the medical images. The segmentation process is started by setting an initial position of the contour. These techniques evolve a smooth and closed contour that separates an image into distinct regions. The contour propagates from its initial position until it arrives at the targeted object boundary within the image domain. The final segmentation outcomes are guaranteed to be continuous closed boundaries with possibly sub-pixel accuracy. These active contour based segmentation methods that fall into the class of variational methods seek to solve complex problems via optimization. In general, an energy functional is associated with the contour's smoothness and the image features. The energy is optimized by solving a gradient flow equation to regulate the contour motion. Such that when the contour coincides with the boundaries, the function should reach its optimum point. The optimization problems yields several benefits. For example, the minimization problem described variationally is easy to understand by analyzing the energy formulation. The solution to the energy minimization does not depend on the implementation of the energy functional where a particular energy minimization framework will result in an identical segmentation outcome.

2.1.1 Theory of Curve Evolution

In general, the evolution of the active contours can be tracked either by the Lagrangian parameterized control points or by the Eulerian level set methods. The contour in Langrangian approach is parameterized discretely in a set of control points distributed at the evolving contour. The contour front is deformed by advancing the control points to the new locations to update the contour position. This approach that is worked explicitly with a parametrized curve is considered as a parametric active contour. Meanwhile, the level set method tracks the curves in a fixed coordinate system of the Eulerian framework. The contour is evolved using geometric measures, i.e., curvature and normal vectors. As opposed to the parametric active contour, the level set method can handle the topological change automatically. Implemented implicitly through level sets, this approach is often called as the geometric active contour. Active contour models for the knee cartilage and meniscus ultrasound image segmentation presented in Chapter 3 are implemented in the level set formulation.

Via minimization the energy functional $E(C)$, the propagating contour $C(s,t) = \begin{bmatrix} x(s,t) \\ y(s,t) \end{bmatrix}$ evolves within an input image, I defined on the image domain, Ω, where $s \in [0, 1]$ parameterizes the contour points, and $t \in [0, \infty)$ represents a set of curves at different time evolutions. A variational approach is formulated for the evolution of a contour, C that minimizes the energy functional $E(C)$ and eventually segments the image. Denote $F(C)$ as an Euler-Lagrange equation where the condition for C to minimize $E(C)$ is that the first derivative of $E(C)$ with respect to the contour C is zero, $F(C) = 0$. The following partial differential equation is to compute the steady state solution to the condition.

$$\frac{\partial C}{\partial t} = F(C). \tag{2.1}$$

In this curve evolution equation, $F(C)$ is seen as the force to push the contour front or the velocity acting in the propagation of the contour C. The force, F has the component $F_{\hat{\mathbf{n}}}$ that directs the contour front in the normal direction and the tangent component $F_{\hat{\mathbf{t}}}$ that navigates the flow along the contour. The component $F_{\hat{\mathbf{n}}}$ has the role to navigate the contour front in the outward or inward direction. This component regulates the evolution of the curve and influences the change in the geometry of the contour. Since the component $F_{\hat{\mathbf{t}}}$ does not change the geometry of the contour, the equation of the curve evolution has only the component of the normal direction such as

$$\frac{\partial C}{\partial t} = F\hat{\mathbf{n}}, \tag{2.2}$$

The Euclidean curve shortening flow in the equation (2.3) is an example that the motion of the contour is influenced by the local properties of the contour, i.e., the curvature along the contour, κ and the unit normal vector of the contour, $\hat{\mathbf{n}}$.

$$\frac{\partial C}{\partial t} = -\kappa\hat{\mathbf{n}}, \tag{2.3}$$

Since the Euclidean arc length of the contour decreases most rapidly, this gradient descent flow has a smoothing effect on the contour. Hence, this flow is used to regulate the smoothness of the contour and enforces a jagged contour become smoother. If the contour is evolved under this flow only, it will shrink, forming a circle shape, and then a point. At the end, the contour will vanish.

Another flow demonstrates the motion of the contour under constant speed that grows and shrinks the contour, given by

$$\frac{\partial C}{\partial t} = \omega\hat{\mathbf{n}}, \tag{2.4}$$

where ω is a constant. This constant flow corresponds to the minimization of the contour's area. If ω is negative, the contour evolves in an outward direction. If ω is positive, the contour will move inward.

Starting with the position of an initial contour, C_0 and the evolution equation as defined in the equation (2.1), the level set technique is used to track the contour as it propagates. The propagating contour $C(t) \subset \Omega$ is implicitly represented by the level set function at time, t. The contour is embedded in the zero level of a function $\phi(\mathbf{x}) : \Omega \rightarrow \Re$ where $\Re$ is the Real numbers.

$$C(t) = \{\mathbf{x} \in \Omega : \phi(\mathbf{x}, t) = 0\} \text{ with } C_0 = \phi(\mathbf{x}, t = 0), \tag{2.5}$$

where C_0 is the initial contour. Given an initial level set function $\phi(\mathbf{x}, t = 0)$, the function $\phi(t)$ is evolved to move its zero level set based on the motion of the contour.

In the two-phase case, the image domain Ω is partitioned into two separate regions Ω_1 and Ω_2. In this case, a level set function ϕ that has positive sign inside the contour and negative sign outside the contour is used to represent a partition of the image domain Ω into the two regions Ω_1 and Ω_2, given by

$$\text{inside}(C) = \Omega_1 = \{\mathbf{x} \in \Omega : \phi(\mathbf{x}, t) > 0\}, \tag{2.6}$$

$$\text{outside}(C) = \Omega_2 = \{\mathbf{x} \in \Omega : \phi(\mathbf{x}, t) < 0\}, \tag{2.7}$$

The image pixels that are in the interior, exterior, and on the contour are represented with the following the membership functions, M_i. For instance, the image regions inside or on the contour are represented by the function $M_1(\phi) = H(\phi)$. The image pixels outside the contour are represented by the function $M_2(\phi) = 1 - H(\phi)$. The pixels that are on the contour C are represented by the first derivative of $H(\phi)$, the Dirac delta function $\delta(\phi) = H'(\phi)$. To facilitate numerical implementation, the regularized Heaviside function $H_\epsilon(\phi)$, $(1 - H_\epsilon(\phi))$, and the derivative of the Heaviside function, the smoothed Dirac delta function $\delta_\epsilon(\phi)$, are often used to represent the regions inside, outside, and around the contour, respectively. $H_\epsilon(\phi)$ and $\delta_\epsilon(\phi)$ are computed by the equations (2.8) and (2.9) with

$\epsilon = 1$ as in (T. F. Chan & Vese, 2001), respectively.

$$H_\epsilon(\phi) = \frac{1}{2}\left(1 + \frac{2}{\pi}\arctan\left(\frac{\phi}{\epsilon}\right)\right), \tag{2.8}$$

$$\delta_\epsilon(\phi) = \frac{1}{\pi}\left(\frac{\epsilon}{\epsilon^2 + \phi^2}\right). \tag{2.9}$$

By defining that the level set function, ϕ has positive values inside the contour and negative values outside the contour, the unit normal vector of the contour, $\hat{\mathbf{n}}$ will push the contour inward as given by

$$\hat{\mathbf{n}} = \frac{\nabla\phi}{|\nabla\phi|}, \tag{2.10}$$

In addition, the curvature of the contour, κ is defined by

$$\kappa = \mathrm{div}(\hat{\mathbf{n}}) = \mathrm{div}\left(\frac{\nabla\phi}{|\nabla\phi|}\right), \tag{2.11}$$

where $\mathrm{div}(\cdot)$ represents the divergence. This term affects the contour's smoothness. The curvature of the contour is positive if the unit normal vectors diverge. Meanwhile, the curvature is negative when the unit normal vectors converge.

2.1.2 Single Object Segmentation

There have been several active contour models proposed for the purpose of single object segmentation. They can be further categorized into local and global active contour methods. In segmenting the desired boundary, the global models consider entire image intensities (T. F. Chan & Vese, 2001; Li, Kao, Gore, & Ding, 2008), whereas the local models employ either local edge pixels (Casseles, Kimmel, & Sapiro, 1997) or local intensity pixels (Lankton & Tanenbaum, 2008; Darolti, Mertins, Bodensteiner, & Hoffman, 2008). A brief summary of existing models that use edge information, global regional intensity information, and local regional intensity information is provided. The edge-based, the global regional, the local regional active contour methods are briefly described and its advantages and disadvantages are discussed in this section.

The object's edge is one of the image features that is often applied to partition the image. For instance, geodesic active contour (GAC) relies on discontinuity between distinct regions. GAC computes the image gradient priory and uses the obtained edge pixels as the boundary candidates. In GAC, the arc length of the curve is represented as a line integral, $L_C = \oint |C'(s)|\, ds = \oint dr$. The length element dr is weighted by an edge indicator, g given in (2.13). Casseles et al. (1997) expressed the energy functional of GAC as follows

$$\begin{aligned} E_{\mathrm{GAC}}(C(s)) &= \int_0^1 g(\nabla I(C(s)))dr, \\ &= \int_0^1 g(\nabla I(C(s)))\,|C'(s)|\, ds, \end{aligned} \tag{2.12}$$

where

$$g(|\nabla I|) = \frac{1}{1 + |\nabla G_\sigma * I|^p}, p = 1 \text{ or } 2, \tag{2.13}$$

where ∇ denotes the gradient operator and $*$ is the convolution operator. Since the force on the contour front is regulated by such image gradient, the contour will propagate gradually either in the inward or outward direction. The contour will finally converge at the strong edges when the magnitude of the motion forces, $g(|\nabla I|)$, gives the smallest value.

The image gradient or edge map is non-zero at rapid intensity changes, supposedly the actual boundaries that separate distinct regions. Spatial intensity variation such as non-uniform background may disappear while rapid intensity change is converted into the edges. The edge-based models do not consider the global information of the image intensity. When strong edge pixels exist, a satisfactory segmentation outcome can still be obtained in the presence of non-uniform or heterogeneous textures. However, not only the boundaries but also the noises attribute as rapid intensity changes. To reduce the sensitivity to noise, σ of the Gaussian smoothing function may be tuned with larger values. However, it results in the blurring the true boundaries, making the contour pass through noises and weak boundaries. These turn out to be complicated problems because solving one usually leads to another problem.

The energy functional in the equation (2.12) is minimized by searching the path of the shortest length $\oint dr$, which also takes into account the image features. The evolution equation of GAC is expressed as

$$\frac{\partial C}{\partial t} = g(|\nabla I|)\kappa\hat{\mathbf{n}} - (\nabla g(|\nabla I|) \cdot \hat{\mathbf{n}})\hat{\mathbf{n}}, \tag{2.14}$$

GAC added the balloon force or constant motion term ω into its formulation and expressed the level set formulation as follows

$$\begin{aligned} \frac{\partial \phi}{\partial t} &= g(|\nabla I|)|\nabla \phi| \mathrm{div}\left(\frac{\nabla \phi}{|\nabla \phi|}\right) + \nabla g(|\nabla I|) \cdot \nabla \phi + \omega g(|\nabla I|)|\nabla \phi|, \\ &= g(|\nabla I|)|\nabla \phi|(\kappa + \omega) + \nabla g(|\nabla I|) \cdot \nabla \phi, \end{aligned} \tag{2.15}$$

Since the value of g is never zero at the edges that have a large variation, the contour may not completely stop at the intended boundary. The gradient term $\nabla g \cdot \nabla \phi$ that is naturally incorporated in the GAC has a strong attraction to drive the contour towards the real boundary. This gradient term prevents the contour from surpassing the weak edges. The term ∇g helps the contour to stop exactly at the middle of the edge pixels. Nonetheless, this gradient term evolves the contour with a slow convergence and a small capture range.

In order to gain a faster convergence and a larger capture range, an additional balloon force ω is placed into the formulation of GAC. The term $\omega g(|\nabla I|)|\nabla \phi|$ has a role to inflate or deflate the contour at a constant velocity. The value of this constant velocity will determine the speed of the contour motion while its sign will control the inward or outward direction of the contour motion. However, this constant flow introduces an undesired property, i.e., sensitivity to initial contour placement. If the sign of ω is set as positive, the initial contour has to be placed outside the object so that the contour will deflate. If the sign of ω is negative, then the initial contour needs to be put entirely inside the object so that the contour will inflate. If the constant ω is removed, the initial contour can be placed both inside and outside the object. The contour will grow and shrink simultaneously, however, with a slower convergence and a small capture range.

To overcome these classical drawbacks of the edge-based methods, i.e., sensitivity to noise and initial contour placement, the region-based models use statistics of several pixels within regions as a force to attract the contour to the boundary. Since these models rely on the regional statistics, they are less sensitive to the noise and the placement of the initial contour than the edge-based models.

Mumford and Shah (1989) proposed the piecewise smooth model that provides a theoretical framework for global regional image segmentation. This framework is later independently implemented using the level set method (Osher & Sethian, 1988) by Tsai, Yezzi, and Willsky (2001); Vese and Chan (2002). The piecewise smooth model of Mumford and Shah assumes smooth and slowly varying region; whereas, its simplification, the piecewise constant model of T. F. Chan and Vese estimates the regions by constants intensity averages on either image regions delimited by the contour. The minimization of this energy is obtained when the regions are optimally estimated by the means. Later, J. A. Yezzi, Tsai, and Willsky (2002) added the regional variances to the model's statistics. Michailovich, Rathi, and Tannenbaum (2007) minimize the probability density functions of intensity histograms on two sides of the contour. Note that the aforementioned models utilize the global intensity fitting function and the regional statistics both sides the contour as a clue to find the boundary. Hence, they are called as the global region-based models.

In general, the energy functional $E(\phi)$ is comprised of the contour's smoothness and the image features. The energy functions e_i that represent an image partition are combined with M_i to be incorporated into the level set formulation. The total energy functional can be expressed as

$$E(\phi) = \nu \int_{\Omega} |\nabla H_{\epsilon}(\phi_i(\mathbf{x}))| d\mathbf{x} + \int_{\Omega} \sum_{i=1}^{2} e_i(\mathbf{x}) M_i(\phi(\mathbf{x})) d\mathbf{x}, \tag{2.16}$$

where ν is a constant to regulate the contour's smoothness.

Minimization of the energy functional E is equivalent to solving the gradient flow equation given by

$$\frac{\partial \phi}{\partial t} = \delta_{\epsilon}(\phi) \left[\nu \mathrm{div} \left(\frac{\nabla \phi}{|\nabla \phi|} \right) - e_1 + e_2 \right], \tag{2.17}$$

where div$(\cdot)$ represents the divergence and δ_{ϵ} is the smoothed delta function defined in the equation (2.9).

T. F. Chan and Vese (2001) proposed active contours without edges (ACWE) under the assumption of the statistically homogeneous image intensities. The image is segmented into two disjoint regions delimited by the contour approximated by the piecewise constant intensities for $i = 1, 2$. The functions e_i for this method is defined by

$$e_i^{\mathrm{ACWE}}(\mathbf{x}) = |I(\mathbf{x}) - \mu_i(\mathbf{y})|^2, \tag{2.18}$$

where μ_i are the constants of the intensity means of the image pixels $I(\mathbf{x})$ either side of the contour given by

$$\mu_i(\mathbf{y}) = \frac{\int_{\Omega} M_i(\phi(\mathbf{x})) I(\mathbf{x}) d\mathbf{x}}{\int_{\Omega} M_i(\phi(\mathbf{x})) d\mathbf{x}}, i = 1, 2. \tag{2.19}$$

ACWE utilizes the global intensity fitting function and the entire image intensities to partition the image. This method also assumes intensity homogeneity of the image to be segmented. The assumption of the piecewise constant intensity in each region is not applicable to segment images corrupted by intensity inhomogeneities.

To deal with intensity inhomogeneity, Li et al. (2008) presented region-scalable fitting (RSF) model using sliding fixed-scale Gaussian kernels into image regions on either side of the contour. The scalable kernel allows approximation of means intensity at a certain regional scale from small to large scale. Utilizing entire image feature on either region of the contour, the region-scalable data fitting function behaves as a gravitational field to partition the image into several regions represented by the contour. While ACWE estimates the image intensities in the entire domain and does not have a choice to approximate the intensities in the local region, RSF provides the choice of the scale in the local region and in the entire image domain. The functions e_i of RSF in (Li et al., 2008) is given below

$$e_i^{\mathrm{RSF}}(\mathbf{x}) = \int_\Omega K(\mathbf{y}-\mathbf{x})\,|I(\mathbf{x}) - \mu_i(\mathbf{y})|^2\,d\mathbf{y}, \tag{2.20}$$

where μ_i for $i = 1, 2$ are weighted intensity means in a neighborhood of $\mathbf{y}$, whose the size is proportional to the scale of the kernel function K. A truncated Gaussian function is chosen as the kernel function.

$$\mu_i(\mathbf{y}) = \frac{\int_\Omega (I(\mathbf{x})M_i(\phi(\mathbf{x})) * K(\mathbf{y}-\mathbf{x}))d\mathbf{x}}{\int_\Omega (M_i(\phi(\mathbf{x})) * K(\mathbf{y}-\mathbf{x}))d\mathbf{x}}. \tag{2.21}$$

RSF relies only on the local intensity means to cope with intensity inhomogeneity. In order to distinguish regions that have the same intensity means, but different variances, the local Gaussian distribution fitting (LGDF) method uses a Gaussian distribution of the local image intensities where the means and variances are different. L. Wang, He, Mishra, and Li (2009) expressed the function e_i of LGDF as follows

$$e_i^{\mathrm{LGDF}}(\mathbf{x}) = \int_{\Omega} K(\mathbf{y}-\mathbf{x})\left(\frac{|I(\mathbf{x})-\mu_i(\mathbf{y})|^2}{2\sigma_i^2} + \frac{\log(2\pi\sigma_i^2)}{2}\right)d\mathbf{y}, \tag{2.22}$$

where the local intensity means, μ_i for $i = 1, 2$ are defined by

$$\mu_i(\mathbf{y}) = \frac{\int_{\Omega}(K(\mathbf{y}-\mathbf{x})I(\mathbf{x})M_i(\phi(\mathbf{x}))) d\mathbf{x}}{\int_{\Omega}(K(\mathbf{y}-\mathbf{x})M_i(\phi(\mathbf{x}))) d\mathbf{x}}, \tag{2.23}$$

and the variances σ_i^2 are given by

$$\sigma_i^2 = \frac{\int_{\Omega} K(\mathbf{y}-\mathbf{x})\,|I(\mathbf{x})-\mu_i(\mathbf{y})|^2\, M_i(\phi(\mathbf{x}))d\mathbf{x}}{\int_{\Omega} K(\mathbf{y}-\mathbf{x})M_i(\phi(\mathbf{x}))d\mathbf{x}}. \tag{2.24}$$

The robustness of global region-based methods to contour initialization tends to locate whole image structures where different positions of the initial contour will evolve into an identical final contour location (T. F. Chan & Vese, 2001; Li et al., 2008). The sensitivity of the local active contour methods to contour initialization limits the initial contour to be put near the object (Casseles et al., 1997; Lankton & Tanenbaum, 2008). This condition allows segmentation of objects with different locations by putting different initial contour positions. Therefore, locating an object boundary from surrounding objects is allowed using these local active contour methods. As the image noise causes fault edges, it often impedes the edge-based active contour methods to converge into the desired boundary. The insensitivity of the regional active contour methods against image noises is more likely to produce satisfactory result as it uses pixel intensities instead of edge pixels.

As opposed to global active contour methods that may produce poor segmentation due to overlapped probability densities in images with intensity homogeneity between the foreground and the background, the local regional active contours reduce the overlapping distribution, analogously to the local edge assumption. Several active contour methods using the local regional descriptor have been proposed such as localizing region-based active contour (LRAC) (Lankton & Tanenbaum, 2008) and local region descriptors (LRD) for active contour evolutions (Darolti et al., 2008). LRAC and LRD employ local regional statistics within fixed-radius balls and fixed-scale square windows distributed on the evolving contour, respectively. These local regional models try to locate the boundaries by gradually deforming the contour similar to those in the edge-based models.

The function e_i of LRAC in (Lankton & Tanenbaum, 2008) is written as

$$e_i^{\mathrm{LRAC}}(\mathbf{x}) = \int_\Omega B(\mathbf{y}-\mathbf{x})\delta_\epsilon(\phi(\mathbf{y})) \cdot \left|I(\mathbf{x}) - \mu_i^B(\mathbf{y})\right|^2 d\mathbf{y}, \tag{2.25}$$

where $B(\mathbf{y}-\mathbf{x})$ is the ball mask with radius r centered at the contour, defined as

$$B(\mathbf{y},\mathbf{x}) = \begin{cases} ,1, & ||\mathbf{y}-\mathbf{x}|| < r \\ 0, & \text{otherwise,} \end{cases} \tag{2.26}$$

and the local intensity averages μ_i inside and outside of the contour localized by $B(\mathbf{y}-\mathbf{x})$ at a point $\mathbf{x}$ given by

$$\mu_i^B(\mathbf{y}) = \frac{\int_\Omega B(\mathbf{y}-\mathbf{x}) \cdot M_i(\phi(\mathbf{x})) \cdot I(\mathbf{x}) d\mathbf{x}}{\int_\Omega B(\mathbf{y}-\mathbf{x}) \cdot M_i(\phi(\mathbf{x})) d\mathbf{x}}, i = 1, 2. \tag{2.27}$$

LRAC and LRD estimate local intensity, but do not accommodate any scale choice to measure region with various sizes. In LRAC, the scale has to be manually set according to the distance between the locations of the initial contour and the object. If the scale is too small and the initial contour is put further from the nearest boundary, the contour may not be able to penetrate into the boundary concavity. As the meniscus resembles a concave shape, LRAC may have problems in completely penetrating the boundary. To cope with the local minima problem, LRD added the constant motion and two segmenter functions. However, it requires the initial contour to be put entirely within the object of interest.

Later, Phumeechanya, Pluempitiwiriyawej, and Thongvigitmanee (2010) proposed active contour using local regional information on extendable search line (LRES). LRES utilizes extendable search lines to reach the boundary concavity. Phumeechanya et al. (2010) expressed the function e_i of LRES as follows

$$e_i^{\text{LRES}}(\mathbf{x}) = \int_{\Omega} L(\mathbf{y},\mathbf{x})\delta_{\epsilon}(\phi(\mathbf{y})) \cdot \left|I(\mathbf{x}) - \mu_i^L(\mathbf{y})\right|^2 d\mathbf{y}, \tag{2.28}$$

where $L(\mathbf{x},\mathbf{y})$ is the search line spread at the contour front given by

$$L(\mathbf{y},\mathbf{x}) = \begin{cases} 1, & (\mathbf{y},\mathbf{x}) \text{ is on the search line}, \\ 0, & \text{otherwise}, \end{cases} \tag{2.29}$$

and the local intensity averages μ_i in both sides of the contour localized by $L(\mathbf{y}-\mathbf{x})$ defined by

$$\mu_i^L(\mathbf{y}) = \frac{\int_{\Omega} L(\mathbf{y},\mathbf{x}) \cdot M_i(\phi(\mathbf{x})) \cdot I(\mathbf{x})d\mathbf{x}}{\int_{\Omega} L(\mathbf{y},\mathbf{x}) \cdot M_i(\phi(\mathbf{x}))d\mathbf{x}}, i = 1, 2. \tag{2.30}$$

LRES has a flexibility to extend the search line reaching the intended boundary where the intensity statistics is estimated on the adaptive-length search lines. However, the area of the search lines is not proportional to the image size. Insufficient statistics computed within the lines may drive the contour to the wrong direction. In addition, it needs more computational cost to form and extend two line regions either side of the contour.

Another active contour is driven by local region-scalable force with expandable kernel (LREK) (Faisal & Pluempitiwiriyawej, 2012). It utilizes pixel intensity values within scalable kernels distributed on the contour front. The kernels expand gradually until a boundary is detected. Therefore, the kernels are to drive the contour to reach the object's boundary. The function e_i of LREK is defined by

$$e_i^{\mathrm{LREK}}(\mathbf{x}) = \int_\Omega K(\|\mathbf{y}-\mathbf{x}\|)\delta_\epsilon(\phi(\mathbf{y})) \times |I(\mathbf{x}) - \mu_i^K(\mathbf{y})|^2 d\mathbf{y}. \tag{2.31}$$

where the kernel function is chosen as the uniform kernel. The intensity averages within the interior and exterior areas of the expandable kernel $K(\mathbf{y}-\mathbf{x})$ are given by

$$\mu_i^K(\mathbf{y}) = \frac{\int_\Omega K(\|\mathbf{y}-\mathbf{x}\|)M_i(\phi(\mathbf{x}))I(\mathbf{x})d\mathbf{x}}{\int_\Omega K(\|\mathbf{y}-\mathbf{x}\|)M_i(\phi(\mathbf{x}))d\mathbf{x}}. \tag{2.32}$$

In LREK, one kernel region is used to form inner and outer regions split by the contour line. Thus, instead of two local regions, only one kernel region needs to be expanded. This helps LREK to arrive at the object's boundary faster than some other models. Moreover, the scalability of the kernel region to the image area results in a proportional computation in both small and large images.

2.1.3 Multiple Object Segmentation

The active contour models have been extended to handle multiple structure segmentation using global regional information (Vese & Chan, 2002; Brox & Weickert, 2006). For instance, the framework in (Vese & Chan, 2002) represents $N = 2^n$ regions using n-level set functions. In the case of $N = 4$, two level set functions ϕ_1 and ϕ_2 are used to define $M_1(\phi_1, \phi_2) = H(\phi_1)H(\phi_2)$, $M_2(\phi_1, \phi_2) = H(\phi_1)(1 - H(\phi_2))$, $M_3(\phi_1, \phi_2) = (1 - H(\phi_1))H(\phi_2)$, and $M_4(\phi_1, \phi_2) = (1 - H(\phi_1))(1 - H(\phi_2))$ to give a four-phase level set formulation. The level set functions partition the image into two subdomains. An additional constraint is not necessary to handle junctions between multiple contours as the junctions itself represent the regions to be segmented.

The level set functions $\phi_1, \cdots, \phi_n$ are denoted by a vector valued function $\Phi =$

$(\phi_1, \cdots, \phi_n)$. Therefore, the membership functions $M_i(\phi_1, \cdots, \phi_n)$ are expressed as $M_i(\Phi)$. For the multiphase case ($N > 2$), the energy $E(\Phi)$ is expressed in the following multiphase level set formulation

$$E(\Phi) = \nu \int_\Omega |\nabla H_\epsilon(\Phi(\mathbf{x}))| d\mathbf{x} + \int_\Omega \sum_{i=1}^{N} e_i(\mathbf{x}) M_i(\Phi(\mathbf{x})) d\mathbf{x}, \tag{2.33}$$

where e_i for $i = 1, \cdots, N$ is defined as in the equation (2.18).

The energy minimization of $E(\Phi)$ with respect to variable $\Phi = (\phi_1, \cdots, \phi_n)$ is performed by solving the following gradient flow equations:

$$\frac{\partial \phi_j}{\partial t} = \nu \delta_\epsilon(\phi_j) \mathrm{div}\left(\frac{\nabla \phi_j}{|\nabla \phi_j|}\right) - \sum_{i=1}^{N} \frac{\partial M_i(\phi_j)}{\partial \phi_j} e_i. \tag{2.34}$$

In the case that the number of regions is a power of two, this multiphase level set method adopts the property of the two-phase level set method. It implicitly respects the constraint of separate regions and thus does not need coupling forces. When the number of the regions is not a power of two, a particular region has twice weights. It will produce empty regions, which does not fit with the piecewise constant model.

Instead of assigning n-level set functions to segment $N = 2^n$ regions, multiple level set functions are used to deal with multi structure segmentation where a disjoint level set function ϕ_j is assigned to represent every region Ω_i. This multiphase level set method requires a coupling force to consider the constraint of separate regions. Such that the regions are not overlapping each other and the pixels are not assigned to any region.

The coupled level set approach for multiphase motion in (Zhao, Chan, Merriman, & Osher, 1996) added a constraint to handle junctions formed in between multiple level set functions. The constraint of separate regions is combined by means of a Lagrangian multiplier, λ. The third term is placed in addition to the length and area terms in their energy functional. In the gradient flow equation, the third term prevents the growth of the overlapping regions between the adjacent contour. As this term forces the junctions to disappear, the neighbouring contours share the boundary.

$$E(\Phi) = \nu \int_{\Omega} |\nabla H_{\epsilon}(\Phi(\mathbf{x}))| d\mathbf{x} + \int_{\Omega} \sum_{i=1}^{N} e_i(\mathbf{x}) M_i(\Phi(\mathbf{x})) d\mathbf{x} + \frac{\lambda}{2} \int_{\Omega} (H_{\epsilon}(\Phi(\mathbf{x})) - 1)\, d\mathbf{x}, \quad (2.35)$$

where e_i for $i = 1, \cdots, N$ is defined as in the equation (2.18).

$$\frac{\partial \phi_j}{\partial t} = \nu \delta_{\epsilon}(\phi_j) \mathrm{div}\left(\frac{\nabla \phi_j}{|\nabla \phi_j|}\right) - \sum_{i=1}^{N} \frac{\partial M_i(\phi_j)}{\partial \phi_j} e_i - \lambda \delta_{\epsilon}(\phi_j) \left(\sum_{k=1}^{n} H_{\epsilon}(\phi_k) - 1\right), \quad (2.36)$$

where λ is a Lagrange multiplier and $1 \leq j < k \leq n$.

In (Brox & Weickert, 2006), each object's region is assigned by one level set function. Each level set function ϕ_j is evolved such that every point in the domain is inside the contour. To achieve this goal, every ϕ_j evolves according to

$$\frac{\partial \phi_j}{\partial t} = \delta_{\epsilon}(\phi_j) \left(e_i(\phi_j) - \max_{\delta_{\epsilon}(\phi_j)>0, k\neq j} \left(e_i(\phi_k), e_i(\phi_j) - 1\right)\right), \quad (2.37)$$

where e_i is defined as in the equation (2.18).

The coupled contours are allowed to compete with adjacent contours at an interface. The contours interact with themselves when only one contour and no competing region nearby exists. The neighboring contours move simultaneously based on the strongest retreat force. In the situations where there are no other contours in the surrounding, a balancing term $e_j - 1$ will direct the contour towards the empty region with a constant velocity. Thus, it allows the contour to grow, but prevent overlaps. When the number of regions is not a power of two, there are no empty regions and no varying weights for the length constraint. This behavior is suitable to be used by the global region-based models.

Lankton and Tanenbaum (2008) formulated the multiple level set scheme using the local region descriptor for multiple region segmentation. Inspired by the work of Brox and Weickert, Lankton and Tanenbaum (2008) modified the multiple level set scheme using the assumption of competing region. It is realized by combining the advance and retreat forces given as follows

$$\frac{\partial \phi_j}{\partial t} = \delta_\epsilon(\phi_j)\left(\max_{\delta_\epsilon(\phi_j)>0, k\neq j} \big(e_1(\phi_j) + e_2(\phi_k)\big) + \min_{\delta_\epsilon(\phi_i)>0, k\neq j} \big(-e_1\left(\phi_j\right) - e_2(\phi_k)\big)\right), \quad (2.38)$$

where e_i for $i = 1, 2$ is defined as in the equation (2.25).

This formulation consists of advance and retreat competing components. The contours propagate based on the relative magnitude of the advance component and the retreat component. The advance component has a positive value to grow the contour outward along its normal. On the other hand, the retreat component has a negative value to grow the contour in the inward direction. The advance force of one contour competes with the corresponding retreat forces of the adjacent contours and vice versa. Thus, the coupled contours will interact at the interface and move simultaneously based on the strongest force, while uncoupled contours will keep evolving.

2.1.4 Joint Segmentation and Intensity Bias Estimation

Spatial intensity variation that cause changes in the image intensity may complicate the task of image segmentation. When spatial intensity variation caused by intensity inhomogeneity is considered and not the one caused by speckle, the problem of intensity inhomogeneity can be addressed similar to the intensity bias correction in MRI images (Xiao, Brady, Noble, & Zhang, 2002). It is applied retrospectively in the acquired images and also often combined with the segmentation methods, for which, several active contour methods have been extended to handle simultaneous multiphase segmentation and bias estimation of MRI images (Li et al., 2011; K. Zhang, Zhang, & Zhang, 2010; K. Zhang, Zhang, Lam, & Zhang, 2016; X.-F. Wang, Min, Zou, & Zhang, 2015; X.-F. Wang, Min, & Zhang, 2015; Mukherjee & Acton, 2015) where its implementation in total variational model offers even more efficient performance (H. Zhang, Ye, & Chen, 2013). Li et al. (2011); K. Zhang et al. (2010, 2016) used the multiple level set framework in (Vese & Chan, 2002) to represent the subregions.

To segment images corrupted by intensity bias, the energy proposed by Li et al. (2011) is formulated according to the multiplicative noise model of intensity inhomogeneity. To form separable clusters, image intensities I are defined in a local region and approximated by mean bc_i, which are the product of the bias field and constants, respectively. An energy functional is formed by integrating the local clustering criterion with the membership functions, M_i. This energy functional represents an image partition and the bias field that considers the intensity inhomogeneity. The kernel function, K, chosen as a truncated Gaussian function, defines the local region at a certain scale. This method is referred as the locally weighted K-means variational level set method (WKVLS). WKVLS defines its energy functional E in the first row of the equation (2.39). It can also be computed using the equivalent expression given in the second row of the equation the (2.39).

$$\begin{aligned} e_i^{\mathrm{WKVLS}}(\mathbf{x}) &= \int_\Omega K(\mathbf{y}-\mathbf{x})\,|I(\mathbf{x}) - b(\mathbf{y})c_i|^2\,d\mathbf{y}, \\ &= I^2\mathbf{1}_K - 2c_i I(b*K) + c_i^2(b^2*K). \end{aligned} \tag{2.39}$$

Via energy minimization of the energy functional E, estimation of the membership functions M_i, the bias field b that estimates the intensity inhomogeneity, and the constants c_i that approximate the true image pixels in each region are obtained. Therefore, image segmentation and bias field correction are performed together, where the results are given by the level set function ϕ and the restored bias field b, respectively. Meanwhile, the multiplicative components of the image I: the variables c_i and b that minimize E are accordingly defined by

$$c_i(\mathbf{x}) = \frac{\int_\Omega (b(\mathbf{y}) * K(\mathbf{y}-\mathbf{x}))I(\mathbf{x})M_i(\phi(\mathbf{x}))d\mathbf{y}}{\int_\Omega (b^2(\mathbf{y}) * K(\mathbf{y}-\mathbf{x}))M_i(\phi(\mathbf{x}))d\mathbf{y}}, \tag{2.40}$$

and

$$b(\mathbf{y}) = \frac{\sum_{i=1}^N (I(\mathbf{x})M_i(\phi(\mathbf{x})) * K(\mathbf{y}-\mathbf{x}))}{\sum_{i=1}^N (M_i(\phi(\mathbf{x})) * K(\mathbf{y}-\mathbf{x}))}. \tag{2.41}$$

K. Zhang et al. (2010, 2016) proposed statistical variational multiphase level set method (SVMLS) for joint MRI tissue segmentation and bias estimation. The energy is derived according to Gaussian distributions of local image intensity and multiplicative noise model. Local intensities within a neighborhood are approximated by Gaussian distributions with mean bc_i and variance σ_i^2. The kernel function, K, is set as a uniform function. This is to ensure the intensities involved only in the local neighborhood. The energy functional E of SVMLS is written as follows

$$e_i^{\text{SVMLS}}(\mathbf{x}) = \int_\Omega K(\mathbf{y}-\mathbf{x})\left(\frac{|I(\mathbf{x}) - b(\mathbf{y})c_i|^2}{2\sigma_i^2} + \frac{\log(2\pi\sigma_i^2)}{2}\right)d\mathbf{y}. \tag{2.42}$$

Via energy minimization of the energy functional E with respect to the constants, c_i, the restored bias field, b, and the variances, σ_i, the variables ϕ, c_i, b, and σ_i are jointly estimated during the evolution of ϕ. Each variable is defined by

$$c_i(\mathbf{x}) = \frac{\int_\Omega (b * K)IM_i(\phi)d\mathbf{y}}{\int_\Omega (b^2 * K)M_i(\phi)d\mathbf{y}}, \tag{2.43}$$

$$b(\mathbf{y}) = \frac{\sum_{i=1}^N \frac{c_i}{\sigma_i^2}(IM_i(\phi) * K)}{\sum_{i=1}^N \frac{c_i^2}{\sigma_i^2}(M_i(\phi) * K)}, \tag{2.44}$$

and

$$\sigma_i^2 = \frac{\int_\Omega K(\mathbf{y}-\mathbf{x}) \left| I(\mathbf{x}) - b(\mathbf{y})c_i \right|^2 M_i(\phi(\mathbf{x}))d\mathbf{x}}{\int_\Omega K(\mathbf{y}-\mathbf{x}) M_i(\phi(\mathbf{x}))d\mathbf{x}}. \tag{2.45}$$

Both methods were essentially designed to simultaneously estimate the multiplicative bias field while segmenting MRI images. While these intensity-based segmentation techniques are generally insensitive to noise, the use of local image intensity and simultaneous intensity bias estimation help to cope with the intensity inhomogeneity. But different from WKVLS, where each cluster approximates the intensities by the local intensity means, SVMLS assumes the local intensities to be Gaussian distributed to optimize the means and the variances. SVMLS is more general than WKVLS that assumes Gaussian distributions with a fixed variance. WKVLS ignores the variance component that is taken into account in SVMLS, which helps to distinguish different tissues more accurately. Although developed for another imaging modality, SVMLS is suitable and can be adapted as a technique for locating the cartilage boundary in the ultrasound images. It has been explained in (Xiao et al., 2002) that the underlying assumption of the multiplicative noise model is related to the classic reflection imaging equation of ultrasound physics of image formation.

2.2 Cartilage Thickness Computation

Ultrasound imaging has been used to measure the thickness and detect the degenerative change in the cartilage (Aisen et al., 1984) in patients with knee pain (Kazam et al., 2011), osteoarthritis, and rheumatoid arthritis (Iagnocco, Coari, & Zoppini, 1992) where the measurement of the cartilage thickness was performed manually by drawing the perpendicular line between hyperechoic lines of the soft tissue-cartilage interface and of the cartilage-bone interface (Kazam et al., 2011; Naredo et al., 2009).

Several computational approaches have been proposed for estimating the cartilage thickness in 3-D MRI images (Fripp et al., 2010; Tang et al., 2006; Solloway, Hutchison, Waterton, & Taylor, 1993). The thickness computation was performed on the 3-D cartilage surface obtained from a 3-D reconstruction of segmented sagittal knee cartilage slices or a direct 3-D MRI cartilage segmentation. Vertical distance is a simple thickness measurement providing z-directional distance between points on the upper and lower surfaces (Heuer, Sommer, III, & Bottlang, 2001). Proximity method computes the closest neighbour on corresponding surface. It reflects the distance that is closest from each point on a given surface to the point on the opposing surface (Fripp et al., 2010; Maurer, Qi, & Raghavan, 2003). Another class of methods defines the thickness relative to a central axis. The thickness is treated as the distance between the points on the medial axis that is perpendicular to the axis intersected with the upper and lower surfaces (Solloway et al., 1993). This method generates the normal to an average surface of the two surfaces and then calculates the distance between two points where the vector intersects the two surfaces (Solloway et al., 1993). Hence, it does not measure a true normal thickness (Tang et al., 2006). In (A. Yezzi & Prince, 2003), the length of streamlines approaching the opposing boundary from a normal direction is defined as the thickness. Instead of using the streamlines, the normal distance calculates the thickness from the length of the straight line of the normal vectors among the two surfaces (Tang et al., 2006). It provides the true normal thickness from one surface to another that yielded the most accurate estimation (Heuer et al., 2001).

2.3 Summary

The two-phase case of SVMLS or referred as the locally statistical level set method (LSLSM) is considered to address single object segmentation and bias field estimation in the 2-D knee cartilage ultrasound images. LSLSM is applied in segmenting the cartilage boundary from the surrounding tissues that is not sufficiently distinct and hampered by spatial intensity variation caused by speckle and intensity inhomogeneity. Since the energy functional of LSLSM is derived from Gaussian distributions of local image intensity and multiplicative noise model, LSLSM is suitable to cope with a noisy and bias-corrupted image. The variance component of the Gaussian distribution helps to distinguish different tissues between the cartilage interfaces more accurately. The normal distance is adopted as a technique for computing the cartilage thickness in the 2-D ultrasound images, which provides the true normal thickness and the most accurate estimation. The cartilage thickness between the two interfaces is measured by averaging the normal distance along the 2-D segmented cartilage area.

To deal with the meniscus ultrasound image segmentation that requires simultaneous segmentation of the femoral condyle, the meniscus, and the tibial plateau, a multiple active contours framework that uses scalable local regional information on expandable kernel or called multiple LREK active contours (MLREK) is applied. Using scalable local regional information on expandable kernel, the kernel is of adaptive scale in order to prevent multiple contours being stuck locally in a homogeneous region and thus navigate the contours towards the object's boundaries of different shape and size. The use of local region descriptor helps to cope with speckle noise that varies the contrast of the object's boundary. To handle multiple structure segmentation, an additional constraint in multiple level set framework is employed to prevent merging and overlapping between the neighboring contours in the shared boundaries of separate regions.

CHAPTER 3: MATERIALS AND METHODS

This chapter presents active contour based segmentation algorithms designed to address challenging problems available in the knee cartilage and meniscus ultrasound images. A summary on the ultrasound image acquisition protocols in order to obtain the knee cartilage and meniscus images is provided. In addition, the normal distance as a technique for computing the cartilage thickness in the ultrasound images is presented.

In Section 3.1, the knee cartilage boundary segmentation using the locally statistical level set method (LSLSM) and thickness computation using the normal distance method in the 2-D ultrasound images are presented. A summary of the methodologies on how to obtain short-axis views of the knee cartilage in the 2-D ultrasound images is given in Section 3.1.1. LSLSM applied in locating the cartilage boundary in a noisy and bias-corrupted image is described. The energy functional of LSLSM derived from Gaussian distributions of local image intensity and multiplicative noise model that consists of an image partition and an intensity bias estimation is explained in Section 3.1.2. To suppress the overlapped intensity distribution in the image, image intensities are defined within a neighbourhood at a certain scale. The local intensities are estimated by the spatially varying means and variances of the Gaussian distributions. To accomplish the joint segmentation and bias field estimation, the means are estimated by the product of the bias field and the piecewise constants. The energy functional to be minimized is expressed in the equivalent form of the convolution operation. The minimization process of the energy functional that iterates between the estimation of the variables and the evolution of the contour is described. Meanwhile, the minimization of the energy functional and the derivation of its variables from the equivalent expression of the energy functional are given. These variables are also expressed in the form of the convolution operation. In Section 3.1.3, the normal distance adopted as a technique for computing the cartilage thickness in the 2-D ultrasound images is explained. The cartilage thickness is automatically computed by averaging the normal distance along on the 2-D segmented cartilage area. The true thickness between the two interfaces of the cartilage is computed by estimating the length of normal vectors between its upper and lower boundaries. Finally, the section is concluded by providing the summary on the knee cartilage segmentation and thickness computation methods for the 2-D ultrasound images.

In Section 3.2, a multiple active contours framework or called as multiple LREK active contours (MLREK) for the meniscus ultrasound image segmentation is presented. In Section 3.2.1, the methodology to obtain ultrasound images of the meniscus in the knee joint is described. In Section 3.2.2, an active contour with adaptive-scale kernels to direct the evolving contour to reach the boundary concavity is described. The local image intensity within the kernels distributed on the contour front is employed. The kernels along the contour front expand gradually to reach the intended boundary within the image domain. To prevent the contour being trapped in a homogeneous region, the kernel is defined one at a time at the contour point and its scale is adaptable during the evolution process. During the segmentation process, the scale of the kernel varies for each contour point and depends on the distance of the contour point to the suspected boundary. The estimation of the scale is influenced by the local image intensity on the zero level of the contour. Next, the multiple level set formulation is provided to allow simultaneous multiple structure segmentation without merging and overlapping between neighbouring contours in dealing with unique challenges in the meniscus ultrasound images. The overall evolution process of MLREK is finally explained. Finally, the section is concluded by summarizing the meniscus ultrasound image segmentation method.

In Section 3.3, both qualitative and quantitative segmentation assessments using Cohen's κ statistics and two validation metrics of DSC and HD are explained, respectively.

The Cohen's κ statistics is used to express an inter-observer agreement for the segmentation quality of the cartilage area observed by two experts. While DSC metric indicates the area similarity between two comparing contours, HD metric tells the shape difference between the contour pair.

3.1 Cartilage Segmentation and Thickness Computation

In this section, the methodology in order to obtain the knee cartilage of the ultrasound images and the demographic information on the subject involved in this research are explained and detailed below. The locally statistical level set method applied to the cartilage boundary segmentation is described. The normal distance used to estimate the cartilage thickness based on the segmented images is then described.

3.1.1 Cartilage Ultrasound Image Acquisition

An ultrasound image acquisition protocol to capture the cartilage of the knee joint is described in this subsection. The Toshiba Aplio MX ultrasound machine is utilized with a 2-D linear array, 8-12 MHz multifrequency transducer (PLT-805AT). In order to obtain short-axis views of the femoral condylar cartilage on the trochlear notch, the subject were scanned in vivo in the supine position with the knee joint fully flexed (120°). The transducer was put transversely to the knee joint and perpendicular to the bone surface, just above the superior margin of the patella (Kazam et al., 2011; Naredo et al., 2009). Ten subjects (male, age range: 23-27 years, mean age: 24.75 ± 2.18) were recruited. The written consent was obtained prior to the ultrasound scanning. Four different scans of the cartilage were obtained from both left and right knee joints with repositioning of the ultrasound probe between acquisitions. The images were stored in DICOM format at a resolution of 0.1316×0.1316 mm. The musculoskeletal sonography was performed by a professional sonographer. The study received ethics approval from the University of

Malaya Medical Ethics Committee (MECID No. 20147-396) as attached in Appendix A.

3.1.2 Locally Statistical Level Set Method

The energy functional of LSLSM derived from Gaussian distributions of local image intensity and multiplicative noise model is explained in Section 3.1.2.1. It is composed of an image partition and an intensity bias estimation. The energy functional to be minimized is expressed in its equivalent form of convolution operation. Meanwhile, the minimization of the energy functional and the derivation of the variables from the equivalent expression of the energy functional are given in Section 3.1.2.2. The minimization problem is solved by iterating between two main tasks: the first task is concerned with the evolution of the level set function and the second task is dealt with the estimation of the variables. The variables are estimated in the energy minimization with respect to each variable. Using calculus of variations, the main energy functional is minimized, resulting in the gradient flow equation for the evolution of the level set function.

3.1.2.1 Energy Functional

The two-phase case of SVMLS or referred as the locally statistical level set method (LSLSM) is considered to address individual structure segmentation and bias field estimation in the knee cartilage ultrasound images. The energy functional of LSLSM is derived based on Gaussian distributions of local image intensity and multiplicative noise model. Intensity inhomogeneity associated with a component of an observed image I is often modelled as the following multiplicative noise model

$$I = bJ + \eta, \tag{3.1}$$

where J is the true image to be restored, b is an unknown bias field that approximates the intensity bias and η is refereed as the additive noise.

The true image, J is assumed as a piecewise constant. The bias field, b is to vary slowly. The additive noise, η is under the assumption of the Gaussian distribution with zero-mean. The distribution of image intensities I are approximated by Gaussian distributions with spatially varying means μ_i and variances σ_i^2. The intensity distribution in each local region is attributed to a Gaussian model. The intensity corresponding to each neighbourhood is given by

$$p(I(\mathbf{x})|\mu_i, \sigma_i) = \frac{1}{\sqrt{2\pi\sigma_i^2}} \exp\left(-\frac{|I(\mathbf{x}) - \mu_i|^2}{2\sigma_i^2}\right), \tag{3.2}$$

To accomplish the joint segmentation and bias field estimation, the means of the Gaussian distributions as the centres of the clusters μ_i are approximated by multiplication of the bias field $b(\mathbf{y})$ and the image signal within the window J estimated by a piecewise constant c_i for $i = 1, \ldots, N$, where N is the number of regions.

$$p(I(\mathbf{x})|b, c_i, \sigma_i) = \frac{1}{\sqrt{2\pi\sigma_i^2}} \exp\left(-\frac{|I(\mathbf{x}) - b(\mathbf{y})c_i(\mathbf{y})|^2}{2\sigma_i^2}\right). \tag{3.3}$$

The energy functions e_i is defined by

$$e_i(\mathbf{x}) = \int_\Omega -\log(p(I(\mathbf{x})|b, c_i, \sigma_i))d\mathbf{y}, \tag{3.4}$$

By substituting the equation (3.3) to the equation (3.4), the energy functions e_i become

$$e_i(\mathbf{x}) = \int_\Omega \frac{|I(\mathbf{x}) - b(\mathbf{y})c_i|^2}{2\sigma_i^2} + \frac{\log(2\pi\sigma_i^2)}{2} d\mathbf{y}, \tag{3.5}$$

In the attempt of reducing the overlapped intensity distribution in the image, image intensity is defined within a neighbourhood at a certain scale to form disjoint clusters.

$$e_i(\mathbf{x}) = \int_\Omega K(\mathbf{y}-\mathbf{x})\left(\frac{|I(\mathbf{x}) - b(\mathbf{y})c_i|^2}{2\sigma_i^2} + \frac{\log(2\pi\sigma_i^2)}{2}\right)d\mathbf{y}, \tag{3.6}$$

The energy functions e_i in the equation (3.6) is computed using the equivalent expression as follows

$$e_i(\mathbf{x}) = \frac{1}{2\sigma_i^2}\left(I^2\mathbf{1}_K - 2c_i I(b*K) + c_i^2(b^2*K)\right) + \frac{1}{2}\log(2\pi\sigma_i^2)\mathbf{1}_K, \tag{3.7}$$

where $*$ denotes convolution operator and $\mathbf{1}_K$ is defined as $\int K(\mathbf{y}-\mathbf{x})d\mathbf{y}$.

A uniform kernel function K is defined by

$$K(\mathbf{z}) = \begin{cases} a & \text{for } |\mathbf{z}| \leq \rho, \\ 0 & \text{for } |\mathbf{z}| > \rho, \end{cases} \tag{3.8}$$

where a is a positive constant such that $\int K(\mathbf{z}) = 1$. Only image intensities $I(\mathbf{x})$ in a neighborhood of $\mathbf{y}$ are effectively involved in the energy functions e_i in the equation (3.7). The scale of the kernel function K controls this neighborhood size. The choice of the small scale for the neighborhood enables to handle intensity inhomogeneity since the image intensities are only involved in a local neighbourhood centered at the point $\mathbf{y}$.

The energy functions, e_i that consist of an image partition and a bias field estimation are combined with membership function $M_i(\phi(\mathbf{x}))$ to be incorporated into the level set formulation. Therefore, the total energy function is defined by

$$E(\phi) = \nu\int_\Omega |\nabla H_\epsilon(\phi(\mathbf{x}))|d\mathbf{x} + \int_\Omega \sum_{i=1}^{2} e_i(\mathbf{x})M_i(\phi(\mathbf{x}))d\mathbf{x}, \tag{3.9}$$

with the first term being the regularization term to compute the arc length of the zero level set where its relative strength is controlled by the parameter ν. The variables c_i, b, and σ_i will be jointly estimated through minimization of the energy functional E.

In the two-phase case ($N = 2$), each region is represented by the membership functions $M_1(\phi) = H_\epsilon(\phi)$ and $M_2(\phi) = 1 - H_\epsilon(\phi)$, where the Heaviside function, H and the Dirac delta function, δ are computed by the equations (2.8) and (2.9), respectively.

3.1.2.2 Minimization of the Energy Functional

Via minimization of the energy functional, image segmentation and estimation of the bias field are performed together by estimating the membership functions $M_i(\phi)$, the restored bias field b, and the piecewise constants approximating the image intensity in each region c_i for $i = 1, 2$. The minimization process of the energy functional iterates between the estimation of the variables and the evolution of the level set function. The variables derived from the equivalent expression of the energy function are expressed in the form of the convolution operation. The level set function ϕ and the restored bias field b are the results of the image segmentation and the intensity bias estimation, respectively.

In the iterative process, the energy minimization with respect to each variable ϕ, c_i, b, and σ_i is obtained. The minimization problem is solved by iterating between two steps. In step one, the level set function is fixed, or equivalently the contour C, and then all these variables are estimated. In step two, the variables c_i, b, and σ_i for $i = 1, 2$ are fixed, and then the level set function is evolved, so that the energy functional E is minimized.

In step one, the variables c_i, b and σ_i are estimated. Keeping ϕ fixed, the first variation of E is taken with respect to the variables, and then equate the resulting expressions to zero, then solve the variables. It is easy to express these optimal variables c_i, b, and σ_i

that minimize E by

$$c_i(\mathbf{x}) = \frac{\int_\Omega (b * K) I M_i(\phi) d\mathbf{y}}{\int_\Omega (b^2 * K) M_i(\phi) d\mathbf{y}}, \tag{3.10}$$

$$b(\mathbf{y}) = \frac{\sum_{i=1}^{2} \frac{c_i}{\sigma_i^2} (I M_i(\phi) * K)}{\sum_{i=1}^{2} \frac{c_i^2}{\sigma_i^2} (M_i(\phi) * K)}, \tag{3.11}$$

$$\sigma_i^2 = \frac{\int_\Omega \left(I^2 \mathbf{1}_K - 2c_i I (b * K) + c_i^2 (b^2 * K) \right) M_i(\phi) d\mathbf{x}}{\int_\Omega (M_i(\phi) * K)\, d\mathbf{x}}. \tag{3.12}$$

In step two, assuming that all parameters are known, the level set function ϕ is evolved, hence the contour C, so that it minimizes the energy functional. Using the standard gradient descent method, the minimization of $E(\phi, c_i, b, \sigma_i)$ with respect to ϕ for fixed c_i, b, and σ_i is obtained. It is achieved by computing the gradient flow equation $\frac{\partial \phi}{\partial t} = -\frac{\partial E}{\partial \phi}$ where $\frac{\partial E}{\partial \phi}$ is the Gâteaux derivative of E. The gradient flow equation corresponding to the energy functional in the equation (3.9) has been derived in Appendix B.

$$\frac{\partial \phi}{\partial t} = \delta_\epsilon(\phi) \left[\nu \mathrm{div} \left(\frac{\nabla \phi}{|\nabla \phi|} \right) - e_1 + e_2 \right]. \tag{3.13}$$

To keep the level set evolution stable, after each iteration of the equation (3.13), the level set function is diffused by the following formulation (K. Zhang, Zhang, Song, & Zhang, 2013):

$$\phi^{n+1} = \phi^n + \Delta t \cdot \Delta \phi^n, \tag{3.14}$$

where ϕ^n is the level set function obtained from the n-th iteration of the equation (3.13) and Δt is the diffusion strength where Δ denotes the Laplacian operator.

3.1.3 Normal Distance

The normal distance (Heuer et al., 2001) is adapted as a technique for estimating the cartilage thickness in the short axis knee cartilage of the 2-D ultrasound images. While the thickness computation in (Fripp et al., 2010; Tang et al., 2006; Solloway et al., 1993) was performed in the 3-D cartilage surface, in this work, it is performed in the 2-D cartilage segmented area. The normal distance is used to compute the true normal thickness of the cartilage from one boundary to another in the segmented images. The thickness computation is performed by evenly spacing m points along the boundary, then taking the normal vector from the boundary points (x_i, y_i), and the perpendicular line is created from (x_i, y_i) to the intersection points of the upper or lower boundary of the cartilage. The distance between two points from the normal vector of the upper (or lower) boundary to the intersection of the line with the lower (or upper) boundary is utilized to compute the cartilage thickness t_i for each point, respectively. The average thickness of the cartilage $\bar{t}$ is taken from the mean of the thicknesses at all m boundary points.

3.1.4 Summary

The cartilage segmentation and thickness computation methods for the 2-D ultrasound images have been presented. LSLSM is applied in segmenting the cartilage boundary from the surrounding tissues that is not sufficiently distinct and hampered by spatial intensity variation caused by speckle and intensity inhomogeneity. The energy functional of LSLSM derived from the Gaussian distributions of local image intensity and multiplicative noise model is suitable to cope with a noisy and bias-corrupted image and thus distinguish different tissues between the cartilage interfaces. Therefore, the thickness between the cartilage interfaces can be measured based on the segmented images.

The energy functional of LSLSM represents an image partition and a bias field estimation. The image intensity is defined within a neighbourhood at a certain scale. It is approximated by the means and variances of the Gaussian distributions. The means are approximated by multiplication of the bias field and the piecewise constants. The segmentation and estimation of the bias field are performed together by estimating the membership functions, the variances, the restored bias field, and the piecewise constants. The results of the image partition and the bias field estimation are given by the level set function and the restored bias field.

The minimization of the energy functional and the derivation of the variables from the equivalent expression of the energy functional are given. An equivalent expression in the form of convolution operation is used to compute the energy functional and its variables. The minimization of the energy functional with respect to the level set function, the piecewise constants, the bias field, and the variances is performed in the iterative process. The minimization problem is solved by iterating between two steps. In step one, the piecewise constants, the bias field, and the variances are estimated. By minimizing the energy functional with respect to each variable, these variables are updated during the level set evolution. In step two, assuming that these variables are known and fixed, the minimization of the energy functional with respect to the level set function is obtained. The level set function is evolved so that the energy functional is minimized.

The normal distance as a technique for computing the cartilage thickness in the 2-D ultrasound images has been described. The cartilage thickness is measured by averaging the normal distances along the segmented cartilage area. The thickness computation is performed by taking the normal vector from the cartilage boundary and creating the perpendicular line from upper (or lower) boundary to the intersection points in the lower (or upper) boundary, respectively. The thickness is treated as the distance between two points from the normal vector of the upper (or lower) boundary to the intersection of the line in the lower (or upper) boundary for all boundary points, respectively.

3.2 Meniscus Ultrasound Image Segmentation

In this section, the methodology on how to obtain the knee meniscus of the ultrasound images and demographic information on the subject involved in this research are explained below. A segmentation framework for use in ultrasound imaging, which utilizes multiple active contours to simultaneously segment separate structures in an meniscus ultrasound image is presented.

3.2.1 Meniscus Ultrasound Image Acquisition

An ultrasound image acquisition protocol to capture the meniscus in the knee joint is described in this subsection. The Philips ClearVue 550 ultrasound system is utilized with a 2-D, 12 MHz (L12-4) broadband linear array transducer. The high frequency probe is desirable to observe superficial periarticular and intraarticular structures (Naredo et al., 2005). The medial side of the anterior view of the knee joint was scanned in vivo to capture the medial meniscus. The subject laid down in the supine position with the knee flexed 90°. Nineteen subjects (15 males and 4 females, age range: 18-55 years, and mean age: 31.20 ± 14.41) were recruited with an informed consent. A professional sonographer performed the ultrasound image acquisition. The study received ethics approval from the University of Malaya Medical Ethics Committee (MECID No. 20147-396) as attached in Appendix A.

3.2.2 Multiple LREK Active Contours

The multiple LREK active contours (MLREK) for segmentation of the meniscus in the ultrasound image are presented. In Section 3.2.2.1, an active contour with the variable-scale kernel to drive the contour to reach the boundary concavity is described. The scalable local regional information defined as a weighted mean intensity within scalable kernels distributed on the propagating contour is explained. A strategy to adapt the scale of the kernel to avoid the contour being trapped locally in a homogeneous region is explained. In Section 3.2.2.2, a framework for multiple active contours to address multiple structure problems is described. The multiple level set formulation with additional constraint is provided to allow simultaneous multiple region segmentation. It includes a strategy to prevent merging and overlapping between neighboring contours. Finally, the overall evolution process of this multiple active contours framework with the variable-scale kernel is explained in Section 3.2.2.3. After setting a number of parameters, the evolution process starts with estimation of the kernel size for each contour point. Then, the contour motion, its smoothness, and other contours motion are enforced by each of their corresponding terms. The entire process is repeated for another iteration. It will stop when the contours arrive at the boundary or once the iteration numbers have reached its maximum number.

3.2.2.1 Scalable Local Regional Information

A scalable local regional (SLR) information is defined as an image's weighted intensity mean within the scalable kernel. The SLR energy function e_i^{SLR} is defined by

$$e_i^{\mathrm{SLR}}(\mathbf{x}) = \int_{\Omega} K(\|\mathbf{y} - \mathbf{x}\|)\delta_{\epsilon}(\phi(\mathbf{y})) \times |I(\mathbf{x}) - \mu_i(\mathbf{y})|^2 d\mathbf{y}. \tag{3.15}$$

The local intensity region is masked using the kernel function. The uniform kernel, $K_u(d) = a$ is chosen where a is a positive constant. $d = \|\mathbf{x} - \mathbf{y}\|$ is L_2-norm distance between the contour points $\mathbf{x}$ and other points $\mathbf{y}$ within the kernel support. It takes into account image intensity within the distance, d from the contour. It does not consider spatial intensity variation outside d. Each kernel is divided by the contour line into two regions to sample intensity averages of the inner and outer regions within the kernel μ_i for

$i = 1, 2$, given by

$$\mu_i(\mathbf{y}) = \frac{\int_\Omega K(\|\mathbf{y} - \mathbf{x}\|) M_i(\phi(\mathbf{x})) I(\mathbf{x}) d\mathbf{x}}{\int_\Omega K(\|\mathbf{y} - \mathbf{x}\|) M_i(\phi(\mathbf{x})) d\mathbf{x}}. \tag{3.16}$$

A strategy to avoid the contour from being confined locally in a homogeneous region is explained. The scale of each kernel d_q, $q = 1, 2, \ldots, m$ is defined at the points along the contour line q, where m denotes the pixel numbers. For each iteration, the number of the kernels relies on the pixel numbers on the contour line. Initially, the scale of the kernel is set to $d_q = d_{\text{initial}}$ pixels. The scale adaptation process is enabled by gradually adding Δd pixels to d for each contour point. It depends on the comparison between the absolute difference of an intensity threshold, thres and μ_1 or μ_2. This comparison tells whether the kernel lies entirely on the homogeneous region or has arrived at the boundary. thres = $[L \times \tau]$ represents a small intensity value of the input image where $\tau \subseteq [0, 1]$ and $L = 255$ for the 8-bit grayscale images. The value of thres should be set close to zero to indicate the difference between μ_1 and μ_2. If the difference is less than thres where μ_1 is about the same as μ_2, it implies that the kernel is still in the homogeneous area. In this case, the scale of the kernels will expand gradually. This process is repeated iteratively until the kernel has arrived at the nearest boundary. Once it crosses the boundary, there is a significant difference between μ_1 and μ_2 in which the difference is larger than the threshold. It means that the kernel has found its optimal scale, thus the SLR energy function e_i^{SLR} will determine the motion of the contour line to reach the boundary.

Using the local version of the Chan-Vese energy (T. F. Chan & Vese, 2001), the SLR energy function e_i^{SLR} in the equation (3.15) reaches its optimum point when the image pixels within the kernel at each contour point $I(\mathbf{x})$ is optimally estimated by the local intensity averages μ_i. It acts as a force to inflate or deflate the contour locally. It is influenced by the difference between $I(\mathbf{x})$ and μ_1 or μ_2. If the value of $I(\mathbf{x})$ is closer to μ_1 than μ_2, the negative sign of e_i^{SLR} will grow the contour. If $I(\mathbf{x})$ is about the same value as μ_2 and far different from μ_1, the positive sign of e_i^{SLR} will shrink the contour. When the value of $I(\mathbf{x})$ is about the same either with μ_1 or μ_2, e_i^{SLR} will not produce any motion force and the contour will finally converge at the intended boundary.

The total energy function expressed using the level set formulation is written in the equation (3.17). The first term of the equation (3.17) is the contour's length regulation term that serves to smoothen the contour. In the second term of the equation (3.17), the function e_i^{SLR} is combined with membership function $M_i(\phi)$ for $i = 1, 2$.

$$E(\phi) = \nu \int_{\Omega} |\nabla H_{\epsilon}(\phi(\mathbf{x}))| d\mathbf{x} + \int_{\Omega} \sum_{i=1}^{2} e_i(\mathbf{x}) M_i(\phi(\mathbf{x})) d\mathbf{x}, \tag{3.17}$$

where ν is a weighing parameter of the contour's smoothness.

Using the standard gradient descent method, the energy functional $E(\phi)$ in the equation (3.17) is minimized with respect to the level set function ϕ by solving the gradient flow equation $\frac{\partial \phi}{\partial t} = -\frac{\partial E}{\partial \phi}$. $\frac{\partial E}{\partial \phi}$ is derived using the Gâteaux derivative where the derivation is given in more detail in Appendix C. It is performed by substituting ϕ with $\phi + \xi\psi$, where ψ denotes a tiny change perpendicular to ϕ weighted with a small number ξ. The corresponding gradient flow equation is written in the equation (3.18). It consists of the contour's smoothness term that calculates the arc length of the zero level set and the SLR force that drives the contour.

$$\frac{\partial \phi}{\partial t} = \delta_{\epsilon}(\phi) \left[\nu \mathrm{div} \left(\frac{\nabla \phi}{|\nabla \phi|} \right) - e_1 + e_2 \right], \tag{3.18}$$

where $\mathrm{div}(\cdot)$ denotes the divergence.

3.2.2.2 Multiple Level Set Formulation

The previous level set formulation in Section 3.2.2.1 is for the two-phase case ($N = 2$) using a level set function. To allow simultaneous multiple region segmentation, the energy functional is re-formulated into a n-active contours framework. To deal with multiple object regions ($N > 2$), multiple level set functions $\phi_1, \ldots, \phi_n$ are employed. Multiple contours are embedded in the n-level set functions $(\phi_j)_{j=1}^n$ where each object's region is represented by one level set function.

The previous single level set energy function in the equation (3.17) is converted into the following multiple level sets formulation, considering the required number of contours, n is known.

$$E(\phi_1, \ldots, \phi_n) = \nu \int_\Omega \sum_{j=1}^{n} |\nabla H_\epsilon(\phi_j(\mathbf{x}))| d\mathbf{x} + \int_\Omega \sum_{i=1}^{2} \sum_{j=1}^{n} e_i(\mathbf{x}) M_i(\phi_j(\mathbf{x})) d\mathbf{x}. \tag{3.19}$$

To deal with segmentation of multiple structure with shared boundaries, an additional constraint is needed to avoid the zero level contour overlaps with its neighbouring contour. The strategy in (Zhao et al., 1996) is modified to be utilized with the scalable local regional information. Therefore, the additional constraint is placed as the third term in the total energy function. The multiple level set formulation of MLREK's energy is written using a vector value notation $\Phi = (\phi_1, \ldots, \phi_n)$ as follows

$$E(\Phi) = \nu \int_\Omega |\nabla H_\epsilon(\Phi(\mathbf{x}))| d\mathbf{x} + \int_\Omega \sum_{i=1}^{2} e_i(\mathbf{x}) M_i(\Phi(\mathbf{x})) d\mathbf{x} - \int_\Omega H_\epsilon(\Phi_j(\mathbf{x})) H_\epsilon(\Phi_k(\mathbf{x})) d\mathbf{x}. \tag{3.20}$$

Minimization of the MLREK's energy function in the equation (3.20) with respect to Φ resulted in the gradient equation flow in equation (3.21) for $\phi_j; j = 1, \ldots, n$. The corresponding gradient flow equation evolving every level set function ϕ_j is given in the equation (3.22).

$$\frac{\partial \phi_j}{\partial t} = \nu\delta_\epsilon(\phi_j)\mathrm{div}\left(\frac{\nabla\phi_j}{|\nabla\phi_j|}\right) - \sum_{i=1}^{2}\frac{\partial M_i(\phi_j)}{\partial \phi_j}e_i + \delta_\epsilon(\phi_j)\left(\sum_{k\neq j}^{n} H_\epsilon(\phi_k)\right), \tag{3.21}$$

$$\begin{aligned}
\frac{\partial \phi_1}{\partial t} &= \delta_\epsilon(\phi_1)\left(\nu\mathrm{div}\left(\frac{\nabla\phi_1}{|\nabla\phi_1|}\right) - e_1 + e_2 + \sum_{k\neq 1}^{n} H_\epsilon(\phi_k)\right),\\
&\vdots\\
\frac{\partial \phi_n}{\partial t} &= \delta_\epsilon(\phi_n)\left(\nu\mathrm{div}\left(\frac{\nabla\phi_n}{|\nabla\phi_n|}\right) - e_1 + e_2 + \sum_{k\neq j}^{n} H_\epsilon(\phi_k)\right).
\end{aligned} \tag{3.22}$$

In equation (3.21), the first term is the contour smoothing force, the second term is the SLR force, and the third term is the area term of the regularized Heaviside functions. The third term is used to prevent the neighbouring contours from creating overlapping regions. When updating the contour ϕ_j, other contours $(\phi_k)_{k\neq j}^{n}$ are represented by their area terms $\sum_{k\neq j}^{n} H_\epsilon(\phi_k(\mathbf{y}))$ where $H_\epsilon(\phi)$ is computed according to the equation (2.8). This strategy thus avoids the evolving contours from surpassing each other in the shared boundaries of disjointed regions.

3.2.2.3 Evolution Process

The evolution process of MLREK begins by setting the number of iterations, l, multiple positions of initial contours C_0, the initial scale of the kernel, d_{initial}, the additional scale of the kernel, Δd, and the threshold value, thres. Each contour C_j is embedded in the zero level set function ϕ_j; $j = 1, \ldots, n$ where n is the number of the contours. For $j = 1, \ldots, n$, the value of d_j, Δd_j, and thres$_j$ can be different and is not necessarily set to be similar for each function ϕ_j.

As the energy is minimized by an iterative process, the zero level of contours ϕ_j is updated at each time step $p = 1, \ldots, l$. For every contour point $q = 1, \ldots, m$, $d_q = d_{\text{initial}}$ is set. The means μ_i for $i = 1, 2$ are computed using the equation (3.16). Then, the condition $|\mu_1 - \mu_2| <$ thres is checked where $|.|$ denotes absolute value. If the condition is true, $d_q = d_q + \Delta d$ is set, μ_1 and μ_2 are proceeded to be updated, and the condition is returned to be checked. It will be repeated until the condition is not met, and then e_i^{SLR} proceeds to be computed. All of these processes are iteratively repeated for every kernel on the contour point. Then, the contour ϕ_j is navigated towards the boundary using the equation (3.15). Its smoothness is enforced by the second term of the equation (3.21). Meanwhile, other contours $(\phi_k)_{k\neq j}^n$ are described by their area terms $\sum_{k\neq j}^n H_\epsilon(\phi_k(\mathbf{y}))$. Another contour's evolution starts by re-initializing d_q to d_{initial} and repeating the whole process. Then, all contours are evolved by one iteration and will be reiterated until the contours converge to the boundary or a maximum number of iterations is reached. The entire evolution process is illustrated in Algorithm 1.

Algorithm 1 MLREK's evolution process

```
Set l, d_j, Δd_j, thres_j, and φ_j for j = 1, ..., n;
m is number of points in φ;
for p ← 1, l do                                  ▹ Loop until l iteration numbers
    for j ← 1, n do                              ▹ Loop for n contours
        for q ← 1, m do                          ▹ Loop for m contour points
            Set d_q = d_initial                  ▹ Set initial kernel's scale
            Compute μ_i according to (3.16)
            while |μ_1 − μ_2| < thres do
                Set d_q = d_q + Δd               ▹ Expand the kernel
                Update μ_1 and μ_2
            end while
            Compute e_i^SLR according to (3.15)
        end for
        Evolve φ_j according to (3.21)
    end for
end for
```

3.2.3 Summary

The meniscus ultrasound image segmentation method has been presented. An active contour that uses scalable local regional information on expandable kernels is utilized.

The local image information is defined as intensity values of the pixels on a set of scalable kernels distributed along the evolving contours. It is used to direct the contour's front towards the intended boundary within an image domain. The contour line divides each kernel into two regions that are inside and outside the contour to measure the intensity profiles at image pixels on both sides the contour. The use of the local region descriptor helps to cope with speckle noise that varies the contrast of the object's boundary. A strategy inside the variational level set method is used to adapt the scale of the kernels to successfully reach the concave parts. The variable scale kernel is designed to avoid being trapped in homogeneous regions during the segmentation process. The scale of these kernels varies for each contour point and is dependent on the distance of the contour point to the nearest boundary. These kernels expand gradually until a boundary is detected. The support of each kernel is defined one at a time in each contour point. The estimation of the kernel size is influenced by the local image intensity on the zero level of the contour.

The multiple active contours framework utilized the scalable local regional (SLR) information is presented to deal with the multiple structure problem in the meniscus ultrasound images. Multiple level set functions are used to embed the multiple contours where each level set function represents one object's region to be segmented. To prevent the multiple level set functions from merging and overlapping each other, an additional constraint placed as the third term in the energy functional is used to regulate the multiple contours. Hence, simultaneous segmentation of separate objects of the femoral condyle, the meniscus, and the tibial plateau can be performed all at once in a single image.

The optimal kernel scale is estimated based on the distance of the contour point to the nearest boundary. After the optimal scale for each contour point is obtained, the SLR force navigates the contour towards the object boundary. The smoothness of the contour is regulated by the contour's smoothing term. Meanwhile, other contours are described by their area terms. Another contour evolution starts by estimating the kernel size and repeating the entire process. Then, all contours are deformed gradually by one iteration. The contours will be iteratively evolved until arrive at the boundary when the intensity profile within the kernel is optimally approximated by their local means. The contour evolution will also be stopped when a maximum number of iterations has been reached.

3.3 Evaluation of Segmentation Accuracy

In order to evaluate the segmentation results, qualitative and quantitative segmentation assessments are performed using Cohen's κ statistics and two validation metrics of DSC and HD, respectively. Over all available data sets, the manual outlines as ground truth data were compared against the segmentation results obtained by the algorithms to be evaluated qualitatively and quantitatively.

3.3.1 Qualitative Assessment

The overall segmentation quality of the cartilage anatomical structure in ultrasound images are validated by two experts. The segmentation quality of the cartilage area was assessed by differentiating the boundaries between the soft tissue-cartilage interface and the cartilage-bone interface, which categorized as follows: Grade 1: excellent segmentation quality, with excellent differentiation of the boundaries between the two interfaces and no significant overlap segmentation areas. Grade 2: good segmentation quality, with good differentiation of the boundaries between the two interfaces and only small overlap segmentation areas. Grade 3: poor segmentation quality, with poor differentiation of the boundaries between the two interfaces and some overlap segmentation areas. Grade 4: bad segmentation quality, with bad differentiation of the boundaries between the two interfaces and large overlap segmentation areas.

Inter-observer agreement for the segmentation quality of the cartilage area obtained by

LSLSM is expressed as the Cohen's κ statistics (Cohen, 1960). The observed agreement, the chance agreement, and the κ statistics for agreement between two observers were calculated. The observed agreement is the number of occasions of complete agreement between observers divided by the total number of occasions. The chance agreement is the probability that the observers will provide the same response to an observation. The kappa coefficient is defined as the observed agreement, which is above and beyond that due to chance. Different ranges for kappa values characterise the degrees of agreement. A kappa value of less than 0 implies poor agreement (agreement worse than that of chance alone), 0.00 to 0.20 slight agreement (agreement equal to that of chance alone), 0.21 to 0.40 fair agreement, 0.41 to 0.60 moderate agreement, 0.61 to 0.80 substantial agreement and 0.81 to 1.00 almost perfect agreement (Landis & Koch, 1977).

3.3.2 Quantitative Assessment

In order to examine the segmentation performance of the active contour models for the knee cartilage and meniscus ultrasound image segmentation, the contours obtained from the presented active contour models are compared against those traced manually by an expert or called gold standard. The segmentation performance is quantified using two different metrics of DSC (Dice, 1945) and HD (Huttenlocher, Klanderman, & Rucklidge, 1993) to measure the area similarity and the shape difference, respectively. DSC metric is used to compare the similarity between the areas of the segmented contour (A) and of the reference contour (B). It measures the ratio between twice of the common region of both comparing contours and the sum of their individual regions, given by

$$DSC(A, B) = \frac{2|A \cap B|}{|A| + |B|}, \tag{3.23}$$

This metric indicates the relative locations and sizes of the compared contours. The value is bounded in [0, 1] and the value of 1 implies that the contour pair has the same location and size (or area).

HD metric is used to compare the shape difference rather than the area similarity of the contour pair. It computes the boundary mismatch between two comparing segmented boundaries. HD in equation (3.24) is defined as the largest of all the distances of each point in X that is nearest to any point in Y.

$$HD(X, Y) = \max\left(\max_{x \in X} \min_{y \in Y} \|x - y\|, \max_{y \in Y} \min_{x \in X} \|x - y\|\right), \tag{3.24}$$

where X and Y are two sets of points extracted from the segmented and reference boundaries of A and B, respectively. The small value of d_H implies a minimal shape difference between two comparing contours.

CHAPTER 4: RESULTS AND DISCUSSION

In this chapter, some results and their interpretations on the cartilage segmentation and thickness computation and on the meniscus segmentation in the 2-D ultrasound images are presented and organized into two sections. Some advantages and disadvantages of different active contour models when applied to the knee cartilage and meniscus ultrasound images are pointed out and discussed.

In Section 4.1, the results and discussion on the cartilage segmentation and thickness computation in the 2-D ultrasound images are provided. In Section 4.1.1, the segmentation performances and computational times of LSLSM and other level set methods in the attempt of segmenting a real knee cartilage ultrasound image are compared and discussed. The segmentation results of different level set methods are evaluated using validation metrics of DSC and HD. In Section 4.1.2, the segmentation performances of the three different level set methods when applied to a set of the knee cartilage ultrasound images are discussed. Both qualitative and quantitative evaluations are performed to compare the segmentation results obtained by the algorithms and performed manually by an expert. The cartilage thickness measurement on a set of the segmented images using the normal distance is evaluated in Section 4.1.3. The statistics and reproducibility of this ultrasound-based cartilage thickness measurement and the agreement between pairs of the measurements by the normal distance and the manual measurement are determined.

In Section 4.2, several results on the meniscus ultrasound image segmentation are discussed. In Section 4.2.1, the segmentation results, convergence properties, computational times of MLREK and other existing active contour methods in their attempt of segmenting the meniscus of the ultrasound image are compared and discussed. The segmentation performances and convergence rates of different active contour models are illustrated using DSC metric. In Section 4.2.2, the responses of varying several parameters in MLREK to the segmentation results are further studied and interpreted. Quantitative evaluation of the sensitivity of each parameter in MLREK to the segmentation accuracy is illustrated using both DSC and HD metrics. The effects of threshold value selection in response to the segmentation results as well as convergence properties are investigated. The ability of the presented multiple level set framework in avoiding merging and overlapping between the neighbouring contours is discussed. The accuracy improvement achieved by assigning different choices of scale parameters for each zero level contour in multiple region segmentation is discussed. In Section 4.2.3, the segmentation performance of MLREK when applied into a set of the meniscus ultrasound images is presented and discussed. The segmentation results are validated using quantitative evaluation metrics of DSC and HD. The reproducibility and agreement between DSC measures of the segmentation results of the femoral condyle, the meniscus, and the tibial plateau are determined and discussed. Finally, each section is concluded by the summary of the knee cartilage segmentation and thickness computation and the meniscus segmentation in the ultrasound images.

4.1 Cartilage Segmentation and Thickness Computation

4.1.1 Comparison with Other Level Set Methods

In this section, a comparison of different level set methods in their attempt of segmenting a real knee cartilage ultrasound image is provided. In this experiment, LSLSM was compared to the two methods without and with multiplicative component estimation, i.e., LGDF and WKVLS, respectively. A brief summary of the two segmentation methods is provided. Similar to LSLSM, LGDF also assumes spatially locally varying mean and variance of a Gaussian distribution. While WKVLS and LSLSM were essentially designed to simultaneously estimate the multiplicative bias field while segmenting the images, LGDF can only be used for segmentation since it does not estimate multiplicative component. However, WKVLS ignores the variance component that is taken into account in LSLSM, which helps to distinguish different tissues more accurately.

All the methods were implemented in MATLAB R2014a in an Intel (R) Xeon (R), 2.00 GHz, 32 GB RAM with the following parameter settings. Small kernel's radius $\rho = 5$ is chosen to provide more accurate boundary location. For grayscale images with intensity range $[0, 255]$, the constant ν was set to 0.001×255^2. It was chosen to be small when segmenting objects of any size. The time steps for level set evolution Δt_1 and for regularization Δt_2 were set as $\Delta t_1 = 0.01$ for LGDF, $\Delta t_1 = 0.1$ and $\Delta t_2 = 0.1$ for WKVLS, and $\Delta t_1 = 0.01$ and $\Delta t_2 = 0.01$ for LSLSM. Image size is 420×150 pixels.

(a) Initial contour

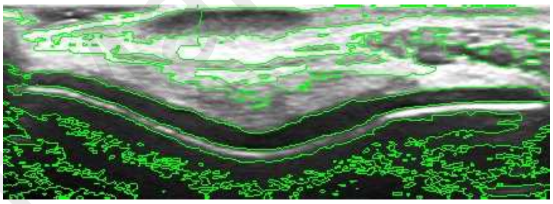

(b) Final contour of LGDF

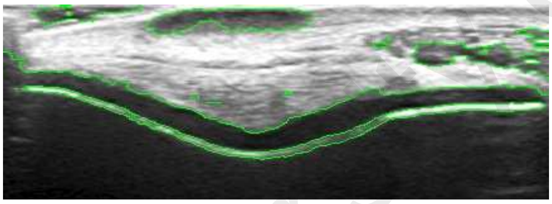

(c) Final contour of WKVLS

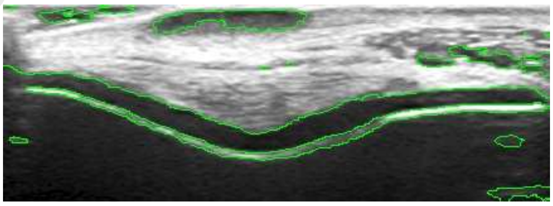

(d) Final contour of LSLSM

Figure 4.1: The segmentation results of three different level set methods in segmenting the knee cartilage of the ultrasound image. The red circle with 10 pixels radius represents the initial contour. The green lines represent the final contours.

Figure 4.1 illustrates the segmentation results of the three related level set methods that are applied to the cartilage boundary segmentation. Figure 4.1 depicts (a) the initial contour, the final contours of (b) LGDF, (c) WKVLS, and (d) LSLSM. The initial and the final segmentation contours are coloured in red and green, respectively. The initial contour is in circle shape with 10 pixels radius and placed just around the center of the images. These three segmentation algorithms are generally able to distinguish different tissues in the presence of noise and intensity inhomogeneity. This is due to the use of local image intensity defined in a local neighborhood that suppresses the overlapping intensity distribution. With the multiplicative component estimation, WKVLS and LSLSM are able to reduce the non-uniform textures and then locate the boundaries between different tissues correctly as seen in Figures 4.1(c) and (d). Without the multiplicative component estimation, LGDF produces an unstable segmentation result where misclassified contours inside the object and some unnecessary contours around the object appear in the final contours as shown in Figure 4.1(b). Both models yield satisfying segmentation results, while LSLSM that considers the variance component obtained a better result than WKVLS.

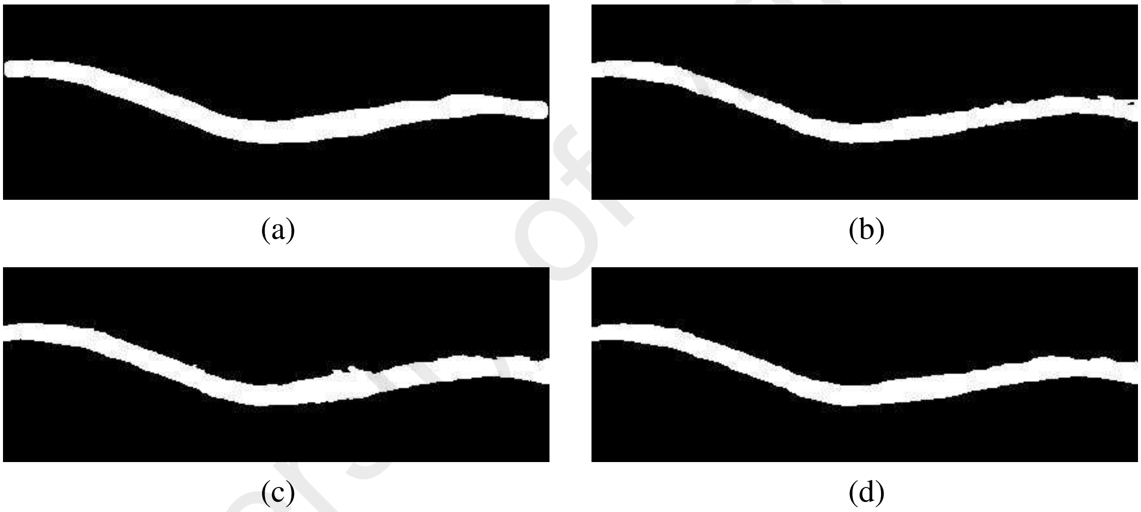

Figure 4.2: (a) Manual segmentation of the cartilage. Cartilage regions extracted from the segmented images by (b) LGDF, (c) WKVLS, and (d) LSLSM.

DSC and HD metrics were computed from the manual outline and the isolated cartilage region as depicted in Figure 4.2. The cartilage region was extracted from its surrounding tissues in the final contours using the connected-component labelling. This is to ensure that the validation metrics of DSC and HD are computed based on the cartilage region and not affected by segmentation of the surrounding tissues. DSC and HD measures for the segmentation outcomes of LGDF, WKVLS, and LSLSM in Figures 4.1(b), (c), and (d) are summarized in the first, second, and third rows of the matrices $\begin{bmatrix}0.9027\\0.9148\\0.9423\end{bmatrix}$ and

$\begin{bmatrix} 6.8557 \\ 7 \\ 6.3246 \end{bmatrix}$, respectively. We observed that the DSC value obtained by LSLSM is higher than the ones obtained by WKVLS and LGDF while HD value obtained by LSLSM is smaller than the ones obtained by WKVLS and LGDF. DSC and HD metrics confirm satisfying segmentation performance of LSLSM depicted in Figure 4.1. In addition, the total computational time for the contour evolution of LGDF, WKVLS, and LSLSM required for 500 iterations are 55, 14, and 13 seconds, respectively.

4.1.2 Cartilage Ultrasound Image Segmentation

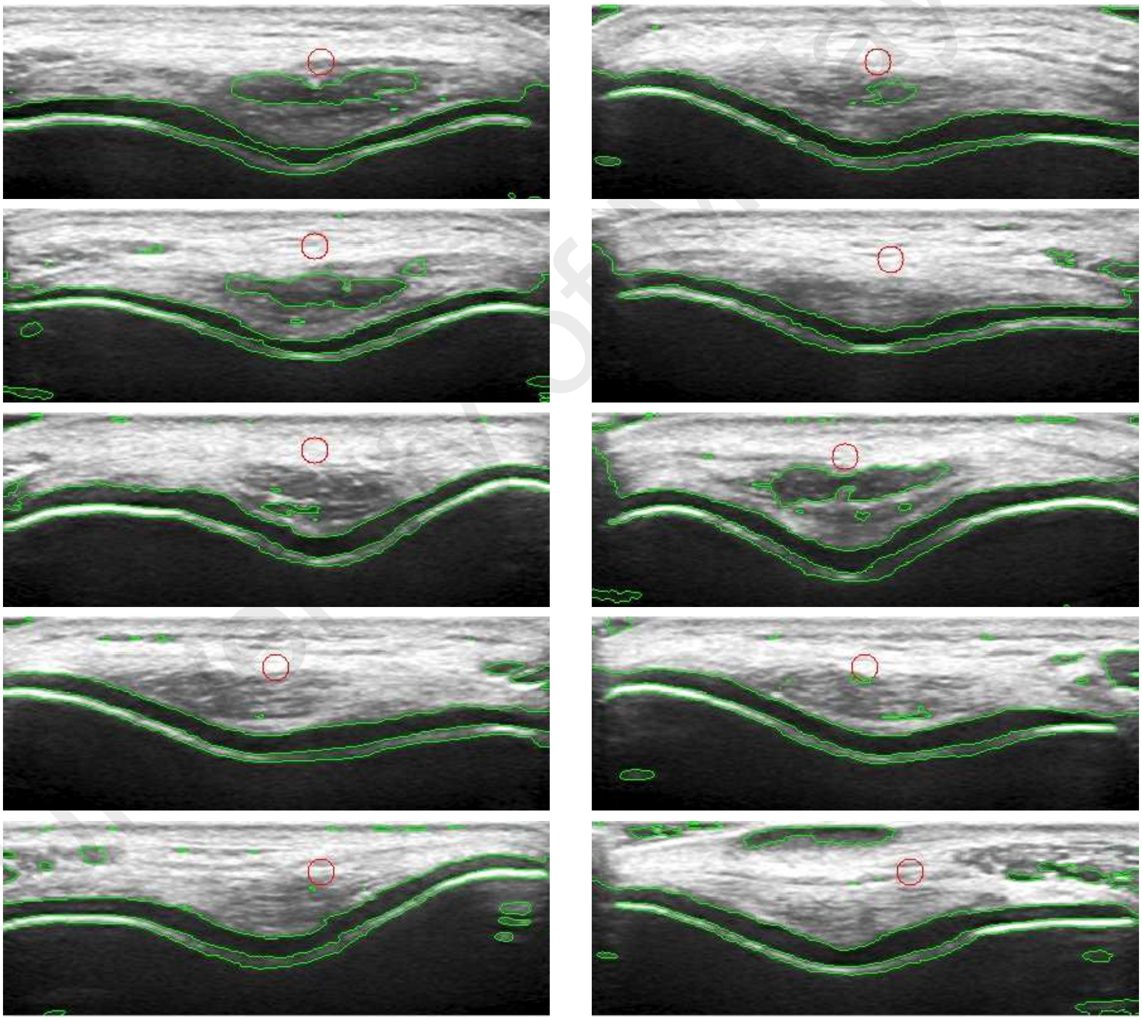

Figure 4.3: Left and right columns represent segmentation results obtained by LSLSM for the left and right knee cartilages of five subjects.

In this subsection, the three different level set methods were applied to segment a set of the knee cartilage of the ultrasound images. Figure 4.3 depicts a subset of 10 segmentation outcomes of the cartilages from total data sets of 80 images. The data sets consist of different scans of the cartilage acquired from ten subjects; both left and right knee joints were imaged four times each with repositioning of the ultrasound probe between acquisitions. The initial contour is depicted in red circle with 10 pixels radius and placed just around the center of the images. The green lines represent the final segmentation contours. The final contours were subsequently used to isolate the cartilage region from its surrounding tissues as illustrated in Figure 4.2(b). The connected-component labelling is used to remove other tissue regions in the binary image. The manual outlines as ground truth data were compared against its isolated cartilage region obtained by the algorithm to be evaluated qualitatively and quantitatively. An expert segmented the cartilage manually from each ultrasound image scan. The segmentation results of LGDF, WKVLS, and LSLSM were evaluated qualitatively and quantitatively over the total data sets of 80 images. While the qualitative assessment is performed using Cohen's κ statistics, the quantitative assessment is performed using validation metrics of DSC and HD.

The number of observed agreements is 67 images (83.75% of the observations), as grade 1 (excellent) in 39 images (48.75%), as grade 2 (good) in 21 images (26.25%), as grade 3 (poor) in 5 images (6.25%), as grade 4 (bad) in 2 images (2.5%). The number of agreement due to chance is 32.05 images. An overall segmentation quality for all 10 subjects rated by two experts indicates a substantial agreement with $\kappa = 0.73$.

Figures 4.4 and 4.5 illustrate a quantitative comparison of LGDF, WKVLS, and LSLSM validated using DSC and HD values over the total data sets of 80 images, respectively. Figure 4.4 shows the computed DSC values for 80 images fall in the range between 0.84 and 0.94, 0.29 and 0.95, and 0.82 and 0.95 for LGDF, WKVLS, and LSLSM, respectively. The higher value of DSC metric indicates that the two comparing contours have a good agreement in size and location, which correspond to more accurate segmentation

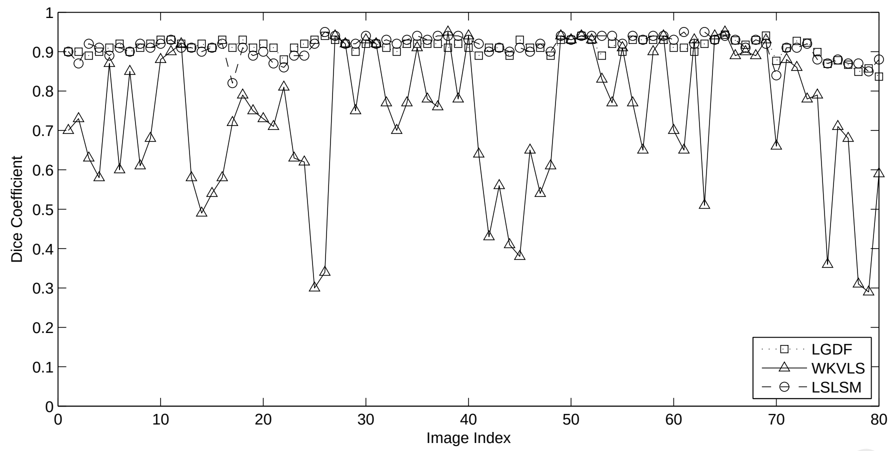

Figure 4.4: DSC measures over 80 images comprised of four repeated scans of the cartilage of the left and right knee joints obtained from ten subjects.

results. The computed HD values in Figure 4.5 are ranging from 4.47 to 8.83, 5.39 to 19.10, and 4.69 to 8.25 pixels for LGDF, WKVLS, and LSLSM, respectively. Smaller HD values correspond to the least difference in shape between the two comparing contours.

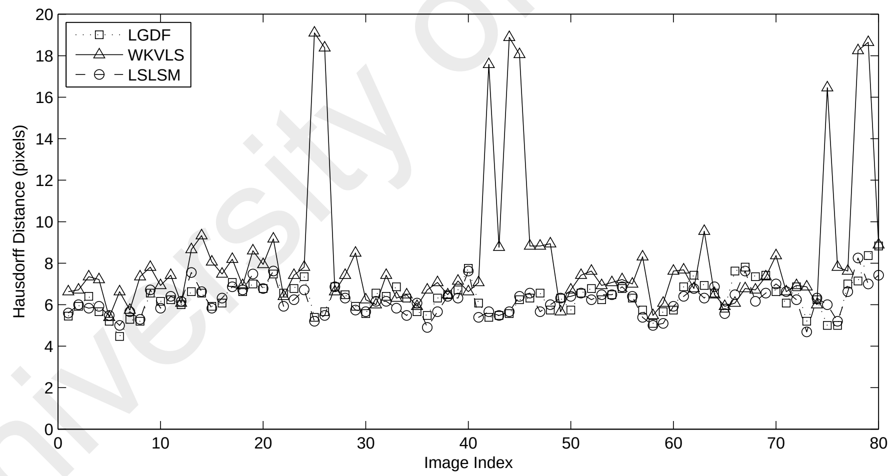

Figure 4.5: HD measures over 80 images comprised of four repeated scans of the cartilage of the left and right knee joints obtained from ten subjects.

The mean and standard deviation of DSC and HD values for all methods over the total data sets of 80 images are summarized in Table 4.1. It indicates that LSLSM obtained higher average value for DSC metric for all available data sets than LGDF and WKVLS. Meanwhile, the average value for HD metric obtained by LSLSM is smaller than obtained by LGDF and WKVLS. It implies that LSLSM provides a good area similarity and a minimally different contour shape, which illustrates the satisfactory segmentation outcomes for all available data sets.

Table 4.1: Statistics of the Evaluation Metrics

Methods	DSC	HD (pixels)
LGDF	0.90 ± 0.02	6.33 ± 0.62
WKVLS	0.73 ± 0.14	8.32 ± 2.17
LSLSM	0.91 ± 0.01	6.21 ± 0.59

The segmentation errors were mainly due to the overlapped intensity distribution between different tissues. The boundary between different tissues is not sufficiently distinct, particularly around the interfaces of soft tissue-cartilage and cartilage-bone. The variances of the Gaussian distributions that are taken into account in LGDF and LSLSM helps to distinguish the two interfaces more satisfactorily. Although WKVLS considers the multiplicative component, it does not take into account the variance component, thus tends to misclassify the two interfaces. In addition, the degree of inhomogeneity is varied between the scanned images. These may be the cause of the less satisfactory segmentation performance indicated by DSC values below 0.8 and HD values above 7 pixels in the graphs. The overall DSC and HD metrics shown in the graphs have illustrated the satisfactory segmentation outcomes of LSLSM for all available data sets.

4.1.3 Cartilage Thickness Computation

The cartilage thickness is computed based on the segmented images using the normal distance (Heuer et al., 2001). Images of cartilage acquired from the ten subjects are used; different scans of the cartilage of both left and right knee joints were imaged four times each as described in Section 3.1.1. The cartilage images were firstly segmented using LSLSM method described in Section 3.1.2. The final contours generated by the segmentation algorithm were subsequently used to isolate the cartilage from its surrounding tissues.

The connected-component labelling is used to remove surrounding tissue regions from the final contour results. Figure 4.2(a) illustrates an example of an isolated region of the cartilage extracted from the segmentation outcome. Using this isolated cartilage ensures the thickness measurements are performed in the cartilage region only. The cartilage thickness was calculated for each sample using the normal distance described in Section 3.1.3. The normal distance computes the true thickness of the cartilage by estimating the length of boundary normal vectors between the upper and lower boundaries of the cartilage (Tang et al., 2006; Solloway et al., 1993) as illustrated in Figure 4.2(d). The thickness measurements were made at every pixel on the upper and lower boundaries.

The obtained measurements of the cartilage thickness ranged from 1.35 mm to 2.72 mm, 1.36 mm to 2.45 mm, 1.33 mm to 2.17 mm, 1.68 mm to 2.39 mm, and 1.35 mm to 2.42 mm for the manual thickness measurement, the normal distance on the cartilage area segmented by the manual outline, LGDF, WKVLS, and LSLSM, respectively. It reflects the robustness of the segmentation algorithms to various cartilage thickness. The statistics such as mean, standard deviation, and the intraclass correlation coefficient (ICC) in Table 4.2 were computed to determine the accuracy and reproducibility of the cartilage thickness computation using the normal distance. ICC values were determined from the thickness measurements of the four repeated scans for all methods. Higher value of ICC indicates a good reproducibility between the measurement sets.

The cartilage thickness computed by the normal distance on the cartilage area segmented by (b) the manual outline, (c) LGDF, (d) WKVLS, and (e) LSLSM was compared to the results obtained by the manual measurement using Bland-Altman plot (Bland & Altman, 1999). The manual measurement is provided by drawing the perpendicular line between the hyper-echoic lines at the soft tissue-cartilage interface and at the cartilage-bone interface (Kazam et al., 2011), (Naredo et al., 2009). In each knee joint, three

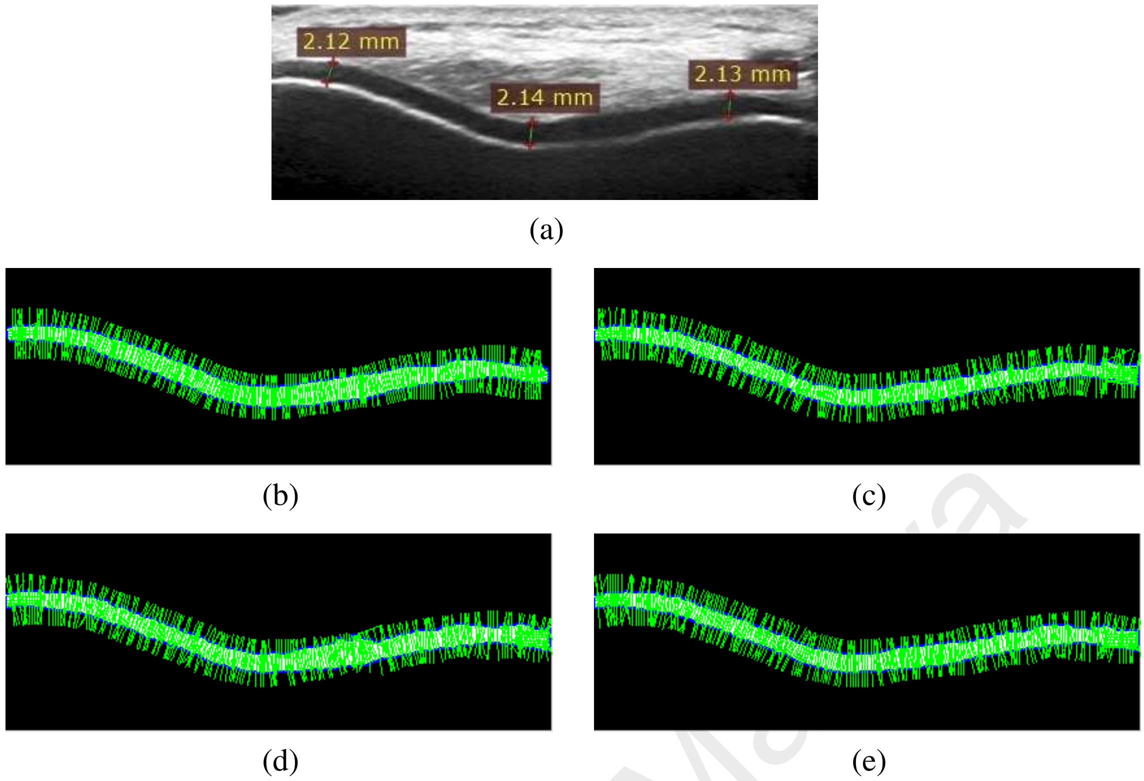

Figure 4.6: (a) Manual thickness measurement of the cartilage. Thickness computation of the cartilage using the normal distance on the cartilage area segmented by (b) the manual outline, (c) LGDF, (d) WKVLS, and (e) LSLSM.

separate measurements were performed at three locations, i.e., the trochlear notch, two-thirds lateral (two-thirds of the distance from the trochlear notch to the convexity of the lateral trochlea), and two-thirds medial (two-thirds of the distance from the trochlear notch to the convexity of the medial trochlea) as illustrated in Figure 4.6(a). The average value is taken from the manual measurement at the three locations.

Table 4.2: Cartilage Thickness Measurement Results

Methods	Image	Mean	ICC
Manual Measurement	Original Image	2.02 ± 0.13	0.95
Normal Distance	Manual Outline	2.00 ± 0.13	0.94
	LGDF	1.83 ± 0.10	0.91
	WKVLS	2.06 ± 0.09	0.85
	LSLSM	1.97 ± 0.11	0.92

Figures 4.7, 4.8, 4.9, and 4.10 illustrate Bland-Altman plots for the thickness measurements obtained manually and by the normal distance on the cartilage area segmented

by the manual outline, LGDF, WKVLS, and LSLSM, respectively. Bland-Altman plots illustrate a good agreement of the cartilage thickness obtained by two measurement methods. The mean differences for all pairs of the thickness measurements were 0.02 ± 0.17, 0.19 ± 0.20, -0.04 ± 0.22, and 0.05 ± 0.18 mm for the manual outline, LGDF, WKVLS, and LSLSM, respectively. Small mean difference indicates no significant bias for both methods. It can also be observed that nearly all differences between measurements by the two methods lie within the 95% limit of agreement (Mean±1.96 SD), i.e., 0.34 to −0.31, 0.59 to −0.20, 0.39 to −0.48, and 0.39 to −0.29 mm for the manual outline, LGDF, WKVLS, and LSLSM, respectively. Meanwhile, there were only several differences between measurements by both methods that fall outside the limits of agreement.

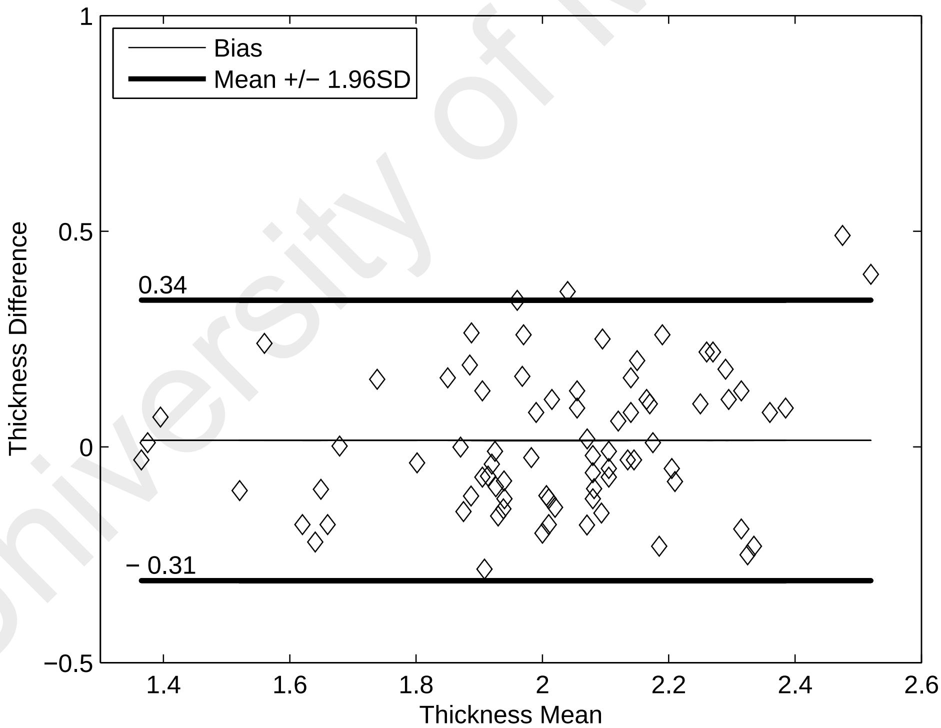

Figure 4.7: Bland-Altman plot for the thickness measurements obtained manually and by the normal distance on the cartilage area segmented by the manual outline.

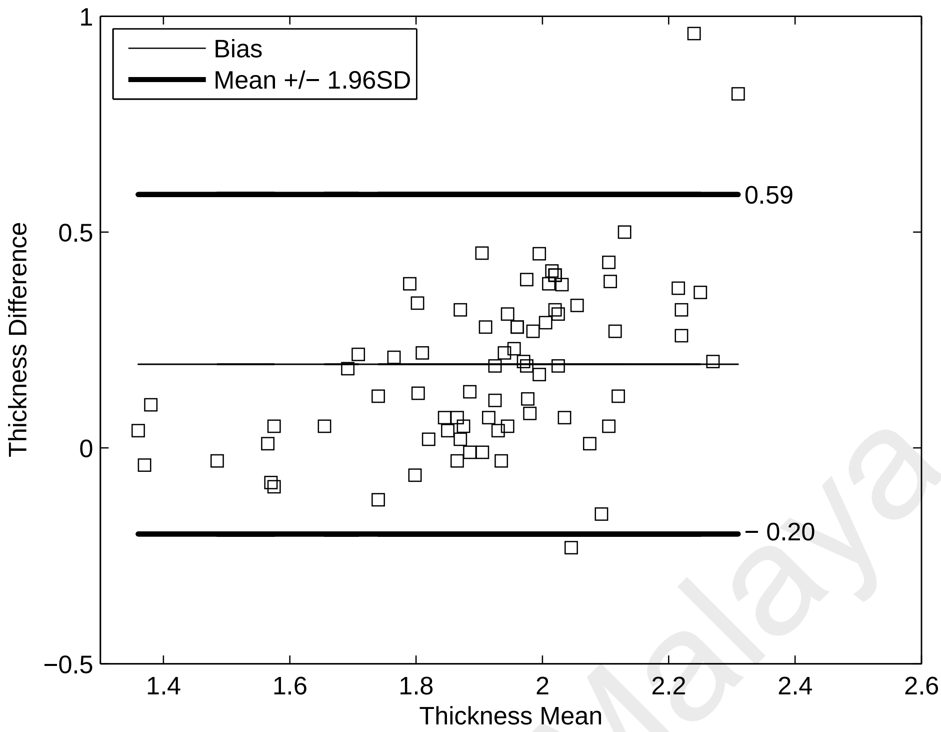

Figure 4.8: Bland-Altman plot for the thickness measurements obtained manually and by the normal distance on the cartilage area segmented by LGDF.

4.1.4 Summary

LSLSM was compared to the other two level set methods without and with multiplicative component estimation in the attempt of segmenting a real knee cartilage ultrasound image. Without multiplicative component estimation, LGDF fails to properly distinguish different tissues in the presence of noise and intensity bias. Meanwhile, simultaneous multiplicative bias field estimation helps WKVLS to cope with intensity inhomogeneity. It is shown that WKVLS produced more stable segmentation result than LGDF. As LSLSM considers the variances of Gaussian distributions of local image intensity in the multiplicative component estimation, LSLSM demonstrated to segment cartilage boundary more accurate than WKVLS, which ignored the variance component. It shows that using the energy derived from Gaussian distributions of local image intensity and multiplicative noise model helps to distinguish the boundary between different tissues that is not sufficiently distinct more

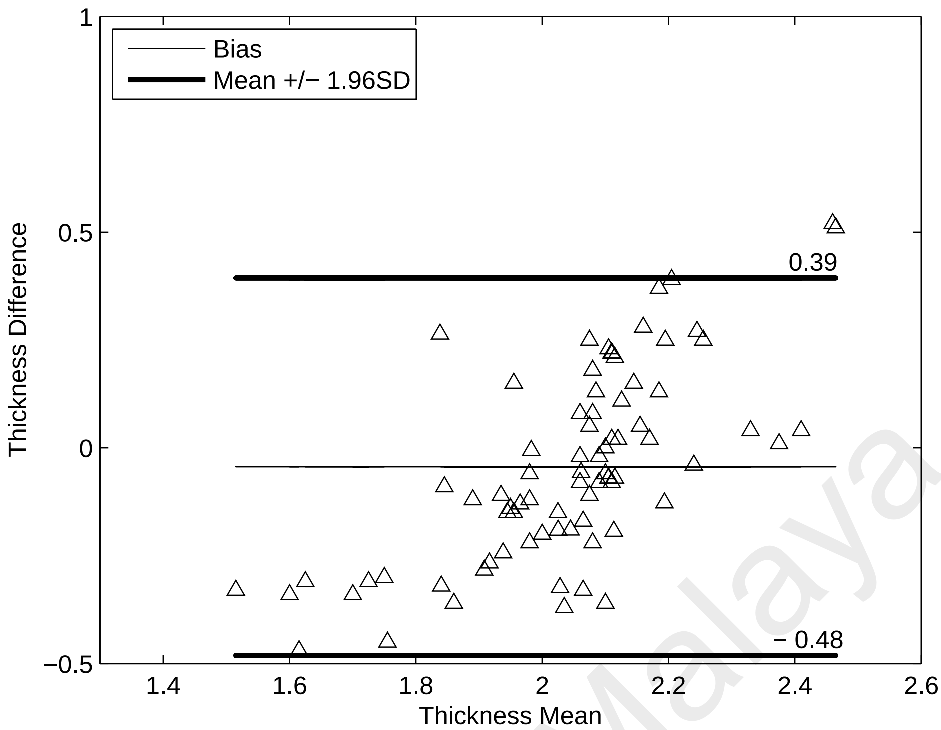

Figure 4.9: Bland-Altman plot for the thickness measurements obtained manually and by the normal distance on the cartilage area segmented by WKVLS.

satisfactorily in the noisy and bias-corrupted image. LSLSM obtained higher DSC value and smaller HD value than WKVLS and LGDF. It indicates that LSLSM has a higher area similarity and a minimally different shape compared toWKVLS and LGDF. In addition, it is shown that LSLSM required less computational time than WKVLS and LGDF. These results show that LSLSM yielded more satisfactory results than other level set methods in term of segmentation accuracy and computational time.

The segmentation performances of LGDF, WKVLS, and LSLSM when applied to a set of the real knee cartilage ultrasound images were evaluated qualitatively and quantitatively. Two experts assessed the overall segmentation quality of the cartilage anatomical structure in ultrasound images by differentiating the boundaries between the soft tissue-cartilage interface and the cartilage-bone interface. Inter-observer agreement for the segmentation quality of the cartilage area is expressed by the Cohen's κ statistics.

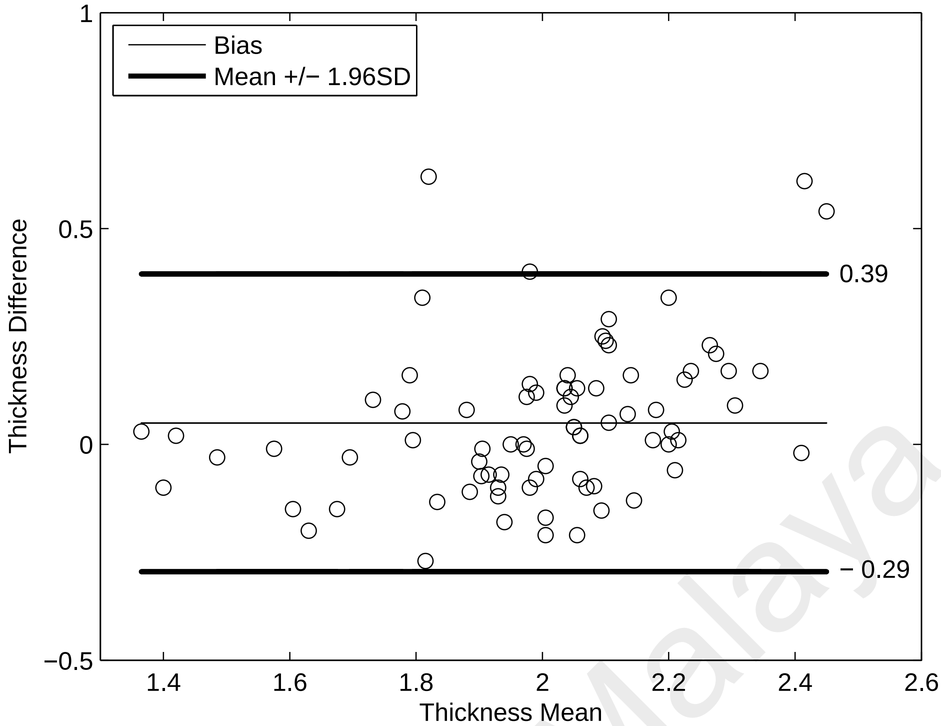

Figure 4.10: Bland-Altman plot for the thickness measurements obtained manually and by the normal distance on the cartilage area segmented by LSLSM.

The κ coefficient of 0.73 indicates a substantial agreement of the cartilage segmentation quality for all ten subjects rated by two experts. Next, two quantitative evaluation metrics of DSC and HD are adopted to examine the segmentation outcomes obtained by the three level set methods opposed to the gold standard obtained manually by an expert. To quantify area similarity between two comparing segmentation regions, DSC metric is used to compute the relative locations and sizes of the contour pair. Meanwhile, HD metric indicates the boundary mismatch between two comparing segmented boundaries. LSLSM was successfully applied in segmenting a set of the real knee cartilage in the 2-D ultrasound images. The average values of DSC metric for LGDF, WKVLS, and LSLSM over the total data set of 80 images were 0.91 ± 0.01, 0.73 ± 0.14, and 0.90 ± 0.02, respectively. The average values of HD metric for LGDF, WKVLS, and LSLSM over the total data set of 80 images were 6.33 ± 0.62, 8.32 ± 2.17, and 6.21 ± 0.59, respectively.

The two metrics indicates LSLSM had a very good agreement between the two compared contours. While the overall average value for DSC metric obtained by LSLSM was higher than the ones obtained by LGDF and WKVLS, the overall average value for HD metric obtained by LSLSM was smaller than the ones obtained by LGDF and WKVLS. While DSC metric is seen as a global measure of the area similarity between the contour pair, HD metric is more sensitive to local shape differences between the contour pair. It can be concluded that these evaluation metrics indicate LSLSM had a very good segmentation performance. The overall statistics illustrate quantitatively very good and consistent quality of the segmentation outcomes for all available data sets.

The satisfactory segmentation results are making the true thickness between two interfaces of the cartilage possible to be computed based on the 2-D segmented cartilage images using the normal distance. The obtained measurements of the cartilage thickness on a set of segmented cartilage areas indicate the robustness of the segmentation algorithm in segmenting various cartilage thickness. ICC value computed from a subset of the four repeated measurements demonstrates a good reproducibility of the thickness measurements. Bland-Altman plots demonstrate a good agreement between the thickness measurements obtained by the normal distance and the manual measurement. It can be observed that nearly all differences between measurements by both methods fall within the limit of agreement and there is no significant bias for the two methods. The measurement obtained by the normal distance does not differ much to the manual measurement, which is seen as gold standard.

The knee cartilage boundary segmentation possible with LSLSM has allowed the obtained segmentation results to be used for making the thickness computation of the cartilage in the 2-D ultrasound images. The obtained results show the accuracy and reproducibility of the segmentation and thickness estimation methods. The methods described in this work are useful to characterize the normal cartilage in the ultrasound images. The robustness in segmenting and computing various cartilage thickness demonstrated in this work indicate a potential application of the methods for the assessment of the knee cartilage degeneration.

4.2 Meniscus Ultrasound Image Segmentation

4.2.1 Comparison with Other Active Contour Models

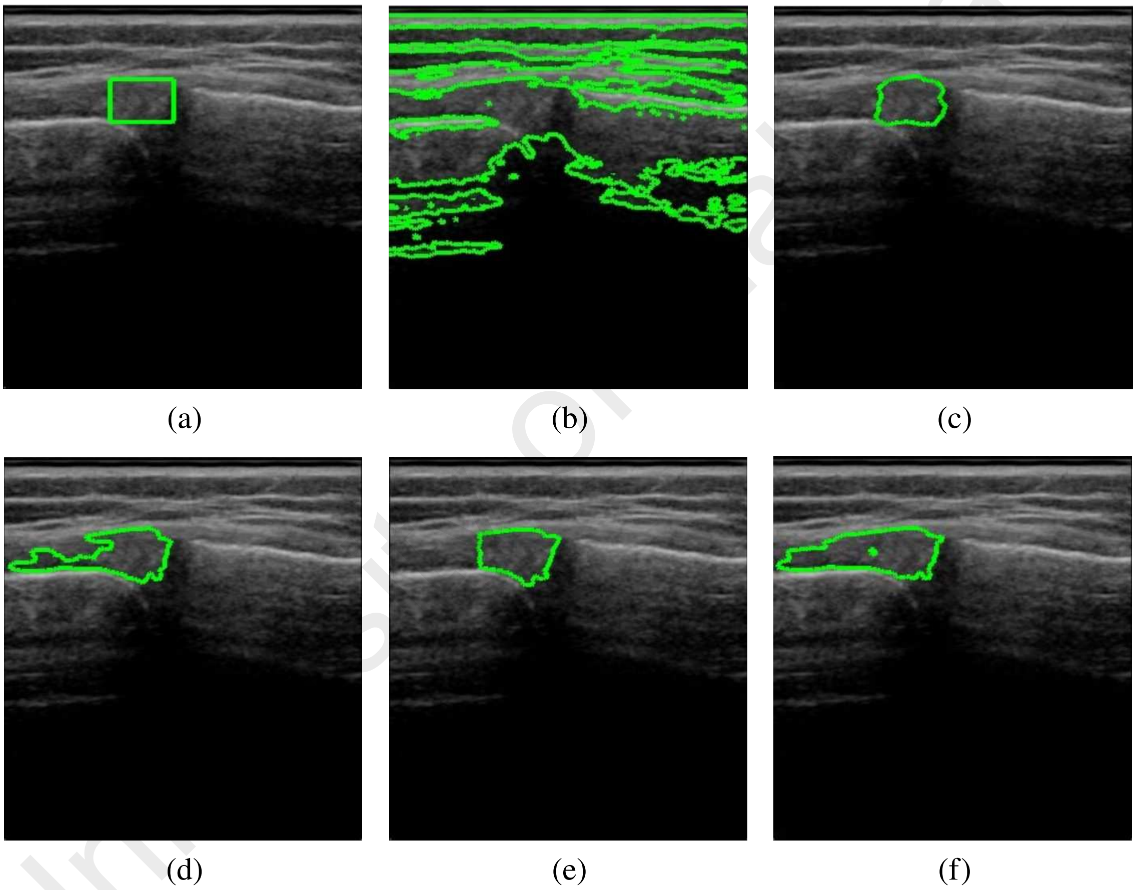

Figure 4.11: The segmentation results of the meniscus (green):(a) initial contour, final contour for (b) RSF (σ_K = 17), (c) GAC (α = 0), (d) LRAC (r = 10), (e) LRES (s = 15, Δs = 5, thres = 5), and (f) LREK (d = 10, Δd = 5, thres = 3).

In this subsection, the performance of LREK was compared to other active contour models in segmenting the meniscus ultrasound images. From the existing global regional, edge-based, and local regional active contour models, RSF, GAC, LRAC and LRES were picked, respectively. All the methods were implemented in MATLAB R2014a in an Intel

(R) Xeon (R), 2.00 GHz, 32 GB RAM. As depicted in Figure 4.11, the meniscus that has a shape with deep concavity is located in the upper-middle of the femoral condyle and the tibial plateau. The initial contour was placed similarly for all tested methods as in Figure 4.11(a). Figure 4.11(b)-(f) depict the final contours of RSF, GAC, LRAC, LRES, and LREK overlaid on the original image. Image size is 288×364 pixels. To evaluate the segmentation accuracy and convergence speed, the segmentation result of LREK in Figure 4.11(f) is used as the reference to compute DSC metric over 1000 iterations as plotted in Figure 4.12, where x and y-axes represent the iteration number and DSC metric, respectively. The computational time required by different active contour models is also presented in the Table 4.3.

With the scale of Gaussian kernel $\sigma_K = 17$, RSF considers local intensity and handles non-uniform intensity well. Convolving the local window to the entire image leads to partitioning the brighter intensity as the object while the darker one as the background. It is unable to locate the meniscus as the only desirable object among other surroundings.

Active contours with local information are sensitive to initial contour positions, which are required to be placed near the object. This limitation, on the other hand, gives advantages in obtaining a particular object among other undesired objects, depending on its initial position. They do not have a tendency to capture the entire object as opposed to RSF that partitions the image into bright and dark intensities.

To navigate the contour towards the object's edge, GAC relies on the image gradient. The speckle, often considered as false edge points, may prevent GAC from reaching the real boundary. Balloon force ($\alpha = 0$) can grow the contour either inward or outward direction with a small capture range and slow convergence, which impedes from penetrating into the boundary concavity of the meniscus. Another choice of α can help to gain a larger capture range, but making it sensitive to initial position. The contour may also pass through weak boundaries, particularly in the images with low contrast.

As active contours using local regional descriptors employ pixel intensity instead of edge pixels, they are more robust against noise (Lankton & Tanenbaum, 2008). They de-emphasize the role of image noise by computing intensity statistics within the local window. The contour can still evolve towards the boundary even though in the presence of noise. LRAC provides a more complete boundary than GAC although some areas are still excluded as the segmentation outcomes. In the shared boundaries between the femoral condyle and the meniscus, the contour evolves reaching the left part of the meniscus. Meanwhile, it only arrives at the half boundary of the upper part. With $r = 10$, the distance between the contour as the center of the circle and the boundary is too far. The problem of limited capture range prevents the contour from evolving into the middle area of the meniscus, which is considered as a homogeneous area. LRES, which utilizes extendable search lines for handling concave parts, is able to segment only into half of the meniscus area. In such low contrast images, the contour is confined in the middle area of the meniscus as shown in Figure 4.11(e). This is because the statistics on the long, thin search line may not reliably describe the local intensity to generate enough force to penetrate the other part of the meniscus.

RSF, GAC, LRAC, LRES, and LREK are set to iterate for 1000 iterations, their DSC values are plotted in Figure 4.12, and their computational times are summarized in Table 4.3. According to Figure 4.12, they converge at approximately 50, 100, 750, 150, and 700 iterations. Instead of locating the meniscus, RSF partitions the entire image. LREK converges faster than LRAC, yet gives more complete boundaries. Although its initial scale is set to 10 pixels similar to that of LRAC, the feature of expandable kernels results in a large capture range to propagate into the concave boundary of the meniscus as confirmed by the higher DSC values in Figure 4.12. Some other models result in less

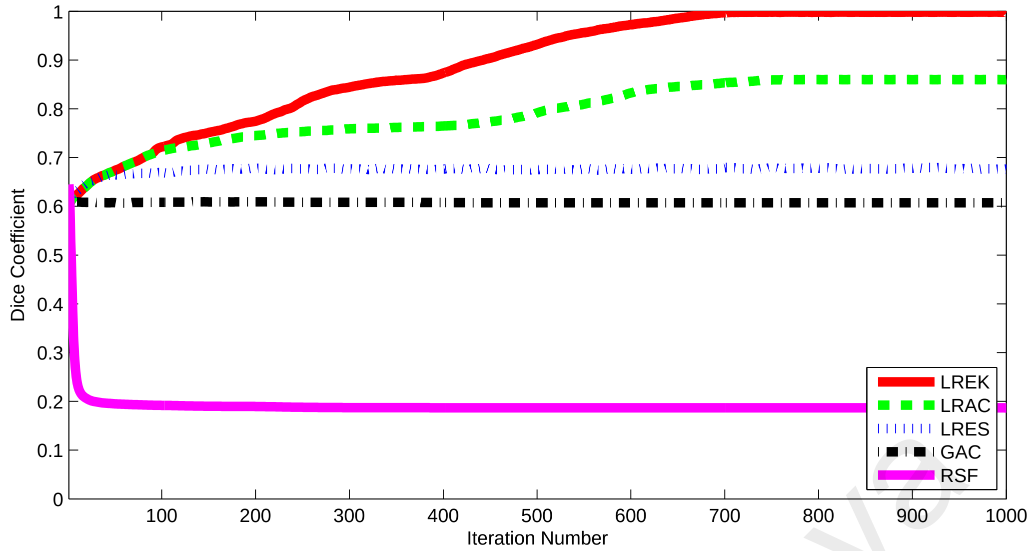

Figure 4.12: Convergence properties (from bottom up) of RSF, GAC, LRAC, LRES, and LREK active contours in segmenting the meniscus.

Table 4.3: Computational Time of Different Active Contour Methods

Methods	Total Time (s)
RSF	1,070
GAC	1,958
LRAC	215
LRES	7,630
LREK	232

complete boundaries due to their inability to move into the concave shape, thus giving smaller DSC values. With the speed of 7.63 seconds per iteration, LRES produces time consuming performance. It requires more computational steps to form two separate line regions inside and outside the contour and also to extend each of them as compared to LREK that just uses one kernel to form two local regions split by the contour line and to be expanded. This helps LREK to converge towards the intended boundary more rapidly than LRES. In addition, the scalability of the kernel to image size leads to a proportional computation in either small or large images. The total computational time required for RSF, GAC, LRAC, LRES, and LREK to converge are 54, 196, 161, 1,144, and 162 seconds, respectively.

4.2.2 Further Evaluations of the Proposed Method

In this subsection, the effect of several parameters of the proposed method in the segmentation results is further evaluated. In Section 4.2.2.1, the effects of threshold value selection in response to segmentation results as well as convergence properties are investigated. It was followed by a demonstration on how the presented multiple level set framework can avoid merging and overlapping between the neighbouring contours in Section 4.2.2.2. In Section 4.2.2.3, different choices of scale parameters that can be assigned for each zero level contour in multiple region segmentation and the accuracy improvement that can be achieved are shown.

4.2.2.1 Analysing the Threshold Value

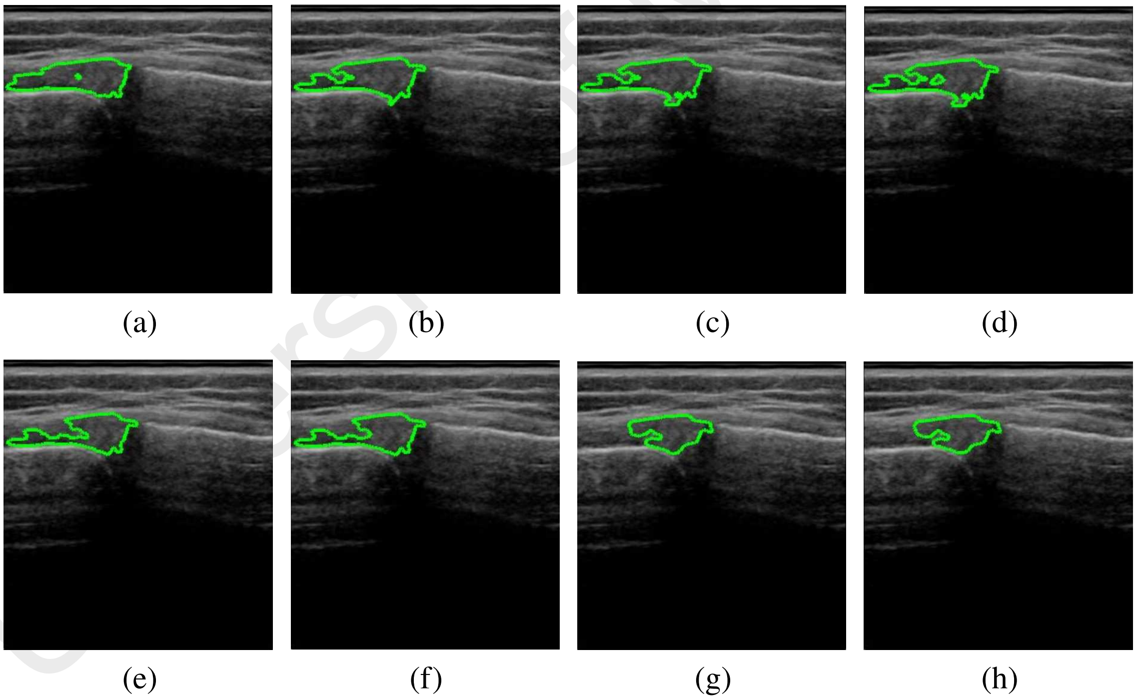

Figure 4.13: (a)-(h) Show segmentation results of LREK active contour on the meniscus (green) with thres $= 3, 5, 7, 9, 11, 13, 15,$ **and** 17**, respectively. Parameters** $d = 10$**,** $\Delta d = 5$**, and** $l = 1000$**.**

Another experiment is performed to investigate the choice of the threshold value thres, a key parameter in adapting the kernel size, in response to the segmentation accuracy. The performance of the single level formulation with various threshold values in segmenting a concave object of the meniscus is tested. Eight different values of thres are tested from 3 to 17 while setting other parameters as $d = 10$ and $\Delta d = 5$ and their final contours are plotted in Figure 4.13. Image size is 288×364 pixels. DSC metric is computed using the segmentation result in Figure 4.13(a) as the reference. The corresponding DSC values of these eight results are plotted over the number of iterations in Figure 4.14.

Figure 4.14 shows that the smallest value results in a more complete boundary of the meniscus. Meanwhile, the higher value of this parameter results in a less complete boundary. The two highest threshold values take the shortest time to converge at the same speed, however, into the least accurate segmentation. Two groups of intermediate values converge into two different speeds and segmentation accuracies. The first group with larger values converge faster, but into a less accurate outcome than the second group with smaller values. The smallest threshold value gives the lowest speed, but the most accurate outcome. This is because the contour requires more time to penetrate into the concave boundary. In essence, this experiment illustrates that the smallest threshold value enables the adaptation of the kernel size in order to detect the nearest boundary. The bigger value results in less ability of the kernel to expand and penetrate particular areas. Hence, the user may select a small threshold value to enable this feature and vice versa.

4.2.2.2 Multiple Region Segmentation

This experiment demonstrates multiple object segmentation using individual and multiple level set formulation without and with the additional constraint according to equations (3.17), (3.19), and (3.20), respectively. The goal is to partition image pixels into separate objects of the femoral condyle (FC), the meniscus (M), and the tibial plateau (TP). In Figure 4.15(b), each initial contour is placed in each object. For the result in Figure 4.15(d), three initial contours are embedded in a single level set function ϕ. Although the final contours are shown to locate each object with different positions, they do not provide

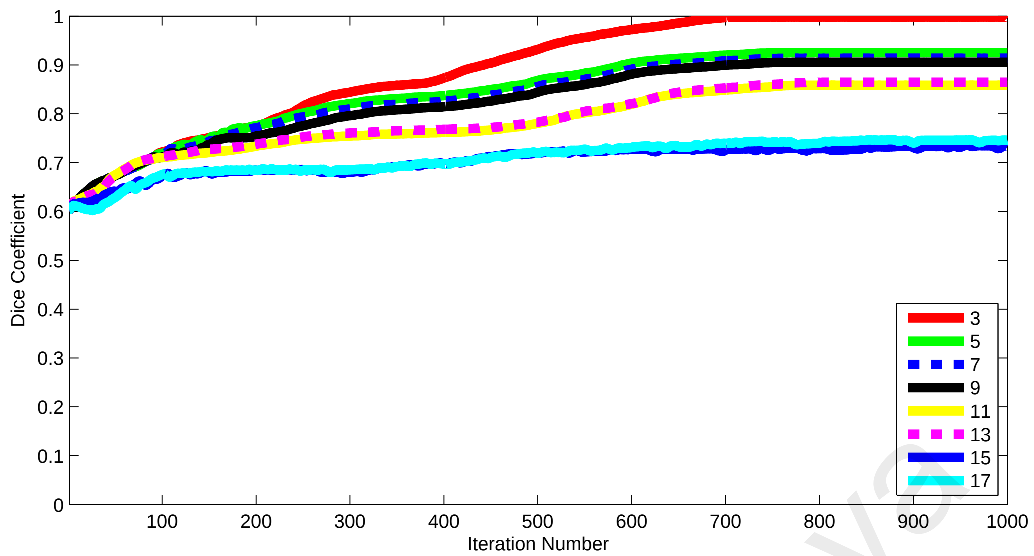

Figure 4.14: Convergence properties of LREK active contour for different threshold values in segmenting the meniscus.

a complete separate boundary between the meniscus and the tibial plateau. As multiple objects reside close to each other, merging between adjacent contours occurs in the shared boundaries, which is undesirable in this case.

To capture three separate object's regions, $n = 3$ is used to embed three initial contours using triple level set function $(\phi_i)_{i=1}^{3}$ as in Figure 4.15(e)-(f). Three sets of zero level of the contours ϕ_1, ϕ_2, and ϕ_3 to segment the femoral condyle, the meniscus, and the tibial plateau boundaries are accordingly coloured as red, green, and blue and overlaid on the original images. Although multiple initial contours overlapped with one another, the final contours in Figure 4.15(e) are positioned on each object without any merging between the adjacent contours. However, the neighbouring contours create an overlapping region in the shared boundaries between the meniscus and the tibial plateau where the contrast is low. Hence, the framework with additional constraint is used to prevent multiple contours from overlapping with each other as depicted in Figure 4.15(f). The corresponding area terms of the Heaviside function of these triple level set functions ϕ_1, ϕ_2, and ϕ_3 are $\sum_{p\neq 1} H_\epsilon(\phi_p) = H_\epsilon(\phi_2) + H_\epsilon(\phi_3)$, $\sum_{p\neq 2} H_\epsilon(\phi_p) = H_\epsilon(\phi_1) + H_\epsilon(\phi_3)$, and

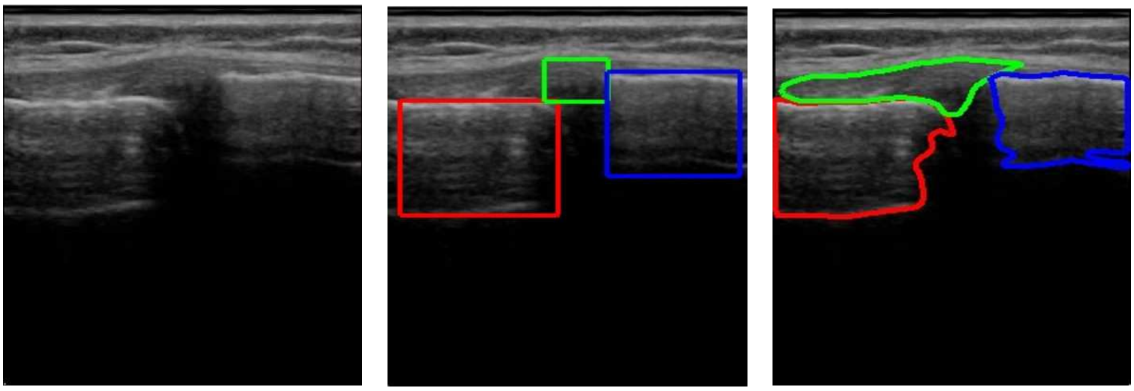

(a) Original image (b) Initial contours (c) Manually traced contours

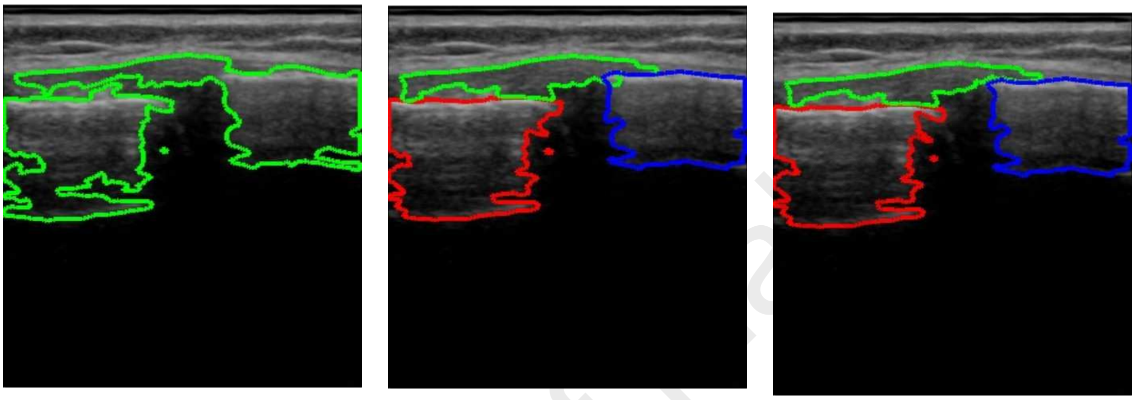

(d) Final contours of the single level set (e) Final contours of the multiple level set without constraint (f) Final contours of the multiple level set with constraint

Figure 4.15: Simultaneous segmentation of the femoral condyle (red), the meniscus (green), and the tibial plateau (blue) with parameters (d = 15 and Δd = 3) for (c), ($d_{\mathbf{FC}} = d_{\mathbf{TP}} = 8$, $d_{\mathbf{M}} = 15$, and $\Delta d_{\mathbf{FC}} = \Delta d_{\mathbf{M}} = \Delta d_{\mathbf{TP}} = 3$) for (d) and (e), thres = 3, and $l = 1100$.

$\sum_{p \neq 3} H_\epsilon(\phi_p) = H_\epsilon(\phi_1) + H_\epsilon(\phi_2)$, respectively. Within one time step, these triple level set functions are updated. When evolving ϕ_1, another two level set functions ϕ_2 and ϕ_3 are described by their Heaviside functions $H_\epsilon(\phi_2)$ and $H_\epsilon(\phi_3)$, respectively, and vice versa. As a result, the multiple contours are evolved simultaneously to the desired boundaries of the femoral condyle, the meniscus, and the tibial plateau in a single image without any merging and overlapping between the neighbouring contours. This is confirmed by DSC and HD values computed from the segmented and manually traced contours in Figure 4.15(c) using single and multiple level set formulation without and with the additional constraint, which are summarized in the first, second, and third rows of the matrices $\begin{bmatrix} 0.9155 & 0.7731 & 0.9430 \\ 0.9061 & 0.7734 & 0.9434 \end{bmatrix}$ and $\begin{bmatrix} 5.5678 & 5.9161 & 5.4772 \\ 5.5678 & 6.4807 & 4.8990 \end{bmatrix}$, respectively.

4.2.2.3 Multiple Scale Parameters

Various parameters are demonstrated to be assigned differently for each zero level contour. Figure 4.15 shows that different scales for each zero level contour in Figure 4.15(e)-(f) may increase segmentation accuracy compared to Figure 4.15(d) that produces a less accurate result. This is because the parameters' values cannot be set to be different for those three contours, which are embedded in a single level set function.

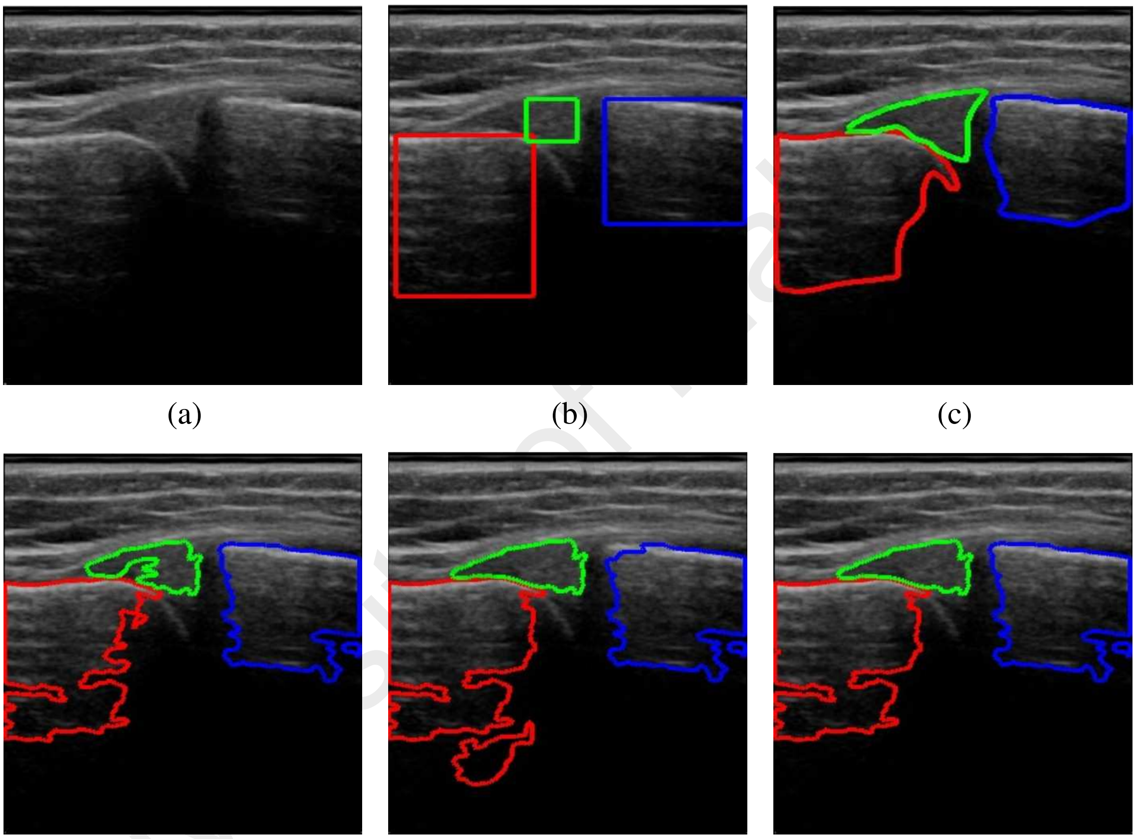

(a) (b) (c)

(d) (e) (f)

Figure 4.16: (a) Original image, (b) initial, (c) the manual outline, and final contours on the femoral condyle (red), the meniscus (green), and the tibial plateau (blue) (d) with $d_{\mathbf{FC}} = d_{\mathbf{M}} = d_{\mathbf{TP}} = 13$ and $\Delta d_{\mathbf{FC}} = \Delta d_{\mathbf{M}} = \Delta d_{\mathbf{TP}} = 5$, (e) with $d_{\mathbf{FC}} = d_{\mathbf{M}} = 12$, $d_{\mathbf{TP}} = 13$, $\Delta d_{\mathbf{FC}} = 5$, and $\Delta d_{\mathbf{M}} = \Delta d_{\mathbf{TP}} = 3$, and (f) with $d_{\mathbf{FC}} = d_{\mathbf{M}} = 12$, $d_{\mathbf{TP}} = 13$, $\Delta d_{\mathbf{FC}} = \Delta d_{\mathbf{M}} = 3$, and $\Delta d_{\mathbf{TP}} = 5$. Parameters $thres = 3$ and $l = 700$. Image size is 288 × 364 pixels.

In Figure 4.16, different choices of scale parameters in the presented multiple level set framework are compared. Similar choice of scale parameters for each zero level contour ($d = 13$ and $\Delta d = 5$) may not produce an accurate segmentation for every object as some excluded areas are found in the segmentation outcome in Figure 4.16(d). With different scales for each zero level contour, some improvements are observed on the femoral condlye and the meniscus boundaries in Figure 4.16(e). However, the contour on the femoral condyle are splitting and developing new areas due to the scale step being too large, i.e., $\Delta d_{\mathrm{FC}} = 5$. On the other hand, the corner area in the upper left of the tibial plateau is excluded because the scale step is too small ($\Delta d_{\mathrm{TP}} = 3$). Therefore, $\Delta d_{\mathrm{FC}} = 3$ for the femoral condyle and $\Delta d_{\mathrm{TP}} = 5$ are set for the tibial plateau to improve the segmentation accuracy. Meanwhile, the choice of Δd_{M} to be 3 or 5 is shown to produce no effect on the meniscus part. In addition, although two initial contours between the femoral condyle and the meniscus created an overlap region, the region vanishes after the contours have evolved. DSC and HD values for the segmentation results in Figure 4.16(d), (e), and (f) summarized accordingly in the first, second, and third rows of the matrices $\begin{bmatrix} 0.8724 & 0.7902 & 0.9244 \\ 0.8691 & 0.8543 & 0.9153 \\ 0.9137 & 0.8543 & 0.9245 \end{bmatrix}$ and $\begin{bmatrix} 4.2426 & 4.8990 & 4.8990 \\ 4.3589 & 4.5826 & 4.4721 \\ 4.2426 & 4.5826 & 4.8990 \end{bmatrix}$ confirm that different scale parameters assigned to the multiple objects of different size and shape can improve the segmentation accuracy.

In summary, the value of d affects the accuracy of contour placement on the boundary once the kernel has found the boundary. As long as the kernel contains enough information, the position is least affected and generally accurate. In addition, the value of Δd determines the gradual increase of the kernel scale when expanding in order to detect the nearest boundary. If the value of this parameter is too large, it results in sudden changes to the scale and causes splitting contours developing new areas despite the main contour still capturing the boundary. However, if the value is too small, the contour is unable to reach some of the object region. Hence, a proper choice of both scales will result in a gradual expansion of the kernel and an accurate contour placement in the boundary.

4.2.3 Meniscus Ultrasound Image Segmentation

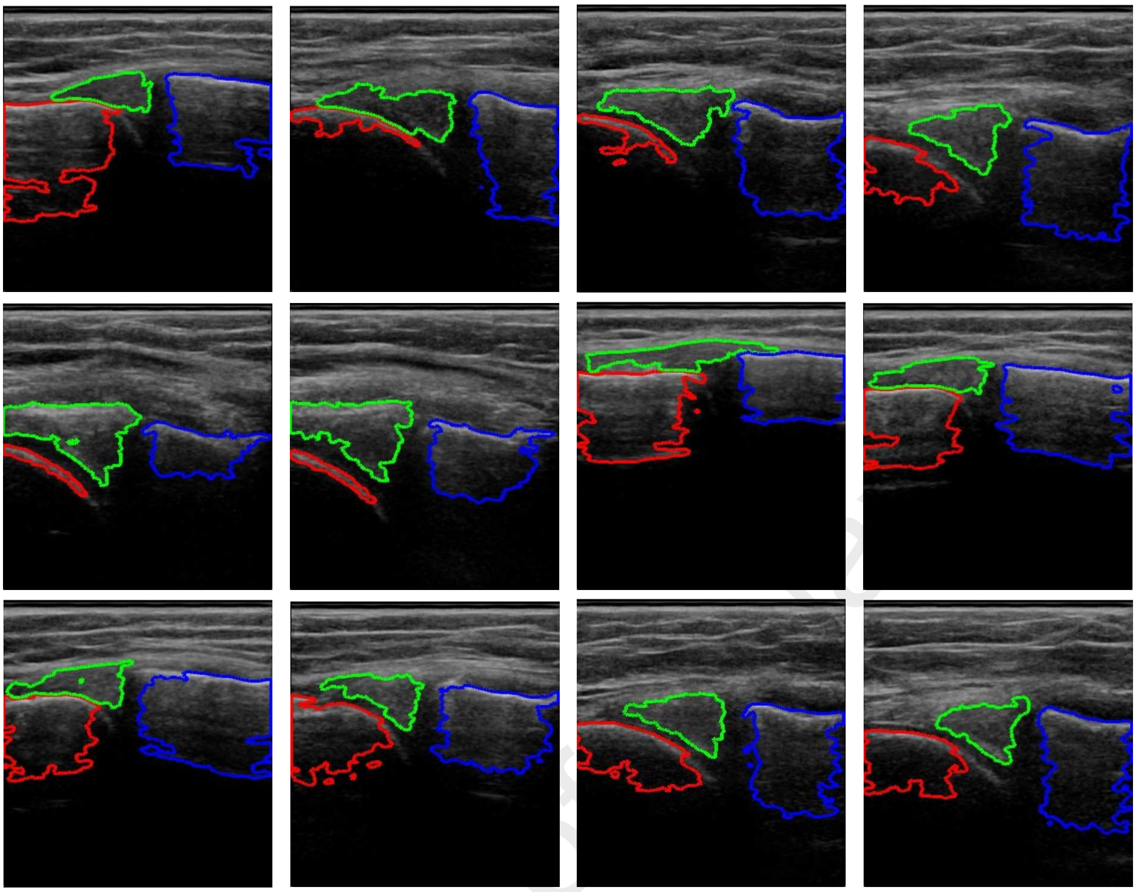

Figure 4.17: A subset of 12 segmentation outcomes of the femoral condyle (red), the meniscus (green), and the tibial plateau (blue) that represents variation in size, shape, and position of the objects.

In this subsection, an application of the proposed framework to segment a set of real meniscus ultrasound images is presented. Figure 4.17 depicts a subset of 12 segmentation outcomes that represents variation in size, shape, and position of the objects from datasets of 70 images. The data sets that consist of 3, 4, and 5 images were available from 10, 5, and 4 subjects, respectively. For these datasets, thres = 3, l = 1000, d_{FC}, d_{M}, and d_{TP} are set to be 8, 10, 12, 13, 14, or 15, and Δd_{FC}, Δd_{M}, and Δd_{TP} to be 3 or 5. Although Figure 4.17 has indicated visually satisfactory results, a precise assessment to quantify the segmentation performance is of great concern. Over the total datasets of 70 images, DSC and HD metrics are computed from contours obtained by MLREK and traced manually by the expert as shown in Figure 4.18 and 4.19, respectively. Each contour of the objects was segmented separately.

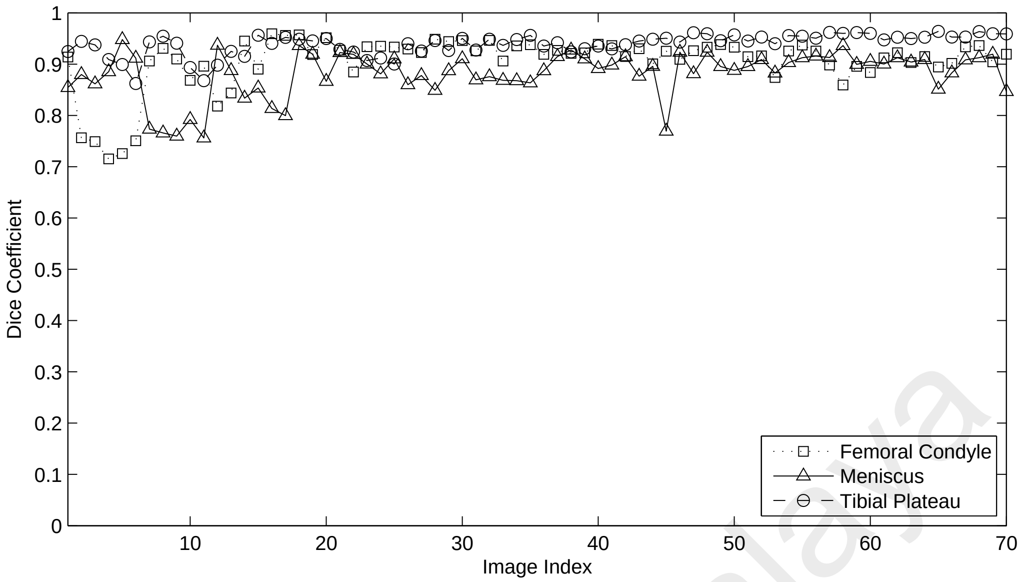

Figure 4.18: DSC measures of the femoral condyle, the meniscus, and the tibial plateau over 70 images.

DSC values in the graph vary from 0.72 to 0.96. The value above 0.7 indicates that the two compared regions have a close similarity in area and location one and another (Zijdenbos, Dawant, Margolin, & Palmer, 1994). The value greater than 0.8 indicates a better similarity area, which provides more satisfactory and less inaccurate segmentation outcomes. Meanwhile, HD values are ranging from 2.65 to 8.78 pixels where a smaller value indicates that two compared shapes differ minimally each other. These values are quite small compared to image size of 288×364 pixels. Such a range in DSC and HD values may be influenced by the low-contrast areas and weak boundaries that are excluded in the segmentation outcomes. It may be caused by the scatter distribution of speckle noise that varies the contrast of the object ranging from low to high intensity changes. Although the local model suffers sensitivity to initialization and scale parameters (Lankton & Tanenbaum, 2008), the results have demonstrated the robustness against various shapes, sizes, and positions of the objects.

The mean of DSC and HD measures for all objects in Table 4.4 falls in the range of

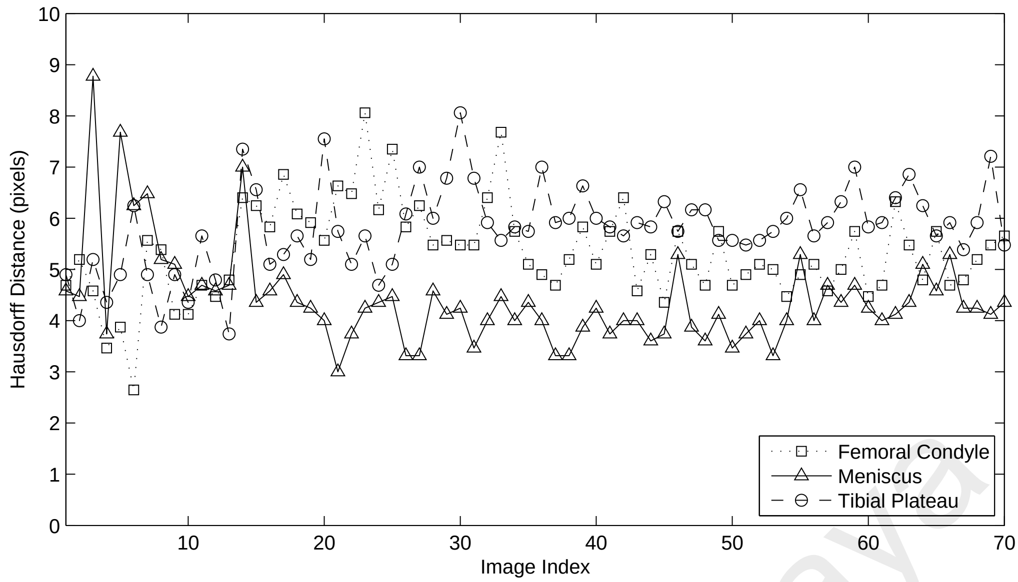

Figure 4.19: HD measures of the femoral condyle, meniscus, and tibial plateau over 70 images.

0.88 and 0.94 and of 4.41 and 5.80 pixels, demonstrating a good segmentation quality. Meanwhile, the standard deviation for DSC metric is between 0.02 and 0.04 and for HD metric is between 0.83 and 0.97 pixels, indicating that MLREK provides consistent outcomes. ICC values in Table 4.4 computed from DSC values of a set of three segmentation results indicate a good reproducibility of the segmentation results of the femoral condyle, the meniscus, and the tibial plateau. Despite these good and consistent outcomes confirm the visually pleasing results in Figure 4.17 and reflects a good agreement with its ground truth, an in-depth study of the framework application for assessment of the meniscus degeneration and displacement is very interesting for future work. For example, DSC values below 0.8, which have more than 20% area discrepancy may not be accurate for use in the area quantification, particularly for the degeneration detection.

Table 4.4: Statistics of the Measures

	Femoral Condyle	**Meniscus**	**Tibial Plateau**
DSC	0.91 ± 0.05	0.88 ± 0.04	0.94 ± 0.02
HD (pixels)	5.35 ± 0.91	4.41 ± 0.97	5.80 ± 0.83
ICC	0.8990	0.7040	0.8989

Figures 4.20, 4.21, and 4.22 illustrate Bland-Altman plots for DSC measures of the femoral condyle, the meniscus, and the tibial plateau, respectively. Bland-Altman plots depicted in the graphs illustrate a good agreement between two segmentation results of the three objects. The mean differences for all pairs of the measurements were 0.006 ± 0.034, 0.006 ± 0.057, and 0.004 ± 0.015 for the femoral condyle, the meniscus, and the tibial plateau, respectively. The mean difference is near zero indicating no significant bias for both measurements. It can also be observed that the data points fall within the 95% confidence interval (Mean±1.96 SD), i.e., 0.07 to −0.06, 0.12 to −0.11, and 0.03 to −0.03 the femoral condyle, the meniscus, and the tibial plateau, respectively. Meanwhile, there were only several differences that fall outside the limits of agreement.

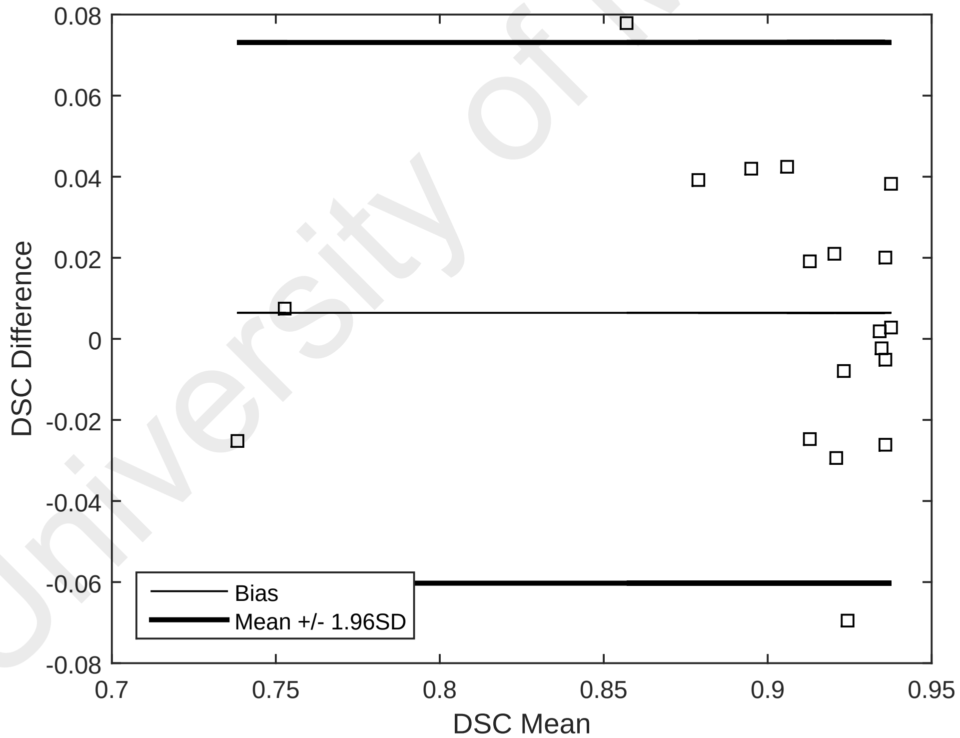

Figure 4.20: Bland-Altman plots for DSC measures of the femoral condyle.

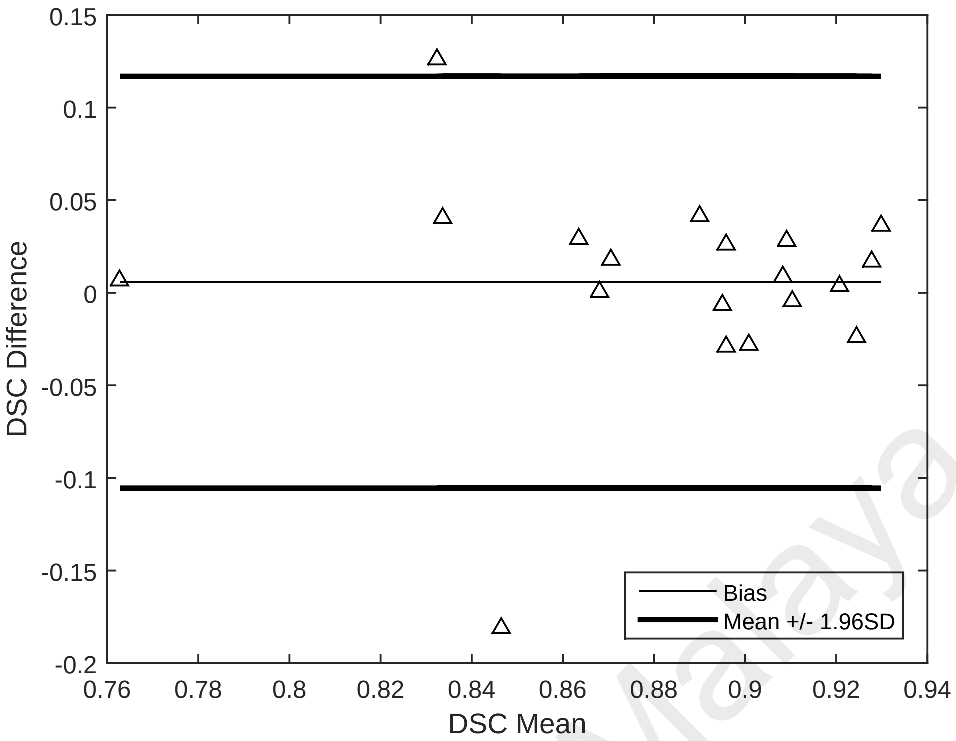

Figure 4.21: Bland-Altman plots for DSC measures of the meniscus.

4.2.4 Summary

The presented active contour model was compared to other related active contour models in the attempt of segmenting the meniscus ultrasound images. While other methods failed to penetrate into boundary concavity, the presented model segmented the desired structures satisfactorily. Instead of locating the meniscus only, RSF partitions the image according to brighter and darker intensities. Speckle noise, often considered as false edge points, impedes GAC from reaching the concave boundary of the meniscus. The problem of limited capture range prevents LRAC from penetrating into the middle area of the meniscus as a result it is excluded as the segmentation outcome. In the low contrast images, the statistics on the extendable search line is unable to generate enough force to move LRES's contour into the concave parts of the meniscus, hence, is confined in the middle area of the meniscus. Evaluation outcomes also include an examination of the convergence speed and the computational time required for the contour evolution. It shows an improvement

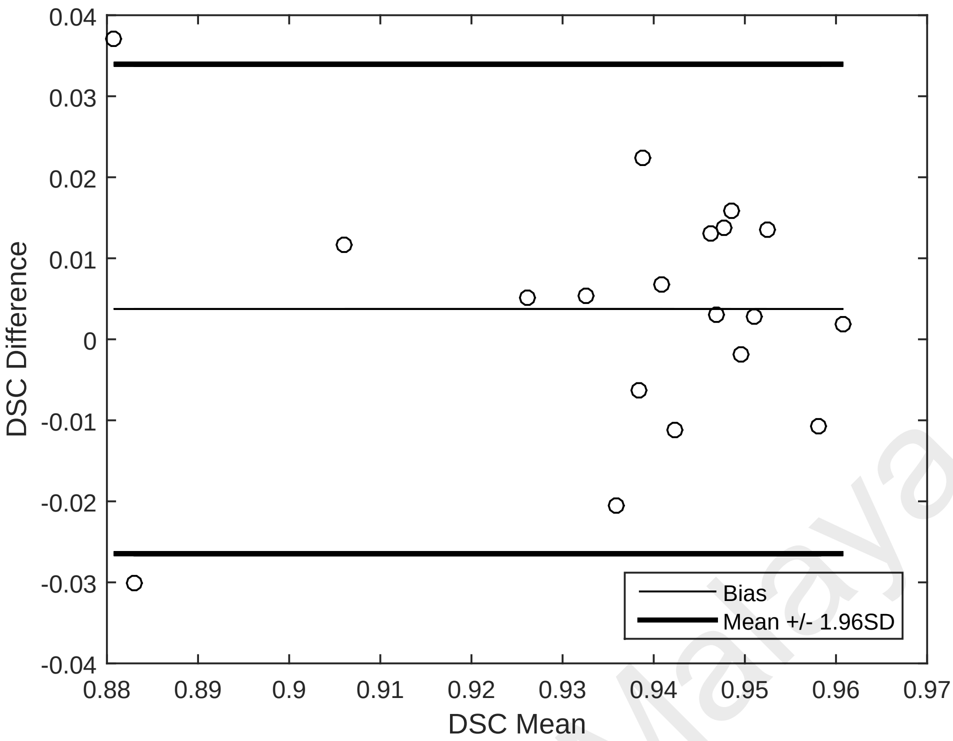

Figure 4.22: Bland-Altman plots for DSC measures of the tibial plateau.

achieved by the presented method in terms of segmentation results, computational time, and convergence speed. RSF, GAC, LRAC, LRES, and LREK converge at approximately 50, 100, 750, 150, and 700 iterations consuming computational time of 53.52, 195.79, 161.18, 1,144.49, and 162.47 seconds, respectively. In other words, LREK propagates into the concave shape of the meniscus providing more complete boundaries, efficient computation, and faster convergence.

Further evaluation was performed by investigating the choice of various parameters in MLREK and their responses to the segmentation results. It was conducted by examining the effect of the threshold value, the algorithm's ability to simultaneously segment an image with multiple structures, and the effect of assigning various parameters for each zero level contour on the segmentation results. First, the effects of the threshold value selection in response to the segmentation accuracy as well as convergence properties are investigated. Our experiment with varying the threshold value illustrates how it should be chosen to adapt the kernel size in order to successfully reach the concave parts. It shows that the smallest threshold value enables in adapting the kernel size in order to detect the nearest boundary. Meanwhile, the bigger value results in less ability of the kernel to expand and penetrate particular areas. Hence, the user may select a small threshold value to enable this feature and vice versa. Second, a demonstration of the algorithm's ability to simultaneously segment multiple structures using single and multiple level set formulation with and without an additional constraint is conducted. When a single level set function is used to embed multiple initial contours, merging between adjacent contours occurs in the shared boundaries of multiple objects that reside closely each other. Next, the multiple contours are embedded in multiple level set functions where each level set function represents one object's region. Although there is no merging between multiple contours, the neighbouring contours overlapped each other in the shared boundaries. On the other hand, the multiple level set framework with additional constraint demonstrated to prevent merging and overlapping between the adjacent contours, and thus performed simultaneous segmentation of separate objects all at once in a single image. Third, a flexible choice in assigning different parameter settings in this multiple active contours framework is illustrated. Different choices of scale parameters can be assigned for each zero level contour in multiple structure segmentation. Different scales for each zero level contour are shown to increase segmentation accuracy compared to multiple contours embedded in a single level set function that produce a less accurate result due to the scale parameters cannot be set to be different for each zero level contour. An improvement in the segmentation accuracy can be achieved by assigning different scale parameters for each level set function when segmenting multiple structures of different size and shape.

A precise assessment to quantify the segmentation performance is demonstrated through the application of MLREK in segmenting over a set of 70 real meniscus ultrasound images. The segmentation outcomes obtained by the algorithm were examined by comparing to the manual segmentation obtained by the expert using both DSC and HD metrics. DSC and HD values for each image were reported for the each of these anatomical regions.DSC metrics for the femoral condyle, the meniscus, and the tibial plateau have the overall average values of 0.91 ± 0.05, 0.88 ± 0.04, and 0.94 ± 0.02, respectively. HD metrics for the femoral condyle, the meniscus, and the tibial plateau have the overall average values of 5.35 ± 0.91, 4.41 ± 0.97, and 5.80 ± 0.83 pixels, respectively. It can be concluded that the overall average value of DSC and HD metrics for the three objects for the total data set of 70 images indicates a very good and consistent segmentation performance. It shows that the segmentation outcomes have a good agreement with the manual segmentation. Meanwhile, ICC value computed from DSC values of three repeated scanned images indicates a good reproducibility of the segmentation results of the three structures. Bland-Altman plot demonstrates a good agreement between the segmentation results from two repeated scan images. Nearly all data points between the two methods fall within the limit of agreement where the bias is near zero. It implies that the segmentation results between two repeated scanned images does not differ each other.

The experimental results showed that MLREK was successfully applied in segmenting the desired multiple objects over a set of real meniscus ultrasound images. Simultaneous segmentation of the multiple objects achieves an acceptable level of accuracy. The validation metrics computed for the three objects demonstrate MLREK had a very good segmentation performance and an excellent agreement between two comparing contours. The robustness and accuracy of MLREK in locating the desired multiple objects of the femoral condyle, meniscus, and tibial plateau with various shapes, sizes, and positions have indicated a potential application of MLREK for assessment of the meniscus degeneration and displacement in an ultrasound image.

CHAPTER 5: CONCLUSION AND FUTURE WORK

In this chapter, conclusion and future work of this thesis are discussed. The conclusion of this thesis is given in Sections 5.1, which will be elaborately discussed in Sections 5.1.1 and 5.1.2. Some recommendations on possible directions to guide research works in the future are given in Section 5.2.

5.1 Conclusion

The cartilage segmentation and thickness computation methods and the meniscus segmentation method for the 2-D ultrasound images have been presented in this thesis. The performance of the cartilage segmentation and thickness computation methods and the meniscus segmentation method on real clinical data sets have been evaluated qualitatively and quantitatively.

5.1.1 Cartilage Segmentation and Thickness Computation

The knee cartilage boundary segmentation using LSLSM and thickness computation using the normal distance in short axis knee cartilage of the 2-D ultrasound images have been presented. The energy functional derived from Gaussian distributions of local image intensity and multiplicative noise model has allowed LSLSM to cope with speckle noise and intensity bias thus capture the monotonous hypoechoic band between the two interfaces of the soft tissue-cartilage and the cartilage-bone that represents the cartilage region. The cartilage thickness is then automatically computed by averaging the normal distances along the segmented cartilage area.

When LSLSM was compared to the other two level set methods without and with multiplicative component estimation in the attempt of segmenting a real knee cartilage ultrasound image, it shows that LSLSM yielded a better segmentation result than other methods. Inter-observer agreement expressed by the κ coefficient indicates a substantial agreement of the cartilage segmentation quality for all ten subjects rated by two experts. The overall statistics of the evaluation metrics of DSC and HD illustrate that LSLSM had a very good and consistent quality of the segmentation outcomes for the total data set of 80 images. The obtained measurements of the cartilage thickness on a set of segmented cartilage area indicates the robustness, reproducibility, and agreement of the segmentation algorithm in segmenting various cartilage thickness.

The knee cartilage boundary segmentation possible using LSLSM has allowed the obtained segmentation results to be used for computing the cartilage thickness in the 2-D ultrasound images. The robustness in segmenting and computing cartilage of various thickness demonstrated in this work indicates a potential application of the methods for the assessment of the knee cartilage degeneration in an ultrasound image. It can be applied to assess the cartilage degeneration typically seen as the cartilage thinning where changes in the cartilage thickness can be quantified over time by comparing the true thickness at a certain time interval. The assessment of the cartilage degeneration using the methods described needs to be investigated further and is left for future work.

5.1.2 Meniscus Ultrasound Image Segmentation

The multiple LREK active contours (MLREK) have been presented to address simultaneous segmentation of the femoral condyle, the meniscus, and the tibial plateau. The use of local region descriptor helps to provide a desired segmentation result in the presence of spatial intensity variation caused by the multiplicative noise. In order to successfully penetrate into the boundary concavity, the scale of the local region for each contour point is adaptable during the segmentation process and is dependent on the distance of this point to the nearest boundary. The multiple level set formulation is provided to segment multiple regions of interest without merging and overlapping between neighboring contours.

When the presented active contour model was compared to other related active contour models in the attempt of segmenting meniscus ultrasound images, it shows an improvement in terms of segmentation performance, computational time, and convergence speed offered by the presented method. Further evaluation was performed by investigating the choice of various parameters in MLREK and their responses to the segmentation results. Our experiment with varying the threshold value illustrates how it should be chosen to adapt the kernel size in order to successfully reach the concave parts. The multiple active contours framework with the additional constraint demonstrates to prevent merging and overlapping and performs simultaneous segmentation of separate objects all at once in a single image. A flexibility in assigning different parameter settings for each zero level contour in this framework shows an improvement in the segmentation accuracy when segmenting multiple objects of different size and shape. When MLREK was applied in segmenting the femoral condyle, the meniscus, and the tibial plateau for the total data set of 70 images, the validation metrics DSC and HD computed demonstrate a very good and consistent segmentation performance, reflecting that the segmentation outcomes have a good agreement with the manual segmentation.

Simultaneous segmentation of the three objects on a set of the meniscus ultrasound images has demonstrated the robustness of the segmentation algorithm to shape variations of the objects. While the focus of this work was on the segmentation of the meniscus in the ultrasound images, the overall statistics indicates a potential application of the framework for the assessment of the meniscus degeneration and displacement in an ultrasound image. It can be applied to assess the meniscus degeneration and displacement typically seen as the changes in the meniscus area and position. Thus, the changes in the meniscus area and position can be quantified over time by comparing the meniscus area and position before and after the degeneration or displacement occurred. An in-depth study of the framework application for the assessment of the meniscus degeneration and displacement is interesting for future work.

5.2 Future Work

Several interesting and worth pursuing research topics that will extend the work in this thesis are described in the following subsections.

5.2.1 Assessment of the Knee Cartilage Degeneration

Once the cartilage in the ultrasound images has been segmented, a diagnostically useful parameter that characterizes the cartilage such as the cartilage thickness can be measured, which can tell how much the degeneration is progressed in the cartilage. This parameter is useful to characterize normal or pathological cartilage with assistance from medical experts in providing descriptive knowledge about the signs of cartilage abnormality. The cartilage segmentation and thickness computation methods could be clinically useful as part of ultrasound scanning routine of the knee joint to produce data that may yield diagnostically significant trends in the cartilage degeneration. In principle, the cartilage segmentation and thickness computation are an important initial step in order to quantify the cartilage degeneration. Segmentation of the cartilage on a set of real knee cartilage ultrasound images has demonstrated the robustness against various shapes and sizes of the object. Early diagnosis and monitoring of the disease progression is possible by measuring the cartilage thickness before and after the degeneration. Change in the cartilage thickness can be quantified over time through the comparison of the true thickness at a certain time interval. In order to compare cartilage thickness before and after the degeneration, the assessment of the cartilage degeneration requires at least two (or more) observations of the degeneration occurrence. As the cartilage degeneration may occur in a subject after a long period of time, i.e., six month intervals, monitoring this occurrence in the patient would spend some time too.

Although segmentation and the thickness computation of the normal cartilage in the ultrasound images still pose a considerable challenge and clinical value, the inclusion of different grade of cartilage degeneration and other pathological change in the cartilage to investigate the performance of the segmentation and thickness computational techniques to various degeneration progression could also guide future work. Future improvement also includes reducing or eliminating two user interactions involved in this work, i.e., the contour initialization and the extraction of the cartilage region from surrounding tissues. The incorporation of the joint shape-intensity prior constraint in (J. Wang, Cheng, Guo, Wang, & Tamura, 2016) to LSLSM could potentially increase the robustness in capturing the shape and thickness variations in the cartilage.

5.2.2 Registration of the short axis view of 2-D ultrasound image of the knee cartilage to the 3-D MRI volume

The cartilage segmentation and thickness computation in the 2-D ultrasound images are limited to a specific view taken by the 2-D ultrasound probe. It has limitations compared to the one performed in the 3-D MRI images reconstructed from the 2-D image stack. In order to describe precisely the relation between the thickness computation in the 2-D ultrasound short axis knee cartilage image plane and the 3-D cartilage surface obtained from the 3-D reconstruction of the 2-D MRI segmentation of para-sagittal knee cartilage slices or a direct 3-D MRI segmentation, the thickness measurements performed in the 2-D cartilage boundary and the 3-D cartilage surface need to be compared. The 2-D ultrasound short axis knee cartilage image plane is seen as the projected image plane from the real 3-D MRI volume of the knee joint. The thickness measurement using the perpendicular line in the 2-D cartilage boundary may not be seen perpendicular between upper and lower surfaces in the real 3-D cartilage surface. Hence, spatial registration of the 2-D ultrasound image plane to the 3-D MRI volume can provide a precise comparison of the thickness measurements. A rigid-body geometrical transformation can be applied to spatially align the 2-D ultrasound planar image into the 3-D MRI volumetric data. A prior knowledge of the orientation of the ultrasound probe in the acquisition protocol with respect to 3-D axes of the knee joint of the subject can be used to determine the position of the 2-D ultrasound image plane in the 3-D MRI volumetric data. A cross-sectional 2-D MRI image plane, which has the same orientation with the 2-D ultrasound image plane, is interpolated from the 3-D MRI volume. Thus, the thickness measurement in the interpolated cross-sectional 2-D MRI and the 2-D ultrasound planar images can be compared more precisely.

5.2.3 Assessment of the Meniscus Degeneration and Displacement

Once the femoral condyle, the meniscus, and the tibial plateau in the ultrasound images have been segmented, some diagnostically useful parameters that characterize the meniscus including the area and position of the meniscus can be extracted, which tell how much the degeneration and displacement are progressed in the meniscus, respectively. These parameters are useful to characterize normal or pathological meniscus with assistance from medical experts in providing descriptive knowledge about the signs of meniscus abnormality. In principle, the multiple structure segmentation of the femoral condyle, the meniscus, and the tibial plateau is an important step in order to determine the area and position of the meniscus where the measurement accuracy will highly rely on the segmentation accuracy itself. The methods could be clinically useful as part of ultrasound scanning routine of the knee joint to produce data that may yield diagnostically significant trends in the meniscus degeneration and displacement. Simultaneous segmentation of the multiple objects on a set of real knee meniscus ultrasound images has demonstrated the robustness against various shapes, sizes, and positions of the objects. Early diagnosis and monitoring of the disease progression is possible by measuring the meniscus area and position before and after the degeneration and displacement. Change in the meniscus area and position can be quantified over time by comparing the area and position at a certain time interval. Further investigation on the relative comparison of the meniscus area or position before and after the degeneration or displacement requires two (or more) observations of its occurrence. As the degeneration or displacement usually takes place in the subject after a long period of time, i.e., six month intervals, monitoring this occurrence in the patient would spend some time too.

Although segmentation of the normal meniscus in the ultrasound images still poses a considerable challenge and clinical value, the inclusion of another specific pathological change in the meniscus to investigate the performance of the segmentation algorithm to various grade of the meniscus degeneration and displacement could also guide future work. As a typical characteristic of energy minimizing local active contour methods, this method requires user initialization, however, due to the various applications of the ultrasound imaging for the diagnosis of the degenerative diseases, a fully automatic segmentation algorithm is desirable. Future improvements include making the algorithm more independent to the user by automating the setting of the parameters and by eliminating the dependency on the position of the initial curve. The use of the adaptive scale kernel and multiple active contours framework discussed in this thesis is not restricted to the meniscus ultrasound image applications specifically, or even the ultrasound images in general. It can benefit to other applications and assist in improving the accuracy and convergence of other methods as well.

5.2.4 Registration of the 2-D ultrasound image of the meniscus to the 3-D MRI volume

It is known that ultrasound imaging produces a low image quality compared to MRI that provides an excellent image quality where some parts of the meniscus may be occluded when captured by the ultrasound imaging. Since the accuracy of the measurement of the meniscus area would rely on the segmentation accuracy, it is interesting to compare the accuracy of meniscus segmentation between both imaging modalities. In order to provide a quantitative relation between the measurement of the meniscus area in the 2-D ultrasound image plane and the real 3-D MRI volume, the measurement of the meniscus area performed in the 2-D ultrasound image plane and the 3-D MRI volume need to be compared. Since the 2-D meniscus ultrasound image plane is seen as a projected image plane from the real 3-D MRI volume of the knee joint, spatial registration of the 2-D ultrasound image plane to the 3-D MRI volume is necessary to provide a quantitative comparison on the measurement of the meniscus area. A rigid-body geometrical transformation can be applied to spatially align the 2-D ultrasound planar image into the 3-D MRI volumetric data. A prior knowledge of the orientation of the ultrasound probe in the acquisition protocol with respect to 3-D axes of the knee joint of the subject can be used to determine the position of the 2-D ultrasound image plane in the 3-D MRI volumetric data. A cross-sectional 2-D MRI image plane, that matches with the orientation of the 2-D ultrasound image plane, is interpolated from the 3-D MRI volume. Thus, the segmentation accuracy and the area measurement of the meniscus in the interpolated cross-sectional 2-D MRI and the 2-D ultrasound planar images can be compared quantitatively.

REFERENCES

Abraham, A. M., Goff, I., Pearce, M. S., Francis, R. M., & Birrell, F. (2011). Reliability and validity of ultrasound imaging of features of knee osteoarthritis in the community. *BMC Muscuskeletal Disorder*, *70*(12), 1471-2474.

Acebes, C., Romero, F. I., Contreras, M. A., Mahillo, I., & Herrero-Beaumont, G. (2013). Dynamic ultrasound assessment of medial meniscal subluxation in knee osteoarthritis. *Rheumatology*, *52*, 1443-1447.

Aisen, A. M., McCune, W. J., MacGuire, A., Carson, P. L., Silver, T. M., Jafri, S. Z., & Martel, W. (1984). Sonographic evaluation of the cartilage of the knee. *Radiology*, *153*(3), 781-784.

Amin, S., LaValley, M. P., Guermazi, A., Grigoryan, M., Hunter, D. J., Clancy, M., ... Felson, D. T. (2005). The relationship between cartilage loss on magnetic resonance imaging and radiographic progression in men and women with knee osteoarthritis. *Arthritis and Rheumatism*, *52*(10), 3152-3159.

Arthritis of the knee. (2017, August). Retrieved from `http://orthoinfo.aaos.org/topic.cfm?topic=a00212`

Bland, J. M., & Altman, D. G. (1999). Measuring agreement in method comparison studies. *Statistical Methods in Medical Research*, *8*, 135-160.

Boniatis, I., Panayiotakis, G., & Panagiotopoulos, E. (2008). A computer-based system for the discrimination between normal and degenerated menisci from magnetic resonance images. In *Proceedings of 2008 IEEE International Workshop on Imaging Systems and Techniques* (p. 510-513). Chania, Greece.

Braun, H. J., & Gold, G. E. (2012). Diagnosis of osteoarthritis: Imaging. *Bone*, *51*, 278-288.

Brox, T., & Weickert, J. (2006). Level set segmentation with multiple regions. *IEEE Transactions on Image Processing*, *15*(10), 2029-2039.

Buckland-Wright, J. C. (1994). Quantitative radiography of osteoarthritis. *Annals of Rheumatic Disease*, *53*, 268-275.

Casseles, V., Kimmel, R., & Sapiro, G. (1997). Geodesic active contours. *International Journal of Computer Vision*, *22*(1), 61-79.

Chan, T. F., & Vese, L. A. (2001). Active contours without edges. *IEEE Transactions on Image Processing*, *10*(2), 266-277.

Chan, W. P., Lang, P., Stevens, M. P., Sack, K., Majumdar, S., Stoller, D. W., . . . Genant, H. K. (1991). Osteoarthritis of the knee: comparison of radiography, CT, and MR imaging to assess extent and severity. *American Journal of Roentgenology*, *157*(4), 799-806.

Cohen, J. (1960, Apr.). A coefficient of agreement for nominal scales. *Educational and Psychological Measurement*, *20*(1), 37-46.

Darolti, C., Mertins, A., Bodensteiner, C., & Hoffman, U. G. (2008). Local region descriptor for active contours evolution. *IEEE Transactions on Image Processing*, *17*(12), 2275-2288.

Dice, L. R. (1945). Measures of the amount of ecologic association between species. *Ecology*, *26*(3), 297-302.

Dodin, P., Pelletier, J.-P., Martel-Pelletier, J., & Abram, F. (2010). Automatic human knee cartilage segmentation from 3-D magnetic resonance images. *IEEE Transactions on Biomedical Engineering*, *57*(11), 2699-2711.

Faisal, A., & Pluempitiwiriyawej, C. (2012). Active contour using local region-scalable force with expandable kernel. In *Proceedings of 2012 IEEE International Conference on Information Science and Technology (ICIST)* (p. 18-24). Wuhan, China.

Folkesson, J., Dam, E. B., Olsen, O. F., Pettersen, P. C., & Christiansen, C. (2007). Segmenting articular cartilage automatically using a voxel classification approach. *IEEE Transactions on Biomedical Engineering*, *26*(1), 106-115.

Fripp, J., Bourgeat, P., Engstrom, C., Ourselin, S., Crozier, S., & Salvado, O. (2009). Automated segmentation of the menisci from MR images. In *Proceedings of 2009 IEEE International Symposium on Biomedical Imaging: From Nano To Macro* (p. 510-513). Boston, MA.

Fripp, J., Crozier, S., Warfield, S. K., & Ourselin, S. (2010). Automatic segmentation and quantitative analysis of the articular cartilages from magnetic resonance images of the knee. *IEEE Transactions on Medical Imaging*, *29*(1), 55-63.

Heuer, F., Sommer, M., III, J. B. R., & Bottlang, M. (2001). Estimation of cartilage thickness from joint surface scans: comparative analysis of computational methods. In *Proceedings of the 2001 ASME Bioengineering Conference* (Vol. 50, p. 569-570).

Hunter, D. J., Buck, R., Vignonk, E., Eckstein, F., Brandt, K., Mazzucayy, S. A., ... Graverandx, M. P. H. L. (2009). Relation of regional articular cartilage morphometry and meniscal position by MRI to joint space width in knee radiographs. *Osteoarthritis and Cartilage*, *17*, 1170-1176.

Hunter, D. J., Zhang, Y. Q., Tu, X., LaValley, M., Niu, J. B., Amin, S., ... Felson, D. T. (2006). Change in joint space width: Hyaline articular cartilage loss or alteration in meniscus? *Arthritis and Rheumatism*, *54*(8), 2488-2495.

Huttenlocher, D. P., Klanderman, G. A., & Rucklidge, W. J. (1993). Comparing images using the Hausdorff distance. *IEEE Transactions on Pattern Analysis and Machine Intelligence*, *15*(9), 850-863.

Iagnocco, A. (2010). Imaging the joint in osteoarthritis: A place for ultrasound? *Best Practice and Research Clinical Rheumatology*, *24*, 27-38.

Iagnocco, A., Coari, G., & Zoppini, A. (1992). Sonographic evaluation of femoral condylar cartilage in osteoarthritis and rheumatoid arthritis. *Scandinavian Journal of Rheumatology*, *21*(4), 201–203.

Jackson, D., Simon, T., & Aberman, H. (2001). Symptomatic articular cartilage degeneration: the impact in the new millennium. *Clinical Orthopaedics and Related Research*, *391*, 14-15.

Kazam, J. K., Nazarian, L. N., Miller, T. T., Sofka, C. M., Parker, L., & Adler, R. S. (2011). Sonographic evaluation of femoral trochlear cartilage in patients with knee pain. *Journal of Ultrasound Medicine*, *30*(6), 797-802.

Landis, J. R., & Koch, G. G. (1977, Mar.). The measurement of observer agreement for categorical data. *Biometrics*, *33*(1), 159-174.

Lankton, S., & Tanenbaum, A. (2008). Localizing region-based active contours. *IEEE Transactions on Image Processing*, *17*(11), 2029-2039.

Li, C., Huang, R., Ding, Z., Gatenby, C., Metaxas, D. N., & Gore, J. C. (2011). A level set method for image segmentation in the presence of intensity inhomogeneities with application to MRI. *IEEE Transactions on Image Processing*, *20*(7), 2007-2016.

Li, C., Kao, C., Gore, J. C., & Ding, Z. (2008). Minimization of region scalable fitting energy for image segmentation. *IEEE Transactions on Image Processing*, *17*(10), 1940-1949.

Maurer, C. R., Qi, R., & Raghavan, V. (2003). A linear time algorithm for computing exact Euclidean distance transforms of binary images in arbitrary dimensions. *IEEE Transactions on Pattern Analysis and Machine Intelligence*, *25*(2), 265-270.

Michailovich, O., Rathi, Y., & Tannenbaum, A. (2007). Image segmentation using active contours driven by the Bhattacharyya gradient flow. *IEEE Transactions on Image Processing*, *16*(11), 2787-2801.

Moller, I., Bong, D., Naredo, E., Filippucci, E., Carrasco, I., Moragues, C., & Iagnocco, A. (2008). Ultrasound in the study and monitoring of osteoarthritis. *Osteoarthritis and Cartilage*, *16*, S4-S7.

Mukherjee, S., & Acton, S. T. (2015). Region based segmentation in presence of intensity inhomogeneity using Legendre polynomials. *IEEE Signal Processing Letters*, *22*(3), 298-302.

Mumford, D., & Shah, J. (1989). Optimal approximation by piecewise smooth functions and associated variational problems. *Communications on Pure and Appllied Mathematics*, *42*, 577-658.

Naredo, E., Acebes, C., Moller, I., Canillas, F., de Agustin, J. J., de Miguel, E., . . . Saenz-Navarro, I. (2009). Ultrasound validity in the measurement of knee cartilage thickness. *Annals of Rheumatic Disease*, *68*, 1322-1327.

Naredo, E., Cabero, F., Palop, M. J., Collado, P., Cruz, A., & Crespo, M. (2005). Ultrasonographic findings in knee osteoarthritis: A comparative study with clinical and radiographic assessment. *Osteoarthritis and Cartilage*, *13*(7), 568-574.

Oo, W. M., & Boo, M. T. (2016). Role of ultrasonography in knee osteoarthritis. *Journal of Clinical Rheumatology*, *22*(6), 324-329.

Osher, S., & Sethian, J. (1988). Front propagating with curvature-dependent speed:

Algorithms based on Hamilton-Jacobi formulations. *Journal of Computational Physics*, *79*(1), 12-49.

Pereiraya, D., Peleteiroyza, B., Araújoyza, J., Brancoxa, J., Santoska, R. A., & Ramos, E. (2011). The effect of osteoarthritis definition on prevalence and incidence estimates: a systematic review. *Osteoarthritis and Cartilage*, *19*, 1270-1285.

Phumeechanya, S., Pluempitiwiriyawej, C., & Thongvigitmanee, S. (2010). Active contour using local regional information on extendable search lines (LRES) for image segmentation. *IEICE Transactions on Information and Systems*, *E-93*(6), 1625-1635.

Roemer, F. W., Crema, M. D., Trattnig, S., & Guermazi, A. (2011). Advances in imaging of osteoarthritis and cartilage. *Radiology*, *260*(2), 332-354.

Saarakkala, S., Waris, P., Waris, V., Tarkiainen, I., Karvanen, E., Aarnio, J., & Koski, J. M. (2012). Diagnostic performance of knee ultrasonography for detecting degenerative changes of articular cartilage. *Osteoarthritis and Cartilage*, *20*, 376-381.

Shan, L., Zach, C., & Niethammer, M. (2010). Automatic three-label bone segmentation from knee MR images. In *Proceedings of the IEEE International Symposium Biomedical Imaging* (p. 1325-1328).

Solloway, S., Hutchison, C., Waterton, J., & Taylor, C. (1993). The use of active shape models for making thickness measurements of articular cartilage from MR images. *Magnetic Resonance Medicine*, *13*(5), 943-952.

Swanson, M. S., Prescott, J. W., Best, T. M., Powell, K., Jacksonk, R. D., Haq, F., & Gurcan, M. N. (2010). Semi-automated segmentation to assess the lateral meniscus in normal and osteoarthritic knees. *Osteoarthritis and Cartilage*, *18*(3), 344-353.

Tang, J., Millington, S., Acton, S. T., Crandall, J., & Hurwitz, S. (2006). Surface extraction and thickness measurement of the articular cartilage from MR images using directional gradient vector flow snakes. *IEEE Transactions on Biomedical Engineering*, *53*(5), 896-907.

Tsai, A., Yezzi, J. A., & Willsky, A. S. (2001). Curve evolution implementation of the Mumford-Shah functional for image segmentation, denoising, interpolation, and magnification. *IEEE Transactions on Image Processing*, *10*(8), 1169-1186.

Vese, L. A., & Chan, T. F. (2002). A multiphase level set framework for image segmentation using the Mumford and Shah model. *International Journal of Computer Vision*, *50*(3), 271-293.

Wang, J., Cheng, Y., Guo, C., Wang, Y., & Tamura, S. (2016). Shape-intensity prior level set combining probabilistic atlas and probability map constrains for automatic liver segmentation from abdominal CT images. *International Journal of Computer Assisted Radiology and Surgery*, *11*(5), 817-826.

Wang, L., He, L., Mishra, A., & Li, C. (2009). Active contours driven by local Gaussian distribution fitting energy. *Signal Processing*, *89*(12), 2435-2447.

Wang, X.-F., Min, H., & Zhang, Y.-G. (2015). Multi-scale local region based level set method for image segmentation in the presence of intensity inhomogeneity. *Neurocomputing*, *151*, 1086 - 1098.

Wang, X.-F., Min, H., Zou, L., & Zhang, Y.-G. (2015). A novel level set method for image segmentation by incorporating local statistical analysis and global similarity measurement. *Pattern Recognition*, *48*(1), 189 - 204.

What is arthritis? (2014, December). Retrieved from `http://www.arthritisresearchuk.org/arthritis-information/conditions/arthritis/what-is-arthritis.aspx`

World Health Organization. (2002). The World Health Report 2002. *Reducing Risks, Promoting Healthy Life*.

Xiao, G., Brady, M., Noble, J. A., & Zhang, Y. (2002). Segmentation of ultrasound B-mode images with intensity inhomogeneity correction. *IEEE Transactions on Medical Imaging*, *21*(1), 48-57.

Yezzi, A., & Prince, J. (2003). An eulerian PDE approach for computing tissue thickness. *IEEE Transactions on Medical Imaging*, *22*(10), 1332-1339.

Yezzi, J. A., Tsai, A., & Willsky, A. S. (2002). A fully global approach to image segmentation via coupled curve evolution equations. *Journal of Visual Communication and Image Representation*, *13*(1), 195-216.

Zhang, H., Ye, X., & Chen, Y. (2013). An efficient algorithm for multiphase image segmentation with intensity bias correction. *IEEE Transactions on Image Processing*, *22*(10), 3842-3851.

Zhang, K., Zhang, L., Lam, K. M., & Zhang, D. (2016). A level set approach to image segmentation with intensity inhomogeneity. *IEEE Transaction on Cybernetics*, *46*(2), 546-557.

Zhang, K., Zhang, L., Song, H., & Zhang, D. (2013). Reinitialization-free level set evolution via reaction diffusion. *IEEE Transactions on Image Processing*, *22*(1), 258-271.

Zhang, K., Zhang, L., & Zhang, S. (2010). A variational multiphase level set approach to simultaneous segmentation and bias correction. In *Proceedings of 2010 IEEE International Conference on Image Processing* (p. 4105-4108). Hong Kong.

Zhao, H. K., Chan, T., Merriman, B., & Osher, S. (1996). A variational level set approach to multiphase motion. *Journal of Computational Physics*, *127*, 179-195.

Zijdenbos, A. P., Dawant, B. M., Margolin, R. A., & Palmer, C. (1994). Morphometric analysis of white matter lesions in MR images: Method and validation. *IEEE Transactions on Medical Imaging*, *13*(4), 716-724.

LIST OF PUBLICATIONS AND PAPERS PRESENTED

Faisal, A., Ng, S. C., Goh, S. L., George, J., Supriyanto, E., & Lai, K. W. (2015). Multiple LREK active contours for knee meniscus ultrasound image segmentation. *IEEE Transactions on Medical Imaging*, *34*(10), 2162 - 2171.

Faisal, A., Ng, S. C., Goh, S. L., & Lai, K. W. (2017a). Knee cartilage segmentation and thickness computation from ultrasound images. *Medical & Biological Engineering & Computation*. doi: https://doi.org/10.1007/s11517-017-1710-2

Faisal, A., Ng, S. C., Goh, S. L., & Lai, K. W. (2017b). Knee cartilage ultrasound image segmentation using locally statistical level set method. In *Proceedings of 2017 International Conference for Innovation in Biomedical Engineering and Life Sciences (ICIBEL).* Penang, Malaysia.

Faisal, A., Ng, S. C., & Lai, K. W. (2014). Multiple active contours using scalable local regional information on expandable kernel. In *Proceedings of 2014 IEEE Conference on Biomedical Engineering and Sciences (IECBES)* (p. 541-544). Miri, Malaysia.